Downloaded from orbit.dtu.dk on: May 05, 2023

DTU Library

Development of Models and Algorithms for the Study of Reactive Porous Media Processes

Kristensen, Morten Rode

Publication date:
2008

Document Version
Publisher's PDF, also known as Version of record

Link back to DTU Orbit

Citation (APA):
Kristensen, M. R. (2008). *Development of Models and Algorithms for the Study of Reactive Porous Media Processes*.

General rights
Copyright and moral rights for the publications made accessible in the public portal are retained by the authors and/or other copyright owners and it is a condition of accessing publications that users recognise and abide by the legal requirements associated with these rights.

- Users may download and print one copy of any publication from the public portal for the purpose of private study or research.
- You may not further distribute the material or use it for any profit-making activity or commercial gain
- You may freely distribute the URL identifying the publication in the public portal

If you believe that this document breaches copyright please contact us providing details, and we will remove access to the work immediately and investigate your claim.

Development of Models and Algorithms for the Study of Reactive Porous Media Processes

Morten Rode Kristensen

2008

Ph.D. Thesis

DTU

TECHNICAL UNIVERSITY OF DENMARK
DEPARTMENT OF CHEMICAL ENGINEERING

Development of Models and Algorithms for the Study of Reactive Porous Media Processes

Morten Rode Kristensen

Department of Chemical and Biochemical Engineering
Technical University of Denmark
Kongens Lyngby, Denmark

Technical University of Denmark
Department of Chemical and Biochemical Engineering
Building 229, DK-2800 Kongens Lyngby, Denmark
Phone +45 45252800, Fax +45 45882258
kt@kt.dtu.dk
www.kt.dtu.dk

Copyright © Morten Rode Kristensen, 2008
ISBN 978-87-91435-74-9
Printed by Frydenberg A/S, Copenhagen, Denmark

Preface

This thesis was prepared at Department of Chemical and Biochemical Engineering, Technical University of Denmark (DTU), in partial fulfillment of the requirements for receiving the Ph.D. degree. The work presented in the thesis was carried out from August 2004 to January 2008.

During the course of the work presented in the thesis, a number of people have provided their help and support, for which I am very grateful. First of all, I would like to thank my advisors at DTU, Per G. Thomsen, Michael L. Michelsen and Erling H. Stenby, for their guidance, encouragement and many valuable inputs, but most of all for allowing me the freedom to pursue my own ideas and interests. I would also like to thank my friends and colleagues at IVC-SEP for providing a fun and stimulating research environment, in particular my long term office mate Kent Johansen. Together we explored many aspects of reservoir simulation and managed to have some fun along the way. Thanks also to John B. Jørgensen for being a great mentor and a friend and patiently listening to my frustrations and offering advice during rough times.

During my Ph.D. I was fortunate to have the opportunity to spend more than a year at Stanford University, California, at the Department of Energy Resources Engineering. A very special thank you to Margot G. Gerritsen for kindly hosting my visits, making me feel a part of the SUPRI-C research group, and for excellent guidance during my visits as well as during time spent in Denmark. Thanks to the many friends I made at Stanford, especially Shalini Krishnamurthy, Rami Younis and Taku Ide, with whom I shared countless coffee breaks. I have benefitted tremendously from the time at Stanford, both academically and personally, and for that I am very grateful.

Finally, I wish to thank my family and friends for continuous support.

Kongens Lyngby, January 2008

Morten Rode Kristensen

Summary

The subject of this thesis is modeling and simulation of reactive porous media processes with emphasis on the enhanced oil recovery process known as In-Situ Combustion (ISC). The motivation for addressing this topic is the high potential of ISC as a recovery method for the world's vast heavy oil reserves combined with the shortcomings in current mathematical models and numerical simulators with respect to providing accurate, efficient, and reliable performance predictions required for safe and cost-effective design of ISC projects. ISC is a complex process coupling chemical reactions and phase equilibria with thermal, multicomponent, multiphase porous media flow. Accurate prediction of field performance in such a multiscale process requires that both spatial and temporal resolution in a numerical simulation is adapted in order to capture the behavior at different scales. Efficient computational methods are needed, which handle this multiscale nature.

Two ISC models have been developed. The Virtual Combustion Tube (VCT) is an equation of state compositional, one-dimensional ISC model for laboratory scale combustion simulation. It accounts for the simultaneous flow, transport of heat and mass, chemical reactions, and phase equilibrium. The Virtual Kinetic Cell (VKC) is, essentially, a zero-dimensional version of the VCT. It models a multiphase, chemical batch reactor, which facilitates the isolated study of chemical reactions and phase behavior. Together, the two models provide a flexible platform for the fundamental study and support of laboratory scale combustion experiments.

The efficiency of ISC processes depends critically on the formation and sustained propagation of a high-temperature combustion front. The models developed were employed to study the impact of phase behavior modeling on ignition/extinction phenomena. Compositional changes affect the chemical kinetics and thereby the process performance. It was demonstrated that a simplified ideal mixture based approach to phase behavior modeling, which is common in

thermal simulators, may overestimate the air injection rate required to sustain combustion compared to a rigorous equation of state based approach. The VCT was used quantitatively to map ignition/extinction regimes as a function of key parameters, such as air injection rate and heat loss rate. It was further demonstrated that, qualitatively, the same conclusions regarding impact of different phase behavior models can be obtained from simulations using the VKC.

A simple and intuitive scheme based on operator splitting techniques was proposed for numerical integration of the ISC equations. Each global integration step in the scheme is composed of a sequence of substeps on the flow/transport and reaction parts of the equations, respectively, the advantage being that the subprocesses can be integrated with tailored methods and timesteps. A family of tailored methods was designed for the chemical reaction subprocess. The new methods proved 2–5 times faster than off-the-shelf stiff ODE solvers when applied to operator splitting integration of ISC kinetics. The integration methods were further extended with a novel algorithm for robust detection and location of fluid phase changes. This algorithm was shown to improve the integration robustness by lowering the number of convergence and error test failures when crossing phase boundaries.

Resumé

Emnet for denne afhandling er modellering og simulering af reaktiv strømning i porøse medier med hovedvægt på *In-Situ Combustion* (ISC) processen til forbedret olieindvinding. Emnet er motiveret af ISC processens potentiale som indvindingsteknik for verdens store reserver af tung olie. Dertil kommer, at eksisterende matematiske modeller og numeriske simulatorer er utilstrækkelige til at forudsige processens opførsel med tilpas nøjagtighed, pålidelighed og effektivitet, hvilket er afgørende for sikre et forsvarligt og omkostningseffektivt design af processen. ISC er en fysisk kompleks proces, der kombinerer kemiske reaktioner og faseligevægt med termisk flerkomponent- og flerfasestrømning i et porøst medium. For pålideligt at kunne forudsige processens opførsel i en numerisk simulering kræves, at både den rumlige og tidsmæssige inddeling i simuleringen tilpasses processens forskellige skalaer. Der er således behov for udvikling af effektive beregningsalgoritmer, som tager højde for processens flerskala opførsel.

Der er udviklet to modeller for ISC. Den første (*The Virtual Combustion Tube (VCT)*) er en én-dimensional kompositionel model baseret på en tilstandsligning. Den anden (*The Virtual Kinetic Cell (VKC)*) er en simplificeret udgave af VCT modellen begrænset til én celle. VKC modellen beskriver et flerfase system i en batch reaktor, hvilket muliggør isolerede undersøgelser af kemiske reaktioner og faseligevægt. De to modeller udgør tilsammen en platform, hvor laboratorieskala forbrændingseksperimenter kan studeres gennem simuleringer.

Effektiviteten af ISC processer afhænger af, om der dannes en stabil højtemperatur forbrændingsfront, som bevæger sig gennem systemet og fortrænger olien. De udviklede modeller blev anvendt til at undersøge, hvordan modellering af faseligevægten påvirker dannelsen af en forbrændingsfront. Ændringer i oliens sammensætning vil påvirke de kemiske reaktioner og dermed processens opførsel. Resultaterne viser, at med en simpel tilgang til modellering af faseligevægten baseret på ideale blandinger, som er en almindelig antagelse i termiske reservoirsimulatorer, overestimerer den minimale mængde luft, som kræves for

at opretholde forbrænding, i forhold til en mere nøjagtig tilgang baseret på en tilstandsligning. VCT modellen blev anvendt kvantitativt til at kortlægge områder i parameterrummet, hvor der opnås en stabil forbrændingsfront, som funktion af operationsbetingelserne, herunder injektionshastigheden af luft samt varmetabet fra systemet. Det blev yderligere vist, at der via simuleringer med VKC modellen kvalitativt kan drages de samme konklusioner med hensyn til indflydelsen af forskellige faseligevægtsmodeller.

Et simpelt tidsintegrationsskema baseret på *operator splitting* teknikker blev udviklet for ISC ligningerne. Hvert globale tidsskridt i skemaet er sammensat af en række delskridt for henholdsvis strømnings- og transportdelen samt reaktionsdelen af de overordnede ligninger. Fordelen herved er, at hver enkelt delprocess kan integreres med specielt tilpassede metoder og tidsskridt. Med fokus på reaktionsdelen blev der designet en klasse af integrationsmetoder, som er specielt velegnet til integration af kemisk reaktionskinetik. Effektivitetssammenligninger med standard metoder til stive ordinære differentialligninger viser, at de nye metoder er 2–5 gange hurtige. Metoderne blev yderligere udvidet med en ny algoritme til robust håndtering af faseovergange. Algoritmen forbedrer robustheden af integrationsprocessen ved at mindske antallet af konvergensfejl i forbindelse faseovergange.

Contents

Chapter 1

Introduction

The purpose of this introductory chapter is to motivate the work presented in this thesis, state the objective of the research and give an overview of the key contributions. Since the topic is reactive porous media transport, we first discuss briefly the different application areas for such processes and then describe in more detail the particular process, which will be the primary focus in this thesis: the in-situ combustion enhanced oil recovery (EOR) process. By means of a discussion of the potential of this process as an EOR method, the nature of the process, and shortcomings in current models and simulation technologies, the motivation and objectives of the work are given in Section 1.3. The key contributions are summarized in Section 1.4, and an outline of the remainder of the thesis is given in Section 1.5.

1.1 Reactive porous media transport

Applications of reactive porous media transport cover the range from small-scale reaction-diffusion problems in catalyst pellets to large-scale transport problems in geologic reservoirs. The application, which dominates the literature on large-scale reactive porous media transport, is subsurface contaminant migration. The contamination arises due to e.g. chemical spills or improper waste disposal, and an extensive literature exists on the modeling and simulation of the subsurface transport processes to understand the migration behavior and design remediation strategies (see e.g. Yeh and Tripathi (1991); Walter et al. (1991)). The chemical species are often present in small amounts, but undergo a range of

chemical processes, including oxidation-reduction, dissolution-precipitation and adsorption-desorption, which must be accounted for in simulation models. The chemical processes usually have little or no influence on the flow, and the flow and transport problems are therefore naturally decoupled.

Filtration combustion (Aldushin et al., 1997; Schult et al., 1996) covers a different class of reactive porous media transport problems. When delivery of reactants through the pores to the reaction site is an important aspect of the combustion process, it is referred to as filtration combustion. It is the study of reaction front propagation in a porous medium, where a gaseous oxidizer reacts with a solid fuel or the porous medium itself. Examples include smoldering, catalyst regeneration, and naturally occurring coal bed fires. The chemical reactions are transport limited, and the mathematical structure of the resulting models often allow analytical solution techniques.

In the context of oil recovery, several EOR techniques involve chemical reactions, including CO_2 injection, microbial EOR, and the air injection technique known as *in-situ combustion* (ISC). In this thesis we consider exclusively modeling and simulation of in-situ combustion, but we emphasize that the models and simulation techniques developed are applicable to a wider range of porous media problems. Later, in particular when developing numerical solution techniques in Chapter 3, we will discuss differences and similarities with contaminant transport problems and look at the solution techniques traditionally applied in this field. Modeling of ISC processes has been approached using techniques from both filtration combustion and contaminant transport, and we will review the different models in Section 1.2.5.

1.2 In-situ combustion (ISC)

The world continues to rely substantially on petroleum fossil fuels as a primary energy source. While the number of new discoveries of petroleum reservoirs decreases, the need to produce the known reservoirs more effectively increases. So far, only the easiest to produce petroleum accumulations have been utilized, and an advancement in technology is needed to access more difficult to produce reservoirs and to address in a cost-effective manner the volume of oil that remains after primary and secondary operations. By 2007, proved world oil reserves were estimated at 1.3 trillion barrels, which cover crude oil reserves that with reasonable certainty can be recovered in future years, assuming existing economic and operating conditions (EIA-DOE, 2007). It is further estimated that Canada and Venezuela alone have heavy oil reserves, which far exceed the world's conventional reserves, but which cannot yet be economically recovered.

Thermal recovery processes, which rely on a viscosity reduction of the oil through heat injected (steam or hot water) or in-situ generated, are well suited to unlock effectively these heavy oil resources in an environmentally sound manner. Among the thermal recovery processes, ISC has been a source of interest and

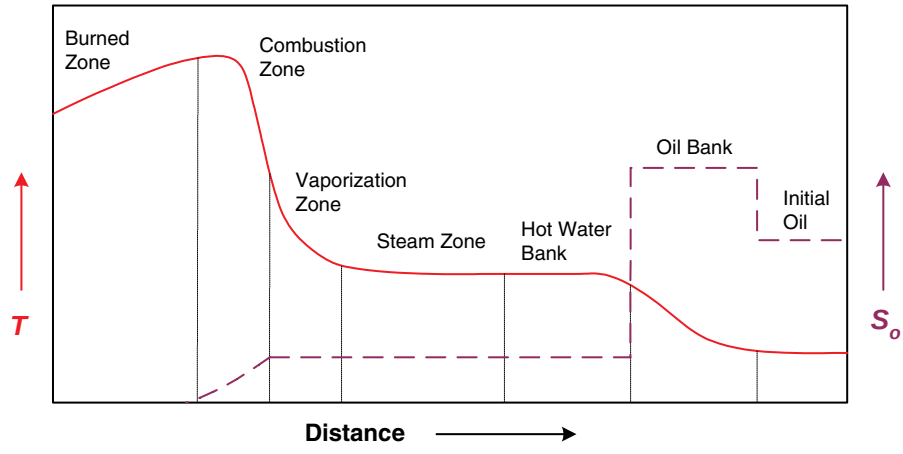

Figure 1.1: Schematic representation of characteristic temperature and saturation distributions in forward in-situ combustion (adapted from Prats, 1986, not to scale).

effort for several decades. ISC is the process of injecting air (or air enriched with oxygen) into oil reservoirs to oxidize a portion of the crude oil and enhance recovery through the heat and pressure produced. Contrary to other thermal recovery processes the main part of the energy required to displace the oil in ISC is generated inside the reservoir from the heat released by chemical reactions between oxygen and fractions of the crude oil.

ISC is technically and economically an attractive process, particularly since the portion of the crude burned is likely to be the heaviest and least valuable. Whereas it is generally classified as a technique that is applicable for heavy oils because of the dramatic reduction in oil viscosity with temperature, ISC also promotes production through thermal expansion and gas drive caused by combustion gases. The process has proven economical in recovering heavy oil from shallow reservoirs and lighter oil from deep reservoirs, where other processes, such as steam injection, are unattractive (Sarathi, 1999). When applied to deep light oil reservoirs, the process is often referred to as *high pressure air injection* (HPAI), whereas the term *in-situ combustion* traditionally has been used for heavy oil reservoirs. Throughout this thesis we refer to air injection into both heavy and light oil reservoirs as in-situ combustion, but important differences between the two settings will be highlighted.

1.2.1 Process description

The ISC process is generally described based on the respective directions of front propagation and air flow. In *forward combustion* oil is ignited at the injection well and the combustion front is propagated towards the production well by

continuous injection of air. In *reverse combustion*, on the other hand, the oil in the production well is ignited and the combustion front propagates against the air flow. Compared to forward combustion the temperature in reverse combustion remains high between the combustion zone and the production well, which has the effect of promoting the flow of oil. The disadvantage of the method is that a residue of solid fuel may block the pores and slow down displacement. Moreover, spontaneous ignition of oil may occur near the injection well consuming most of the oxygen and causing a breakdown in the supply of oxygen to the combustion front (Prats, 1986). For these reasons, forward combustion is solely practiced in the field.

As air is injected and the combustion front progresses into the reservoir, several zones can be found between the injector and the producer. A common misconception of the combustion front propagation is that of an underground fire. Instead, the front is more of a glow passing slowly through the reservoir, similar to the hot zone of a burning cigarette. Figure 1.1 gives a schematic representation of characteristic temperature and saturation zones in ISC. Starting from the injection well the burned zone is the volume already swept by the combustion zone. The burned zone contains the injected air and possibly a residue of burned fuel. The combustion zone has the highest temperature and this is where most of the energy is generated. Injected oxygen reacts with residual hydrocarbons generating carbon oxides and water. Hydrocarbons contacted by the leading edge of the high temperature zone undergo thermal cracking and vaporization. Mobilized light components are transported downstream where they mix with the original crude. The heavy residue, which is normally referred to as coke, is deposited on the core matrix and is the main fuel source for the combustion process. Downstream of the vaporization zone is the steam plateau which is formed from water of combustion and vaporization of formation water. Further downstream the steam condenses into a hot water bank when the temperature drops below the steam saturation temperature. The leading edge of the hot water bank is the primary area of oil mobilization where the oil is banked by the hot water. A more detailed description may be found in Prats (1986) and Castanier and Brigham (2004). A recently developed operation technique involving horizontal wells is Toe-to-Heel Air Injection (THAI) (Greaves et al., 2005), in which air is injected in a vertical well and oil is produced from a long horizontal well. As the combustion front is propagated, the heated oil is drained into the producer, a technique similar to Steam Assisted Gravity Drainage (SAGD) (Butler et al., 1981).

When only air is injected into the reservoir the process is referred to as *dry* combustion. A disadvantage of this process is that a large part of the energy generated remains behind the combustion front as heat absorbed in the reservoir rock. Because of the low heat capacity of air, the heat in the burned zone is not transported efficiently by the injected air. To overcome this inefficiency water can be injected either simultaneously or alternately which is referred to as *wet* combustion. The water-air ratio determines whether water is transported

through the combustion zone in a vapor or liquid state. At sufficiently high water-air ratio liquid water will enter or even pass all the way through the combustion zone leading to quenched or partially quenched combustion.

The actual mechanisms responsible for oil displacement in ISC vary with the type of oil. For heavy oils the increase in oil mobility with elevated temperatures is the primary mechanism assisted by gas flood effects and hot and cold water drive. In the case of lighter oils, the flue gas mixture resulting from combustion provides the primary mobilizing force for the oil downstream of the combustion zone (Moore et al., 2002*a*). The gas-oil mixture may be immiscible, or partly or completely miscible.

Many economically successful ISC projects exist (Moore et al., 1995, 2002*a*). Application of the process is, however, not widespread for a variety of reasons including the relatively large expense required to evaluate prospects. It is often regarded as a high-risk process due to the current lack of reliable tools for accurate and efficient prediction of field performance.

1.2.2 Characteristic behavior

In this section we discuss qualitatively the characteristic behavior observed when burning different kinds of oil under varying conditions in laboratory scale tube tests. Only little is known about ISC processes at the field scale. However, laboratory combustion tube tests provide a good testbed for assessing burning characteristics and studying effects of varying process conditions (e.g. pressure, initial oil and water saturations).

Figure 1.2 shows characteristic temperature profiles observed in ISC laboratory tube tests. Profiles are shown for dry and wet combustion of a typical heavy oil and for dry combustion of a light oil. For dry combustion with little or no initial water saturation the temperature profile shows a single front. No significant steam plateau is formed. The temperature remains fairly high behind the combustion front due to the limited ability of the injected gas to carry the heat forward. The major difference between heavy and light oil combustion is the temperature regime in which the process operates. Heavy oils typically burn at peak temperatures around 600°C, whereas light oils burn at much lower temperatures around 300°C. When water is injected in the wet combustion process, the heat absorbed in the rock in the burned region is effectively swept forward giving a sharper temperature peak. Moreover, vaporization of the water forms a steam bank ahead of the combustion front.

A phenomenon, which has been observed at laboratory scale and theorized to have a stabilizing effect on combustion fronts at the field scale, is the process of blocking and unblocking. Especially in highly oil saturated reservoirs this will be important. Due to the efficient oil mobilization in ISC, the oil will form a bank ahead of the combustion front and the gas saturation may drop below the critical saturation leading to vanishing gas permeability. With no gas permeability the system is blocked. For one-dimensional combustion tube

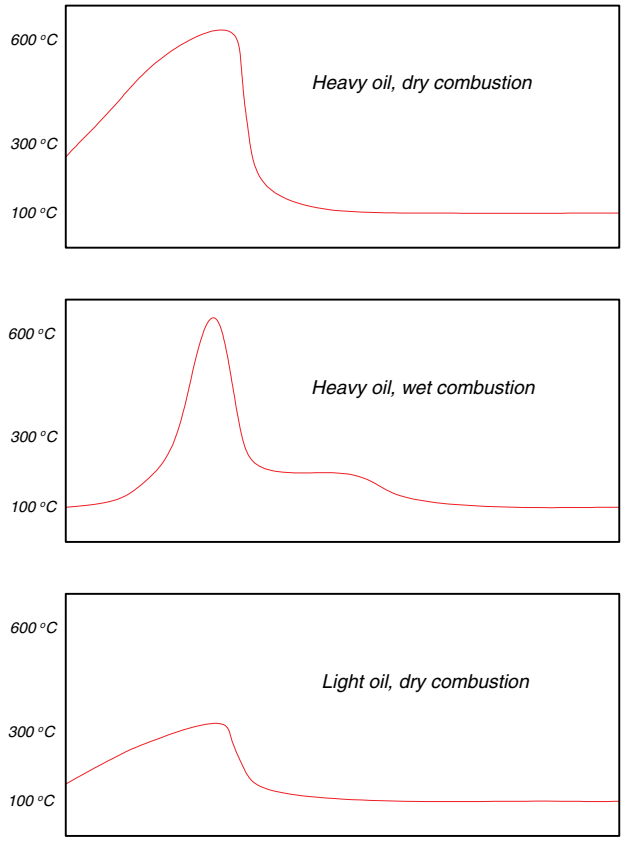

Figure 1.2: Characteristic temperature profiles in ISC for heavy/light oil and dry/wet combustion.

tests this can lead to a break-down of the process. In a heterogeneous field, however, blocking of certain paths in the reservoir may have a stabilizing effect on the combustion front. The mobilized oil will go to high permeability paths. Blocking of these paths will redirect flow to less permeable regions, thereby preventing fingering phenomena. The benefits of the blocking process at the field scale are still rather hypothetical, and no simulation results have been published capturing this effect. Accurate prediction of blocking and unblocking is likely to be very sensitive to the quality of the relative permeability data. Three phase relative permeability data is, in general, difficult to obtain, and very little is known about the effects of temperature and composition changes on relative permeabilities for processes like ISC.

1.2.3 Chemical reactions

A typical crude oil is a complex mixture of hundreds of different chemical species. Hence, the chemical reactions that happen in the presence of oxygen are equally complex and numerous. Deriving detailed reaction pathways for crude oil oxidation in porous media is far beyond current capabilities. Determining reactions and reaction rates in ISC is approached in an empirical way.

Today it is generally accepted that three classes of reactions dominate in ISC: (1) low temperature oxidation reactions (LTO), (2) medium temperature reactions and (3) high temperature oxidation reactions (HTO) (Castanier and Brigham, 2004). The temperature ranges associated with each group of reactions are roughly 150 to 300°C for LTO, 300 to 450°C for medium temperature reactions and above 450°C for HTO.

The nature of the reactions taking place in each regime depends on the type of oil. For heavy oils the LTO reactions are oxygen addition reactions producing partially oxygenated compounds (e.g. alcohols, ketones, aldehydes) and only few carbon oxides. Lighter oils undergo full H/C bond breaking combustion reactions in the LTO regime but may undergo oxygen addition reactions at lower temperatures. Oxygen addition increases oil viscosity, and thus operating in this regime is inefficient. In a forward combustion process LTO reactions may take place when oxygen is available downstream of the combustion front due to either channeling around the front or insufficient consumption in the front (Fassihi et al., 1984*a*). The effects of LTO on ISC performance have been studied by several researchers (e.g Dabbous and Fulton, 1974; Adegbesan et al., 1987; Freitag and Verkoczy, 2005). Although generally recognized as being important to prediction of ISC performance, no reliable LTO reaction models exist today. Freitag and Verkoczy (2005) observed a shift in reaction order for oxygen partial pressure with temperature and concluded that at least two different reaction mechanisms govern LTO. The negative effects of LTO are mainly an increase in oil viscosity and enhanced trapping of oil due to gas phase shrinkage caused by the oxygen removed from the gas phase in oxygen addition reactions (Moore et al., 2002*b*).

At intermediate temperatures after the LTO reactions a series of cracking or pyrolysis reactions take place. These reactions are the primary source of coke formation for the HTO reactions. Coke formation dictates the quantity of fuel available for combustion. Excessive fuel deposition retards the rate of advance of the combustion front whereas insufficient fuel deposition may not provide enough heat for self-sustained combustion. Finally, in the HTO reactions the coke is burned, generating carbon oxides and water.

Both LTO and HTO reactions are believed to be heterogeneous gas/liquid or gas/solid reactions (Fassihi et al., 1984*b*; Castanier and Brigham, 2004), in which oxygen from the gas stream diffuses to the surface of the oil/coke, adsorps on the surface, reacts with a hydrocarbon component, and finally combustion products desorp and diffuse back into the gas stream. It is widely accepted that

the overall reaction is kinetically controlled (Islam et al., 1989).

Concrete reaction models are introduced and discussed in research Paper I in Chapter 5.

1.2.4 A complex multiscale process

ISC is one of the most physically complex enhanced oil recovery processes currently in use. Driven by complex chemical reactions, the oil mobility is increased with the elevated temperatures, and the fluids are displaced by a combination of steam, water, and gas drive. The spatial as well as temporal scales in ISC vary over many orders of magnitude. The bulk of the chemical reactions take place in the narrow reaction zone that may be less than a meter in thickness compared to reservoir scales of hundreds or thousands of meters. Moreover, combustion reactions often occur in fractions of a second, whereas the temporal scales associated with convective transport may be running to days or years. Accurate prediction of field performance in such a multiscale process is an immense challenge requiring a hierarchical approach, in which both spatial and temporal resolution is adapted in order to capture the crucial input from all levels of activity.

The overall performance of an ISC process is governed in a complex way by reservoir heterogeneity, well configurations, injection rates and composition, initial oil saturation and distribution, and both thermodynamic and chemical properties of the rock and fluids. Reliable prediction of field performance requires a fully integrated approach in which the important contributions from all levels are taken into account. ISC is indeed a multiphysics process bringing together multiphase porous media flow, chemical kinetics, and phase equilibria.

The spatial scales affecting ISC span from large geological features such as faults of the size of the reservoir to the very small scale at which chemical reactions happen in the combustion zone. Faults, fractures, and the placement of wells determine global flow patterns, but local displacement efficiency is governed by small scale heterogeneity in porosity and permeability of the reservoir, and by the chemical and thermodynamic behavior of the fluids. Permeability fields are often obtained from high-resolution geocellular models having gridblock sizes on the order of a meter. Reservoir simulations, however, are carried out using gridblocks that are 1–2 orders of magnitude larger due to computational constraints. Upscaling of the permeability or transmissibility field, in which local flow behavior is taken into account, is routinely done. As mentioned above, the bulk of the chemical reactions happen in a narrow combustion zone being less than a meter in thickness compared to standard gridblock sizes of, say, 50 meters. Thus, the spatial scale for chemical reactions is smaller than the smallest scale normally resolved in reservoir simulations. Consequently, the temperature profile on the simulation grid will be too smooth, and important phenomena such as ignition/extinction or quenching may not be predicted correctly.

Relating to temporal scale, a number of different processes may be identified in ISC, each having its own characteristic scale. Most of the existing ISC models include convective mass transport, heat transport by convection and conduction, kinetically controlled chemical reactions, and fluid phases in thermodynamic equilibrium (Crookston et al., 1979; Grabowski et al., 1979; Coats, 1980). The phase equilibrium assumption implicitly states that the timescales for the interphase mass transfer processes occurring when phases come to an equilibrium state, are much faster than all other timescales. Of the remaining processes, the chemical reactions are likely to occur on timescales that are again much faster than the scales for mass and heat transport.

Although being multiscale in nature, the question remains whether all the processes in ISC represent essential physics that needs to be resolved in a simulation. The goal of ISC simulation is to provide reliable predictions of performance, typically in terms of production, for a given ISC project. The production certainly depends on large scale features such as well placement, but the small scale behavior, spatial as well as temporal, in the combustion zone may be equally important. ISC processes are driven by chemical reactions, and chemical kinetics depends strongly on temperature. Thus failing to capture temperature peaks and, in general, smoothing out temperature profiles on too coarse a grid will lead to inaccurate prediction of reaction, which in turn will affect the amount of heat released and combustion gases evolved, ultimately resulting in wrong predictions of oil displacement. Ahead of the combustion front (see Figure 1.1) the oil is mobilized by a combination of steam, water, and gas drive. Lighter oil components will vaporize easily and be transported downstream. The compositional behavior in this region will determine the amount and composition of the oil left behind as fuel for the combustion. Therefore, accurate prediction of phase behavior as well as flow is likely to impact overall performance. Errors at this small scale will feed into overall production calculations, thereby rendering the results unreliable. Hence, the important processes in ISC are indeed multiscale with strong nonlinear interactions between different scales and efficient computational methods must be developed that handle this multiscale nature.

1.2.5 A review of ISC models

The majority of mathematical models for ISC emerged in the literature around 1980. Among the first researchers to develop a realistic model for ISC was Farouq Ali (1977). He presented a two-dimensional model with three phases (oil, water, and gas) and four fixed components (water, oil, oxygen, and inert gas). The oil component was assumed non-volatile, and the combustion process was modeled simply as direct oxidation of the oil component. Capillary effects were included. Heat was assumed to be transported by convection and conduction in the reservoir and by conduction to the underlying and overlying formations.

Crookston et al. (1979) and Grabowski et al. (1979) reported on the development of ISCOM, a general purpose thermal simulator which was the predecessor of the commercial code STARS (Steam, Thermal and Advanced Processes Reservoir Simulator) from Computer Modelling Group, Inc. The model operated in three dimensions and included a variable number of components distributed among four phases (water, oil, gas, and solid). The number and type of chemical reactions were variable and both capillary and gravity forces were included. Heat transfer was by convection and conduction in the reservoir and by conduction in the underlying and overlying formations. Mass transfer was allowed between all phases under equilibrium conditions.

Among the most comprehensive models reported so far is the model by Coats (1980). It included a variable number of components and reactions and allowed the components to be distributed in any or all of the four phases (water, oil, gas, and coke). Gravity and capillary forces were incorporated. The permeability field was allowed to change with changing concentration of coke. Heat transfer was by convection, conduction, and radiation within the reservoir and by conduction in the cap and base rock. All models discussed so far assumed kinetically controlled chemical reactions and modeled phase equilibrium using K-value correlations.

A fundamentally different approach was recently presented by Akkutlu and Yortsos (2003). Inspired by the filtration combustion literature, they proposed a one-dimensional model and devised an analytical solution. They used a transport limiting approach for reactions and treated the combustion zone as a discontinuous front and derived appropriate jump conditions relating the change in variables across the front. The problem then reduced to modeling the combustion front dynamics and the regions on either side of the front. The analytical framework was developed for a single reaction in homogeneous media, but in subsequent papers the authors considered extensions to layered systems (Akkutlu and Yortsos, 2002) and two sequential reactions (Akkutlu and Yortsos, 2004).

The industry standard today for ISC simulations is STARS (CMG, 2004). It is a multi-component, general purpose thermal simulator with capabilities for handling both equilibrium and kinetically controlled chemical reactions. The simulator has extensive features including coupling with a geomechanics module. It uses an ideal fluid description with K-value based phase equilibrium and ideal phase properties (e.g. densities and enthalpies). With respect to numerical solution techniques, the simulator implements a standard control-volume finite difference scheme with a fully implicit (FIM) time discretization and an option for use of the adaptive implicit method (AIM), where gridblock variables are treated either explicitly or implicitly based on local CFL (Courant-Friedrichs-Lewy) criteria. Recently the simulator was extended with dynamic gridding capabilities (Christensen et al., 2004) for tracking of fronts (e.g. combustion or steam). In its current version, functionality is not available for adapting to multiscale behavior in time by tailored timestepping for individual physical subprocesses such as convective transport and chemical reactions.

1.3 Motivation and objectives

ISC has already been proven as an effective recovery process, and the interest in the process is likely to increase dramatically over the next decades, both as a primary recovery process for the world's vast heavy oil reserves and as a tertiary process in waterflooded, light oil reservoirs. Predictive mathematical models and robust and efficient simulators are needed to improve our understanding of the ISC process and to enable safe and cost-effective design of ISC projects.

ISC is being successfully operated in (e.g. Kumar et al., 2007) and have been evaluated for (e.g. Stokka et al., 2005; Pascual et al., 2005) many light oil reservoirs. In light oil reservoirs, where flue gas drive is the dominating displacement mechanism, phase behavior is likely to be important. In general, compositional effects and their impact on reaction paths, and hence on overall process performance, are not fully understood for ISC processes. Tingas et al. (1996) note that the adequacy of the PVT package within a thermal simulator is severely tested in high pressure, light oil thermal processes. In addition, Tingas et al. (1996) comment on numerical convergence problems arising due to the inconsistency inherent in using an ideal mixture approach when modeling phase behavior (through K-value correlations), but taking into account non-idealities when modeling phase compressibilities using an Equation-of-State (EoS), which is common in some thermal simulators. Current models and commercial simulators all assume ideal mixtures when modeling phase behavior. These observations motivate the development of fully compositional, EoS based ISC models, as well as a study of the influence of phase behavior on reaction paths and especially on important phenomena such as ignition and extinction.

The multiscale challenge in ISC simulations may be approached by either attempting to resolve all relevant scales or by making use of appropriate subgrid scale models to represent the small scale processes. Subgrid scale modeling is not addressed in this work, but instead we concentrate on how to resolve different scales. In order to capture the essential process dynamics in a numerical simulation, the reaction kinetics must be integrated using timesteps that are much smaller than those necessary for capturing the effects of convection and conduction. An intuitive way of approaching this problem numerically is by operator splitting and fractional timestepping. Each global timestep then consists of a series of substeps, in which the individual terms are integrated separately, the advantage being that small timesteps can be applied only to those terms requiring high resolution. The separation of scales in the problem is thereby exploited numerically, the cost being a numerical error introduced by the splitting, since in each substep only one process is taken into account and the interaction with the other processes neglected.

The objectives of this work are:

- To develop ISC models, which are fully compositional, and which facilitate the study of ISC dynamics with the purpose of advancing the knowledge

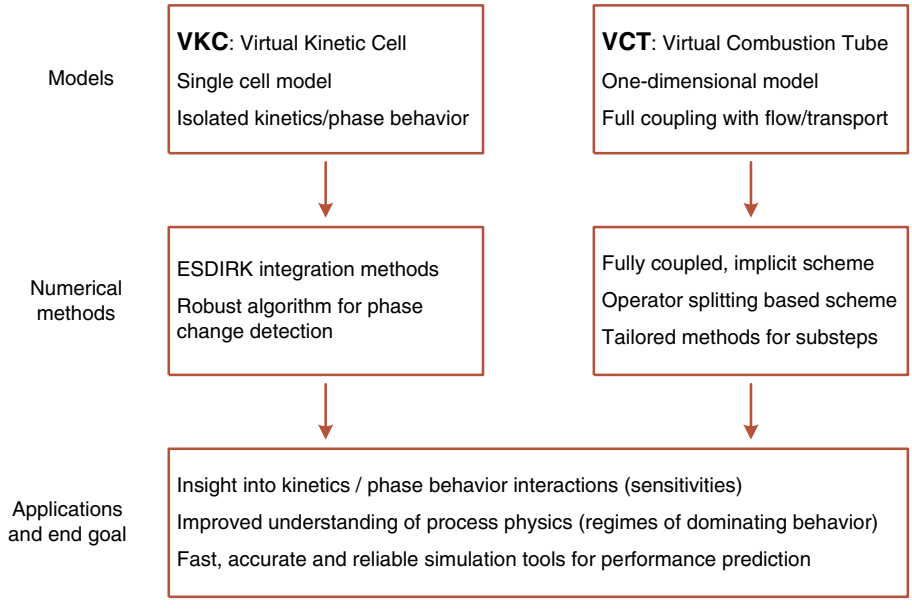

Figure 1.3: Main research directions and contributions.

state on ISC processes. In particular, the objective is to explore the interaction between kinetics and phase behavior and the impact of phase behavior treatment on ignition/extinction dynamics.

- To design numerical methods and algorithms, which are tailored to ISC problems, and which take into account the multiscale nature of the process by adapting to the underlying physics.

- To develop robust and efficient simulation tools implementing the numerical algorithms, in particular the algorithms for integration of chemical reactions subject to phase equilibrium constraints.

1.4 Main contributions

The contributions of this work should be seen together with parallel efforts at Stanford University, California, on other aspects of ISC modeling and simulation, in particular development of adaptive mesh refinement (AMR) techniques for efficient spatial resolution (Nilsson et al., 2005). The long-term goal of our research is the development of accurate, efficient, and reliable models and simulation tools for reactive EOR processes.

The work in this thesis is application-oriented and we emphasize the development of practical solutions to realistic problems. The main directions in this research and the resulting contributions are best described by considering Figure 1.3.

1.4.1 Models and algorithms

We propose two novel, fully compositional ISC models for laboratory scale combustion simulation. The Virtual Combustion Tube (VCT) is a one-dimensional thermal, reactive, and compositional model. It accounts for the simultaneous flow, transport of heat and mass, chemical reactions, and phase equilibrium. The Virtual Kinetic Cell (VKC) is a zero-dimensional version of the VCT. Essentially, the VKC models a multiphase, chemical batch reactor (a kinetic cell) where only chemical reactions and phase behavior are taken into account. It is designed to allow the isolated study of kinetics and phase behavior interactions. In both the VCT and VKC a dual strategy is implemented for phase behavior and fluid property modeling, using both a cubic EoS and an ideal mixture approach, where, in the latter, phase behavior is modeled from pressure-temperature K-value correlations. Together, the two models provide a flexible platform for the study and support of laboratory scale combustion experiments.

We propose a time integration scheme for ISC simulation based on operator splitting techniques. The scheme separates the flow and transport terms in the governing equations from the reaction terms and, hence, allows for integration of the subprocesses by specialized methods. We consider in detail the chemical kinetics substep and design a family of integration methods, which are based on the Runge-Kutta schemes, and which are well suited for integration of stiff kinetics with algebraic constraints due to phase behavior. Moreover, we address the problem of integrating across phase boundaries. Inspired by simulation techniques for hybrid-dynamic systems we extend the integration methods with algorithms for detecting and consistently locating phase changes, and we show that these algorithms improve integration robustness by reducing convergence and error test failures when crossing phase boundaries.

ISC processes rely critically on the sustained propagation of a high-temperature combustion front. We employ the models developed for the study of ignition/extinction phenomena in ISC as a function of operating conditions and the choice of phase behavior model. We quantify critical operation regimes, where a change of phase behavior model will change the state of the system from ignition to extinction or vice versa.

1.4.2 Tools

In order to test the models and numerical methods and algorithms, two simulation codes have been developed for the VKC and VCT, respectively. Although

these simulators are intended for research and developed primarily to demonstrate the models and algorithms developed in this thesis, a flexible and easily extensible code structure was emphasized throughout. All developments were carried out in the Fortran 90/95 language.

1.4.3 List of research papers

The following is a list of papers of relevance to the subject of the thesis, authored or co-authored by the author of this thesis, which have been published or submitted for publication:

Journal articles

[4] Kristensen, M. R., Gerritsen, M. G., Thomsen, P. G., Michelsen, M. L. and Stenby, E. H. (2008). An equation-of-state compositional in-situ combustion model: a study of phase behavior sensitivity. Submitted to *Transport in Porous Media*.

[3] Kristensen, M. R., Gerritsen, M. G., Thomsen, P. G., Michelsen, M. L., Stenby, E. H. (2007). Efficient integration of stiff kinetics with phase change detection for reactive reservoir processes. *Transport in Porous Media* **69**(3), 383–409.

[2] Jørgensen, J. B., Kristensen, M. R., Thomsen, P. G. (2007). A family of ESDIRK integration methods. Submitted to *SIAM Journal on Scientific Computing*.

[1] Kristensen, M. R., Jørgensen, J. B., Thomsen, P. G. and Jørgensen, S. B. (2004). An ESDIRK method with sensitivity analysis capabilities. *Computers and Chemical Engineering*, **28**(12), 2695–2707.

Conference papers

[5] Kristensen, M. R., Gerritsen, M. G., Thomsen, P. G., Michelsen, M. L. and Stenby, E. H. (2008). An equation-of-state compositional in-situ combustion model. SPE 113947. Accepted for presentation at the *SPE Improved Oil Recovery Symposium*, Tulsa, OK, April 21–23.

[4] Kristensen, M. R., Gerritsen, M. G., Thomsen, P. G., Michelsen, M. L. and Stenby, E. H. (2007). Integration of chemical reactions in reservoir simulation. In proceedings of the *28th International Energy Agency Symposium on Enhanced Oil Recovery*, Vedbæk, Denmark, September 4–7.

[3] Kristensen, M. R., Gerritsen, M. G., Thomsen, P. G., Michelsen, M. L. and Stenby, E. H. (2007). Coupling chemical kinetics and flashes in reactive, thermal and compositional reservoir simulation. SPE 106218. In proceedings of the *SPE Reservoir Simulation Symposium*, Houston, TX, February 26–28.

[2] Kristensen, M. R., Gerritsen, M. G., Thomsen, P. G., Michelsen, M. L. and Stenby, E. H. (2006). Efficient reaction integration for in-situ combustion simulation. In proceedings of the *27th International Energy Agency Symposium on Enhanced Oil Recovery*, Paris, France, September 19–22.

[1] Kristensen, M. R., Gerritsen, M. G., Thomsen, P. G., Michelsen, M. L. and Stenby, E. H. (2006). Efficient integration of stiff kinetics in reactive compositional and thermal porous media processes. In proceedings of the *10th European Conference on the Mathematics of Oil Recovery (ECMOR X)*, Amsterdam, The Netherlands, September 4–7.

1.5 Thesis outline

The thesis is organized into three main parts:

The first part (Chapters 2–4) serves as a general introduction and overview of the research. Besides the motivation and objective of the work, which has already been covered, the first part includes the development of mathematical and numerical models for the kinetic cell and the combustion tube along with some example simulation results to illustrate the behavior of ISC processes.

Chapter 2 presents a general model for reactive, thermal, multiphase, and multicomponent porous media flow. The model is simplified in two stages resulting in the combustion tube and kinetic cell models, respectively. Chapter 3 gives an overview of the numerical work in the thesis with details included in the research papers, an exception being the section on operator splitting integration, which has not yet been published as a research paper. Chapter 3 also includes a section on generalization of the phase change detection algorithm, presented in the first research paper, to EoS based phase behavior descriptions.

The second part of the thesis includes two research papers. The first paper (Chapter 5) discusses in detail the kinetic cell model and in particular the development of a class of efficient integration methods for the reaction subproblem in ISC simulations. In addition, the paper presents a novel algorithm for robust detection and location of phase changes. The second paper (Chapter 6) presents a fully compositional, EoS based ISC model. Based on a standard numerical model, the second paper focuses on understanding sensitivities to numerical errors and modeling errors. In particular, the paper studies the sensitivity to phase behavior modeling, both for the kinetic cell and the combustion tube models. To some extent the material presented in the research papers overlap with other parts of the thesis, but the research papers contain important results, which are not presented elsewhere.

Finally, the third part of the thesis contains two appendices, the first including details on derivation of the family of ESDIRK integration methods along with a complete list of coefficients for the methods, and the second including detailed input data for the simulations presented in the thesis.

Chapter 2

Mathematical modeling

We present in this chapter the mathematical model describing compositional, thermal, and reactive reservoir processes. We introduce it in a general form and discuss subsequently specific choices for constitutive models along with specialization of the general model to the one-dimensional VCT and zero-dimensional VKC, respectively.

2.1 General conservation equations

2.1.1 Common assumptions

A component in a reservoir can be transported by molecular diffusion and convection. The relative importance of these processes is measured by the Peclet number defined as the ratio of a characteristic time for diffusion to a characteristic time for convection. Peclet numbers for typical reservoir flows of interest are often large enough that the effects of diffusion can be neglected (Orr Jr., 2007). Similarly, heat can be transported in a reservoir by conduction and convection. As for mass transport, the relative importance of heat conduction and convection is measured by the heat Peclet number. Using typical reservoir parameters for flow rate, interwell distance, and heat diffusivity, it can be shown that the heat Peclet number is 1–3 orders of magnitude lower than the equivalent mass Peclet number. Thus, the effect of heat conduction is normally included in thermal simulation models. Especially in the start-up of ISC processes, when flow rates are small, heat conduction is important.

A condition generally assumed to prevail in ISC, as well as in all other reservoir processes, is that the fluids are in thermodynamic equilibrium at every point within the reservoir (Prats, 1986). This equilibrium assumption implicitly states that the timescales for the interphase mass transfer processes occurring when phases come to an equilibrium state, are much faster than all other timescales. Consider the simple example of an oil phase and a gas phase contained in a pore of diameter $1\,\mu$m. Using a typical value for a diffusion coefficient of $10^{-9}\,\mathrm{m}^2/\mathrm{s}$, the average time required for a molecule to diffuse across the pore would be on the order of $10^{-3}\,\mathrm{s}$. This time is likely to be much smaller than the time required for flow to change the compositions significantly within the pore. Thus, in a non-reacting system it is reasonable to assume thermodynamic equilibrium. The validity of the assumption for reactive systems is unclear, but in lack of better alternatives we shall assume thermodynamic equilibrium conditions.

In addition to thermodynamic equilibrium it is commonly assumed that the fluids and reservoir rock are in thermal equilibrium.

2.1.2 System specifications

We model a porous media system containing n_c chemical (pseudo) components distributed among three mobile fluid phases (oil, water, and gas) and one immobile solid phase. Components existing in the solid phase are assumed to do so exclusively. The mobile components are assumed to exist in at most two phases, with the water component partitioning into the water and gas phases, and the remaining components partitioning into the oil and gas phases. The chemical components are indexed as

$$i \in \mathcal{I} = \mathcal{I}^{ol} \cup \mathcal{I}^{w} \cup \mathcal{I}^{s}, \tag{2.1}$$

where

$$\begin{aligned} \mathcal{I}^{ol} &= \{1, \ldots, n_{ol}\}, \\ \mathcal{I}^{w} &= \{n_{ol}+1\}, \\ \mathcal{I}^{s} &= \{n_c - n_s + 1, \ldots, n_c\}. \end{aligned} \tag{2.2}$$

Thus, the total number of components is $n_c = n_{ol} + n_s + 1$.

We represent the porous medium by Ω with boundary $\mathcal{S} = \partial\Omega$ and outward pointing normal vector $\mathbf{n}$. Points in the domain are denoted $\mathbf{x} = [x\ y\ z]^T$. Intrinsic to the porous medium are the total bulk volume denoted, V_T, the void pore volume, V_p, and the void porosity, $\phi_v = {}^{V_p}/_{V_T}$. The pore space is entirely occupied by the fluid and solid phases. We assume that the reservoir rock is incompressible and chemically inert. It is convenient to define the fluid porosity, ϕ_f, relating the bulk volume to the volume open to flow. If $V_f = V^o + V^w + V^g$ denotes the total fluid volume, then the fluid porosity is given by

$$\phi_f \equiv \frac{V_f}{V_T} = \frac{V_p - V^s}{V_T} = \phi_v - \sum_{i \in \mathcal{I}^s} \frac{C_i}{\xi_i^s}, \tag{2.3}$$

where C_i is the concentration per unit bulk volume and ξ_i^s is the molar density of solid component i. The volumetric saturation of phase j is defined as

$$S^j = \frac{V^j}{V_f} = \frac{V^j}{\phi_f V_T}, \qquad j \in \{o, w, g\}. \tag{2.4}$$

2.1.3 Governing equations

The governing equations for thermal, compositional and reactive porous media flow can be derived from n_c component conservation equations, an energy conservation equation, and a volume conservation equation. The i-th component conservation equation can be written in integral form as

$$\frac{d}{dt}\int_\Omega C_i d\Omega + \int_\mathcal{S} \mathbf{q}_i^m \cdot \mathbf{n} d\mathcal{S} = \int_\Omega \left(Q_i^{m,reac} + Q_i^{m,well} \right) d\Omega, \tag{2.5}$$

where $i \in \mathcal{I}$, $\mathbf{q}_i^m$ is the mass flux, and $Q_i^{m,reac}$ and $Q_i^{m,well}$ are the mass source densities due to chemical reactions and wells, respectively. We can express the phase and total component concentrations as

$$c_i^j = \phi_f x_i^j \xi^j S^j, \qquad i \in \mathcal{I}^{ol} \cup \mathcal{I}^w \tag{2.6a}$$

$$C_i = \sum_j c_i^j, \tag{2.6b}$$

$$c_i^s = (\phi_v - \phi_f)\, x_i^s \xi^s, \qquad i \in \mathcal{I}^s, \tag{2.6c}$$

$$C_i = c_i^s, \tag{2.6d}$$

where $j \in \{o, g\}$ for $i \in \mathcal{I}^{ol}$, and $j \in \{w, g\}$ for $i \in \mathcal{I}^w$. x_i^j is the mole fraction of component i in phase j, and ξ^j is the molar density of phase j. In (2.5) we note that

$$\mathbf{q}_i^m = \mathbf{0}, \qquad i \in \mathcal{I}^s. \tag{2.7}$$

Neglecting capillary forces, we can express the component flux term in (2.5) using the standard multi-phase extension of Darcy's law

$$\mathbf{u}^j = -\frac{k_r^j}{\mu^j}\mathbf{k}\left(\nabla P - \rho^j g \nabla D\right), \tag{2.8}$$

where $\mathbf{u}^j$ is the phase flow velocity, $\mathbf{k}$ is the absolute permeability, k_r^j is the relative permeability, μ^j is the viscosity, ρ^j is the mass density, g is the gravitational constant, and D is the reservoir depth. The total component flux is the sum of the fluxes in the individual phases, given by

$$\mathbf{q}_i^m = \sum_j x_i^j \xi^j \mathbf{u}^j, \qquad i \in \mathcal{I}^{ol} \cup \mathcal{I}^w. \tag{2.9}$$

The energy conservation equation is

$$\frac{d}{dt}\int_{\Omega} U d\Omega + \int_{\mathcal{S}} \left(\mathbf{q}^{h,adv} + \mathbf{q}^{h,cond}\right) \cdot \mathbf{n} d\mathcal{S} = \int_{\Omega} \left(Q^{h,reac} + Q^{h,well}\right) d\Omega, \quad (2.10)$$

where U is the total internal energy of the system, $\mathbf{q}^{h,adv}$ is the heat transport due to advection, $\mathbf{q}^{h,cond}$ is the heat transport due to conduction, and $Q^{h,reac}$ and $Q^{h,well}$ are the heat source densities due to chemical reactions and wells, respectively. The total internal energy can be expressed as

$$U = (1 - \phi_v)\, U^r + (\phi_v - \phi_f)\, \xi^s U^s + \phi_f \sum_j \xi^j S^j U^j, \quad (2.11)$$

where U^r is the volumetric internal energy of the reservoir rock and U^j is the molar internal energy of phase j. The advective heat transport in (2.10) is the sum of the heat carried by each mobile phase

$$\mathbf{q}^{h,adv} = \sum_j h^j \xi^j \mathbf{u}^j, \quad (2.12)$$

where h^j is the molar enthalpy. Fourier's law is used to express the transport due to conduction

$$\mathbf{q}^{h,cond} = -\mathbf{k}_c \nabla T, \quad (2.13)$$

where the tensorial quantity $\mathbf{k}_c$ is the effective thermal conductivity of the saturated medium.

Finally, the principle of volume conservation expresses that the fluid and solid phases must fill the pore space exactly

$$V_p = \sum_j V^j, \quad (2.14)$$

where $j \in \{o, w, g, s\}$.

2.1.4 Phase equilibrium

In addition to the conservation requirements, we assume that the system is in thermodynamic equilibrium as expressed by the equality between chemical potentials, or equivalently fugacities, of a component in all phases. For components partitioning between the oil and gas phases we have

$$f_i^o = f_i^g, \qquad i \in \mathcal{I}^{ol}, \quad (2.15)$$

where f_i^j is the fugacity of component i in phase j.

2.2 Boundary conditions

We assume no flow of mass or heat across the reservoir boundaries corresponding to Neumann conditions

$$\mathbf{q}_i^m \cdot \mathbf{n} = 0, \qquad \mathbf{x} \in \partial\Omega, \tag{2.16a}$$

$$\left(\mathbf{q}^{h,adv} + \mathbf{q}^{h,cond}\right) \cdot \mathbf{n} = 0, \qquad \mathbf{x} \in \partial\Omega. \tag{2.16b}$$

We note that thermal reservoir models usually account for heat exchanges with the surroundings, typically through heat conduction to the reservoir cap and base rock (see e.g. Coats, 1980; Crookston et al., 1979). Since in this thesis we focus primarily on one-dimensional problems, we model heat exchanges as a source/sink term in the equation.

We consider wells completed in a single gridblock and two types of well operation: fixed single-phase injection rate for injectors and fixed back pressure for producers. Typically, a fixed gas rate (air or oxygen enriched air) is specified, or both water and gas rates are specified as for wet combustion processes. The wells are indexed as $w \in \mathcal{I}_w$, which consists of injectors and producers $\mathcal{I}_w = \mathcal{I}_w^{inj} \cup \mathcal{I}_w^{prod}$.

The component source density due to wells can be written as

$$Q_i^{m,well} = -\sum_j \frac{x_i^j \xi^j k_r^j}{\mu^j} \left(WI\right)_w \left(P - P_w\right), \qquad w \in \mathcal{I}_w^{prod} \tag{2.17}$$

for producers, where $\left(WI\right)_w$ is the well index, P is the block pressure, and P_w is the well bottom-hole pressure. For injectors, $Q_i^{m,well}$ can be computed directly from the specified injection rates. Again, since we are concerned primarily with one-dimensional combustion tube problems, we omit the well equation for injectors and include the injection rates directly in the equation. For standard block-centered grids the well index in (2.17) is

$$\left(WI\right)_w = \frac{2\pi kh}{\ln {}^{r_0}\!/_{r_w} + s}, \tag{2.18}$$

where k is the effective permeability, h is the formation thickness, r_w is the well radius, r_0 is the pressure equivalent radius, and s is a skin factor. Expressions for r_0 can be found in Aziz and Settari (1979) for general cartesian grids.

The heat source density due to wells can be written as

$$Q^{h,well} = -\sum_j \frac{h^j \xi^j k_r^j}{\mu^j} \left(WI\right)_w \left(P - P_w\right), \qquad w \in \mathcal{I}_w^{prod}. \tag{2.19}$$

Heat exchange with the surroundings is modeled using an external proportional heat controller

$$Q^{h,htr} = -u_a \left(T - T^{ext}\right), \tag{2.20}$$

where u_a is a heat transfer coefficient (or controller gain) and T^{ext} is the controller set point.

2.3 Constitutive models

The constitutive models for chemical kinetics, and rock and fluid properties are detailed in this section. To some extent this section overlaps with Section 6.10 in Paper II, but it is included here to give a complete presentation of the mathematical models.

2.3.1 Phase equilibrium

As mentioned in Section 1.4.1, we use a dual strategy for phase behavior and fluid property modeling, using both a cubic EoS and an ideal mixture approach, where, in the latter, phase behavior is modeled from pressure-temperature K-value correlations.

In the ideal mixture approach the K-values are calculated either from interpolation in tables generated from EoS flashes of the original oil or from the Wilson correlation

$$\ln K_i = \frac{P_i^{crit}}{P} + 5.373\,(1+\omega_i)\left(1 - \frac{T_i^{crit}}{T}\right), \tag{2.21}$$

where P_i^{crit}, T_i^{crit}, and ω_i are the critical pressure and temperature and accentric factor, respectively, for component i.

In the EoS approach, the fugacities in (2.15) are obtained from a cubic EoS of the form

$$\left(Z^j\right)^3 + c_2\left(Z^j\right)^2 + c_1\left(Z^j\right) + c_0 = 0, \tag{2.22}$$

where Z^j is the phase compressibility factor. The coefficients c_2, c_1 and c_0 depend on pressure, temperature and phase composition. A common choice of EoS in reservoir simulation is the Peng-Robinson equation (Peng and Robinson, 1976), which is used in this work. Details on the EoS and computation of fugacities can be found in e.g. Michelsen and Mollerup (2004) or Whitson and Brule (2000).

2.3.2 Chemical reactions

All chemical reactions are assumed to be kinetically driven. The reactions are modeled using standard Arrhenius rate relations, where the rates depend on component concentrations in a specific phase. Both homogeneous and heterogeneous reactions are allowed. n_r chemical reactions are assumed to occur, which are indexed as $\gamma \in \mathcal{I}^{rx}$. Let $\mathbf{A} \in \mathbb{R}^{n_c \times n_r}$ denote the stoichiometry matrix, where element $A_{i\gamma}$ is the stoichiometry coefficient for component i in reaction γ (negative for reactants, positive for products). To conserve mass, the constraint

$$\mathbf{M}^T\mathbf{A} = \mathbf{0} \tag{2.23}$$

must hold, where $\mathbf{M} = [M_1 \cdots M_{n_c}]^T$ is the vector of component molecular weights. Generally, two kinds of reactions dominate in ISC processes: cracking/pyrolysis reactions and oxidation (full/partial) reactions. For oxidation reactions the partial pressure of oxygen is used in the rate expressions. If the set of triples $(i, j, m) \in \mathcal{J}(\gamma)$ index the involved reactants, phases and reaction orders for reaction γ, then the reaction rate may be expressed as

$$R_\gamma = K_\gamma \left(P x^g_{O_2}\right)^{n_\gamma} \prod_{(i,j,m)\in\mathcal{J}(\gamma)} \left(c_i^j\right)^m, \tag{2.24}$$

where n_γ is the reaction order in oxygen partial pressure and c_i^j is the concentration of component i in phase j according to the definitions (2.6a) and (2.6c). The rate constants are temperature dependent according to Arrhenius's law

$$K_\gamma = \alpha_\gamma \exp\left(-\frac{E_a^\gamma}{R_g T}\right), \tag{2.25}$$

where α_γ is the frequency factor, E_a^γ is the activation energy and R_g is the universal gas constant.

From the reaction rates we can express the mass and heat source densities in (2.5) and (2.10). The net production of component i in chemical reactions is

$$Q_i^{m,reac} = \sum_\gamma A_{i\gamma} R_\gamma. \tag{2.26}$$

Similarly, the net heat generation is

$$Q^{h,reac} = \sum_\gamma (-\Delta H)^r_\gamma R_\gamma, \tag{2.27}$$

where $-\Delta H^r$ is the heat of reaction.

2.3.3 Rock and fluid properties

Depending on the phase behavior treatment we use either ideal or EoS based fluid properties, and we present in this section an overview of the models and correlations implemented for both approaches.

Relative permeability

Three-phase relative permeabilities are, in general, obtained from two-phase experiments, where the relative permeability of the "middle" phase is interpolated from two-phase data. We use the Stone II model (Stone, 1973) to calculate oil phase relative permeability from water-oil and gas-oil curves, which can be entered either as tables or correlations. Temperature effects and possible wettability changes due to chemical reactions (e.g. deposition of coke) have not been considered in this work.

Density

Phase densities are evaluated from the EoS by solving Eqn. (2.22) for Z^j. The molar and mass phase densities are

$$\xi^j = \frac{P}{R_g T Z^j}, \qquad \rho^j = \xi^j \sum_i x_i^j M_i. \tag{2.28}$$

In the ideal case we assume $Z^g = 1$ and obtain pure component liquid densities from

$$\xi_i^o = \xi_{i,ref}^o \exp\left(c_i^p(P - P_{ref}) - c_i^t(T - T_{ref})\right), \tag{2.29}$$

where $\xi_{i,ref}^o$ is the density at the reference consitions, and c_i^p and c_i^t are the compressibility and thermal expansion coefficients, respectively. Linear mixing of molar volumes is assumed

$$\frac{1}{\xi^o} = \sum_i \frac{x_i^o}{\xi_i^o}. \tag{2.30}$$

Water density is calculated according to a correlation similar to (2.29).

Viscosity

Accurate modeling of oil phase viscosity is important for ISC processes, since the reduction in oil viscosity with temperature is the primary mechanism for enhanced recovery. Pure component viscosities can be entered either through tables or obtained from the correlation

$$\mu_i^o = a_i^o \exp\left(\frac{b_i^o}{T}\right), \tag{2.31}$$

where a_i^o and b_i^o are correlation constants. The oil phase viscosity is then obtained by logarithmic mixing of the pure component viscosities

$$\ln \mu^o = \sum_i x_i^o \ln \mu_i^o. \tag{2.32}$$

Accuracy in gas phase viscosity is generally less important. The correlation used here is

$$\mu_i^g = a_i^g T^{b_i^g}, \tag{2.33}$$

and the mixing rule used is

$$\mu^g = \sum_i \frac{x_i^g \sqrt{M_i} \mu_i^g}{x_i^g \sqrt{M_i}}. \tag{2.34}$$

Water viscosity is obtained from a correlation similar to (2.31).

Enthalpy

Phase enthalpies are computed from ideal gas heat capacity correlations and vaporization enthalpy correlations. For a pure component gas we have

$$C_{p,i}(T) = C_{p,i}^1 + C_{p,i}^2 T + C_{p,i}^3 T^2 + C_{p,i}^4 T^3, \tag{2.35a}$$

$$h_i^{g,id} = \int_{T_{ref}}^{T} C_{p,i}(\bar{T}) d\bar{T}, \tag{2.35b}$$

where T_{ref} is the temperature of the reference state. In the ideal case the vaporization enthalpy is obtained from the correlation (CMG, 2004)

$$h_i^{vap} = hv_i^1 \left(T_i^{crit} - T\right)^{hv_i^2}, \tag{2.36}$$

where hv_i^1 and hv_i^2 are correlation constants. Thus, for the ideal case we have

$$h^g = \sum_i x_i^g h_i^{g,id} \tag{2.37a}$$

for the gas phase and

$$h^o = \sum_i x_i^o \left(h_i^{g,id} - h_i^{vap}\right) \tag{2.37b}$$

for the oil phase. In the non-ideal case the residual enthalpies are obtained from the EoS leading to

$$h^g = \sum_i x_i^g h_i^{g,id} + h^{g,res} \tag{2.38a}$$

$$h^o = \sum_i x_i^o h_i^{g,id} + h^{o,res}, \tag{2.38b}$$

where $h^{j,res}$ is the residual enthalpy of phase j. The water phase enthalpy is obtained from correlations similar to (2.35) and (2.36).

Internal energy

The volumetric internal energy of the reservoir rock is modeled as

$$C_v(T) = C_v^1 + C_v^2 T, \tag{2.39a}$$

$$U^r = \int_{T_{ref}}^{T} C_v(\bar{T}) d\bar{T}. \tag{2.39b}$$

The solid phase heat capacity is assumed constant, and the molar internal energy of the fluid phases is obtained from the enthalpy by subtraction of the mechanical work

$$U^j = h^j - \frac{P}{\xi^j}, \qquad j \in \{o, w, g\}. \tag{2.40}$$

Thermal conductivity

The mobile and immobile phases have associated with them a scalar thermal conductivity k_c^j. Moreover, the rock has an associated tensorial thermal conductivity, denoted $\mathbf{k}_c^r$. The effective thermal conductivity of the saturated porous medium is computed as a weighted volume average

$$\mathbf{k}_c = (1-\phi_v)\,\mathbf{k}_c^r + \left[(\phi_v - \phi_f)\,k_c^s + \phi_f \sum_j S^j k_c^j\right]\mathbf{I}, \tag{2.41}$$

where $\mathbf{I}$ denotes the identity matrix. In this thesis we assume the rock conductivity to be isotropic.

2.4 Primary equations and variables

According to Gibbs' phase rule, to fix the intensive state of a system with n_c components and n_p phases, we must specify

$$f = n_c - n_p + 2 \tag{2.42}$$

intensive variables. Since the bulk volume, V_T, is a known quantity, we need an additional $n_p - 1$ phase volume fractions (saturations) to fix the amounts of each phase and thereby the extensive state of the system. Consequently, the number of degress of freedom is

$$n_c - n_p + 2 + (n_p - 1) = n_c + 1. \tag{2.43}$$

In a thermal-compositional reservoir model the state of the system is therefore uniquely determined by $n_c + 1$ independent variables. Thus, we must select $n_c + 1$ primary variables and equations when solving the model.

The natural choice of primary equations are the n_c mass balances (2.5) and the energy balance (2.10). For the choice of variables there are, however, several possibilities. Cao (2002) review compositional models and group them according to choice of variables. Generally, there are two classes of variable sets: *natural variables* and *overall quantity variables*. Natural variables are based on saturations and mole fractions, whereas overall quantity variables are based on total amounts of each component. The argument, often made in favor of natural variables, is that they appear *naturally* in the conservation equations, and that derivatives (needed in implicit formulations) therefore are straightforward and inexpensive to compute. When working with overall quantities (such as total moles of each component) as variables, some derivatives will be more expensive to evaluate, which increases the cost of Jacobian computations. The main drawback of natural variables is the need to switch variables when the phase state in a gridblock changes. Since natural variables are intensive phase properties,

disappearance or reappearance of a phase requires a switch of primary variables, because the phase properties are only defined when the phase is present. Variable switching is administratively difficult and may affect convergence of the nonlinear iterations in implicit formulations.

In reactive systems, a reformulation of the governing equations is often used based on the *extent of reaction* (Aris, 1989). For single phase, batch reactor problems this is straightforward and leads to a system of equations in n_r unknowns instead of n_c, where n_r is the number of independent chemical reactions. The extent of reaction concept has been generalized to open systems involving flow (Friedly, 1991; Friedly and Rubin, 1992). For certain reactive porous media transport problems in water resources modeling this generalized extent of reaction formulation leads to a reduced and simpler set of equations to be solved (Friedly and Rubin, 1992; Kräutle and Knabner, 2005). For multiphase ISC problems, however, where the transport operator is nonlinear and components move between phases due to phase behavior, the reformulation is not directly applicable.

In this thesis we choose as primary variables the n_c overall component concentrations, C_i, and temperature and pressure. With overall quantities as variables, we avoid the complicated variable switching logic when phases change. Since the volume constraint (2.14) is nonlinear in the primary variables, we include it as an additional primary equation and work with the full set of component concentrations. Thus, we solve simultaneously a set of $n_c + 2$ equations per gridblock, where temperature is aligned with the energy balance, pressure is aligned with the volume constraint, and the component concentrations are aligned with the respective component balances. We note that the volume constraint as well as the component balances for all immobile solid components can be eliminated from the primary equation set at the Jacobian level, since both types of equations are local to each gridblock.

The choice of primary equations and variables affects the convergence properties of the nonlinear and linear systems arising in implicit discretizations (Cao, 2002). Haukås (2006) has studied the problem of choosing primary equations and variables for optimal nonlinear convergence in compositional models, but we shall not pursue the problem further here.

2.5 A virtual laboratory

The model presented above has been implemented in two different forms: (i) as a Virtual Combustion Tube (VCT) and (ii) as a Virtual Kinetic Cell (VKC). The VCT and VKC constitute the main modeling contributions of this work.

2.5.1 A virtual combustion tube (VCT)

The VCT is a one-dimensional version of the general model presented above. In Chapter 3 we discuss numerical models for solving the VCT equations, and in Paper II in Chapter 6 we validate the model through convergence studies and comparisons with the commercial simulator STARS.

2.5.2 A virtual kinetic cell (VKC)

The VKC is essentially a zero-dimensional version of the general model. It accounts for chemical reactions in a multiphase batch reactor with simple source and sink terms. The VKC is proposed and discussed in Paper I in Chapter 5 and further extended in Kristensen et al. (2007*a*).

The VKC equations can be expressed in the following form

$$\frac{dC_i}{dt} = Q_i^{m,reac} + Q_i^{m,well}, \qquad i \in \mathcal{I}, \tag{2.44a}$$

$$\frac{dU}{dt} = Q^{h,reac} + Q^{h,well} + Q^{h,htr}, \tag{2.44b}$$

$$0 = V_p - \sum_j V^j, \tag{2.44c}$$

$$0 = f_i^g - f_i^o, \qquad i \in \mathcal{I}^{ol}, \tag{2.44d}$$

where $Q^{h,htr}$ is defined by (2.20) and the mass and heat source densities due to wells are given by (2.17) and (2.19), respectively, with the modification that only the gas phase is assumed to leak out of the cell.

Chapter 3

Numerical modeling

This chapter presents the numerical methods for solving the models developed in the previous chapter. We consider first a fully coupled, implicit solution approach based on a control-volume discretization. In Section 3.2 we propose an integration scheme based on operator splitting techniques, where the flow and transport processes are separated from the reaction process in a sequence of integration steps. This separation of the problem into substeps enables the use of specialized methods for integration of the individual processes. Section 3.3 focusses on the reaction process and highlights the development of a class of tailored Runge-Kutta methods, the details of which are presented in Paper I in Chapter 5 and in Appendix A. Section 3.4 discusses the extension of the integration methods with an algorithm for robust treatment of phase changes. Finally, in Section 3.5 we discuss the development of a simulator for ISC and comment on the design choices made.

3.1 Fully coupled, implicit scheme (FIM)

We consider first a fully implicit (FIM), control-volume based scheme for discretization of the governing equations. This scheme is common in reservoir simulation, and it is also implemented in the STARS simulator (CMG, 2004), which allows us to validate our simulator with this commercial simulator. We note that Coats (1980) also uses a fully implicit approach when solving ISC equations, whereas Crookston et al. (1979) use a mixture of implicit and explicit treatment in the reaction and interblock fluid transmissibility terms.

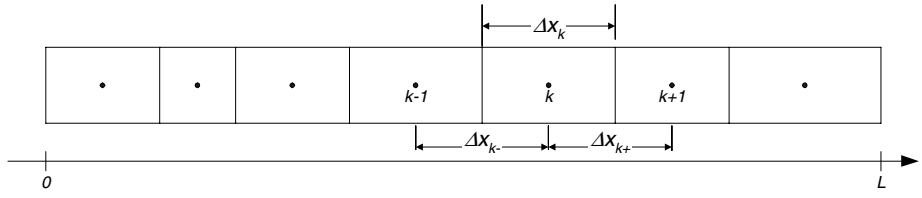

Figure 3.1: One-dimensional block-centered cartesian grid.

3.1.1 Spatial discretization

The discrete 1D domain is represented by a variable volume, block-centered grid as illustrated in Figure 3.1. Each block in the domain is regarded as a small control volume V_b, and the grid nodes are taken as the centers of each block. The grid is denoted as

$$\Omega_{\Delta x} = \{\Delta x_k \ : \ k = 1, \ldots, N_b\}\,. \tag{3.1}$$

The constraint $L = \sum \Delta x_k$ is assumed to hold. The location of node k in the domain is

$$x_k = \frac{\Delta x_k}{2} + \sum_{i=1}^{k-1} \Delta x_i. \tag{3.2}$$

Apart from the gridblock size, Δx_k, the following internode distances are defined

$$\Delta x_{k+} = x_{k+1} - x_k \tag{3.3a}$$
$$\Delta x_{k-} = x_k - x_{k-1}. \tag{3.3b}$$

We use a standard two-point flux approximation for discretization of the flux terms. Let $S_k = \{S_{k+1/2}, S_{k-1/2}\}$ denote the surfaces of gridblock k. Substituting (2.8) and (2.9) in (2.5) and introducing the flow potential

$$\nabla\Phi^j = \nabla P - \rho^j g \nabla D, \tag{3.4}$$

the flux terms can then be discretized as

$$\begin{aligned}\int_{S_k} \mathbf{q}_i^m \cdot \mathbf{n} d\mathcal{S} &= -\int_{S_k} \sum_j \frac{x_i^j \xi^j k_r^j}{\mu^j} \mathbf{k} \nabla\Phi^j \cdot \mathbf{n} d\mathcal{S} \\ &\simeq \sum_j \Lambda^j_{i,k+1/2} T_{k+1/2} \Delta^+ \Phi^j_k - \Lambda^j_{i,k-1/2} T_{k-1/2} \Delta^- \Phi^j_k,\end{aligned} \tag{3.5}$$

where $T_{k\pm1/2}$ is the transmissibility for the gridblock connections

$$T_{k\pm1/2} = \left(\frac{S_{k\pm1/2} k_{k\pm1/2}}{\Delta x_{k\pm}} \right). \tag{3.6}$$

Harmonic averages of block permeabilities are used in the evaluation of $k_{k\pm 1/2}$. $\Lambda^j_{i,k\pm 1/2}$ in (3.5) is the generalized mobility

$$\Lambda^j_{i,k\pm 1/2} = \left(\frac{x_i^j \xi^j k_r^j}{\mu^j} \right)_{k\pm 1/2}, \tag{3.7}$$

which is evaluated in the upstream direction. The discrete flow potentials are

$$\begin{aligned} \Delta^+ \Phi_k^j &= P_{k+1} - P_k - \rho^j_{k+1/2} g \left(D_{k+1} - D_k \right) \\ \Delta^- \Phi_k^j &= P_k - P_{k-1} - \rho^j_{k-1/2} g \left(D_k - D_{k-1} \right), \end{aligned} \tag{3.8}$$

where the mass density in the gravity term is evaluated as a saturation weighted average

$$\rho^j_{k\pm 1/2} = \frac{S^j_{k\pm 1} \rho^j_{k\pm 1} + S^j_k \rho^j_k}{S^j_{k\pm 1} + S^j_k}. \tag{3.9}$$

The heat flux terms in (2.10) are discretized in a similar way

$$\begin{aligned} \int_{S_k} \left(\mathbf{q}^{h,adv} + \mathbf{q}^{h,cond} \right) \cdot \mathbf{n} d\mathcal{S} &= - \int_{S_k} \left(\sum_j \frac{h^j \xi^j k_r^j}{\mu^j} \mathbf{k} \nabla \Phi^j + \mathbf{k}_c \nabla T \right) \cdot \mathbf{n} d\mathcal{S} \\ &\simeq \sum_j \Lambda^{j,h}_{k+1/2} T_{k+1/2} \Delta^+ \Phi^j_k - \Lambda^{j,h}_{k-1/2} T_{k-1/2} \Delta^- \Phi^j_k \\ &\quad + \frac{S_{k+1/2} k_{c,k+1/2}}{\Delta x_{k+}} \Delta^+ T_k - \frac{S_{k-1/2} k_{c,k-1/2}}{\Delta x_{k-}} \Delta^- T_k, \end{aligned} \tag{3.10}$$

where the fluid dependent parts of the interface heat conductivity $k_{c,k\pm 1/2}$ are evaluated upstream in temperature (see Section 2.3.3 for calculation of the effective heat conductivity), and the rock heat conductivity is evaluated as a harmonic average of the block conductivities. The fluid dependent part in the discretized advective term is

$$\Lambda^{j,h}_{k\pm 1/2} = \left(\frac{h^j \xi^j k_r^j}{\mu^j} \right)_{k\pm 1/2}. \tag{3.11}$$

3.1.2 Temporal discretization

The time derivatives in (2.5) and (2.10) are discretized using the first order Euler scheme

$$\frac{d}{dt} \int_{V_b} C_i dV_b \simeq \frac{(C_i V_b)^{n+1} - (C_i V_b)^n}{\Delta t} = \frac{C_i^{n+1} - C_i^n}{\Delta t} V_b, \tag{3.12a}$$

$$\frac{d}{dt} \int_{V_b} U dV_b \simeq \frac{(U V_b)^{n+1} - (U V_b)^n}{\Delta t} = \frac{U^{n+1} - U^n}{\Delta t} V_b. \tag{3.12b}$$

Evaluating the flux and source terms at time level t^{n+1} results in a fully implicit method (i.e. the Implicit Euler scheme).

3.1.3 Solution of nonlinear algebraic equations

If we substitute all the discretized terms in the governing equations, we can summarize the set of discrete primary equations as

$$\begin{aligned} 0 = \frac{C_{i,k}^{n+1} - C_{i,k}^{n}}{\Delta t} - \left[Q_i^{m,reac} + Q_i^{m,well} \right]_k^{n+1} \\ + \frac{1}{V_b} \left[\sum_j \Lambda_{i,k+1/2}^{j} T_{k+1/2} \Delta^+ \Phi_k^j - \Lambda_{i,k-1/2}^{j} T_{k-1/2} \Delta^- \Phi_k^j \right]^{n+1}, \end{aligned} \tag{3.13a}$$

$$\begin{aligned} 0 = \frac{U_k^{n+1} - U_k^{n}}{\Delta t} - \left[Q^{h,reac} + Q^{h,well} \right]_k^{n+1} \\ + \frac{1}{V_b} \left[\sum_j \Lambda_{k+1/2}^{j,h} T_{k+1/2} \Delta^+ \Phi_k^j - \Lambda_{k-1/2}^{j,h} T_{k-1/2} \Delta^- \Phi_k^j \right. \\ \left. + \frac{S_{k+1/2} k_{c,k+1/2}}{\Delta x_{k+}} \Delta^+ T_k - \frac{S_{k-1/2} k_{c,k-1/2}}{\Delta x_{k-}} \Delta^- T_k \right]^{n+1}, \end{aligned} \tag{3.13b}$$

$$0 = V_p - \left[\sum_j V^j \right]_k^{n+1}. \tag{3.13c}$$

The primary equations are nonlinear with respect to the chosen variables, so in order to advance one step in an implicit method, we must solve the system of nonlinear algebraic equations (3.13) using an iterative approach. We denote by $\mathbf{R} \in \mathbb{R}^{N_b(n_c+2)}$ the vector of residuals of the primary equations in (3.13) and let $\mathbf{u} \in \mathbb{R}^{N_b(n_c+2)}$ denote the vector of primary variables

$$\mathbf{u} = \begin{bmatrix} \mathbf{u}_1 \\ \vdots \\ \mathbf{u}_{N_b} \end{bmatrix}, \qquad \mathbf{u}_k = \begin{bmatrix} \mathbf{C} \\ T \\ P \end{bmatrix}_k, \qquad \mathbf{C}_k = \begin{bmatrix} C_i \\ \vdots \\ C_{n_c} \end{bmatrix}_k. \tag{3.14}$$

Thus, in each timestep we must solve

$$\mathbf{R}(\mathbf{u}) = \mathbf{0}. \tag{3.15}$$

From an initial guess for the solution, $\mathbf{u}^{(l)}$, we solve (3.15) using Newton-Raphson iterations

$$\left(\frac{\partial \mathbf{R}}{\partial \mathbf{u}} \right)^{(l)} \Delta \mathbf{u}^{(l+1)} = -\mathbf{R}^{(l)}, \tag{3.16a}$$

$$\mathbf{u}^{(l+1)} = \mathbf{u}^{(l)} + \Delta \mathbf{u}^{(l+1)}. \tag{3.16b}$$

For a 1D grid, the Jacobian of $\mathbf{R}$ in (3.16) is block tri-diagonal with blocks of size $(n_c + 2) \times (n_c + 2)$.

3.1.4 Phase equilibrium calculations

In order to evaluate all the terms in (3.13) we need, in addition to the primary variables, the compositions of each phase. The phase compositions are secondary variables in this formulation, and the equilibrium constraints (2.15) are the secondary equations. The equilibrium constraints can be solved together with the primary equations with elimination of the constraint equations at the Jacobian level, a technique described in e.g. Cao (2002). In this way, both primary and secondary equations are converged simultaneously. Alternatively, we can perform exact phase equilibrium calculations (flashes) in each Newton iteration for the primary equations. In the simultaneous approach, challenges in the phase equilibrium calculations may affect the convergence of the primary equations (Haukås, 2006). Using a staggered approach, on the other hand, separate flashes are performed in each primary iteration, which may be computationally more expensive, but is administratively simpler and has the advantage that optimized, stand-alone flash routines can be used. We use the staggered approach in the 1D simulator, but a simultaneous approach in the VKC, which is discussed in Section 3.4 and in Paper I in Chapter 5.

In the ideal mixture approach, where K-values are explicit functions of temperature and pressure, the two-phase flash computation reduces to solving the Rachford-Rice equation

$$\sum_{i \in \mathcal{I}^{ol}} (x_i^g - x_i^o) = \sum_{i \in \mathcal{I}^{ol}} \frac{z_i(K_i - 1)}{1 - \beta^g + \beta^g K_i}, \tag{3.17}$$

where $z_i = {}^{C_i}/_{\sum_i C_i}$, $i \in \mathcal{I}^{ol}$, is the overall mole fraction of component i and β^g is the overall molar phase fraction of gas. The phase compositions are

$$x_i^o = \frac{z_i}{1 - \beta^g + \beta^g K_i}, \qquad x_i^g = \frac{K_i z_i}{1 - \beta^g + \beta^g K_i}. \tag{3.18}$$

In the non-ideal case, where K-values are also functions of composition, we must solve the equilibrium constraints (2.15). The computational approach generally depends on the quality of the initial estimates. In the initialization phase of a simulation, where no previous information regarding phase compositions is available, we use an accelerated successive substitution approach with a switch to a second order Gibbs energy minimization procedure for final convergence. In subsequent flashes we use the compositions from the previous iteration (in the primary equations) or timestep as starting guesses and proceed directly to the second order minimization procedure. We refer to Michelsen and Mollerup (2004) for further details.

Regardless of the phase behavior treatment for components partitioning between the gas and oil phases, we assume that the partitioning of the water component between the gas and water phases can be modeled using a simple K-value correlation, and that the presence of water in the gas phase does not affect the two-phase gas-oil equilibrium. This assumption simplifies the equilibrium calculation considerably. An exception from this approach is discussed in Section 3.4 for the VKC.

3.2 Operator splitting based scheme

In the fully coupled, implicit approach, as outlined above, all processes (flow, transport, reaction) are integrated in the same way. The advantages of this approach are the unconditional stability of the scheme and the relative ease of its implementation. The scheme does not, however, address the underlying multiscale character of the equations, where the timescales for chemical reactions are often much faster than the timescales for advective transport, and where the scales can vary substantially over the duration of the combustion process as well as over the reservoir domain. Hence, in order to retain accuracy in the solution and capture the important dynamics of the system, the integration timestep in a fully coupled approach must be consistent with the fastest scale in the system, i.e. the reaction scale. Moreover, regardless of the appropriate timestep to capture the dynamics of the system, timesteps are often limited, despite the implicitness, by convergence problems when solving the large systems of nonlinear algebraic equations arising in the discretization (Younis and Gerritsen, 2006).

To overcome some of the drawbacks of the fully coupled, implicit approach, we propose in this section an integration scheme based on *operator splitting*. The general idea behind splitting is to break down the time integration process for a complicated problem into smaller parts, such that the different parts can be solved with suitable integration methods. For example, advective transport can often be integrated by explicit methods, whereas stiff chemical kinetics is best treated by implicit methods.

3.2.1 Operator splitting methods

Following Hundsdorfer and Verwer (2003) we can illustrate the splitting idea by considering the semi-discrete PDE

$$\frac{d\mathbf{w}}{dt} = \mathbf{f}\left(\mathbf{w}_1, \mathbf{w}_2\right) = \mathbf{f}^A\left(\mathbf{w}_1, \mathbf{w}_2\right) + \mathbf{f}^R\left(\mathbf{w}_1, \mathbf{w}_2\right), \tag{3.19}$$

where $\mathbf{f}^A$ and $\mathbf{f}^R$ denote discrete advection and reaction operators, respectively, and $\mathbf{w}_1$ and $\mathbf{w}_2$ denote two different variables, for example pressure and saturation. Generally, operator splitting methods can be grouped in two categories:

Implicit-Explicit (IMEX) methods and Additive Splitting (ADS) (or Locally One-Dimensional (LOD) (Hundsdorfer and Verwer, 2003)) methods.

ADS methods can be applied to additively separable operators, such as advection and reaction in the ISC problem. The global integration step is decomposed into a number of substeps, where in each substep only one operator (i.e. one physical process), or a subset of operators, is considered. The solutions to each substep are not consistent with the full equation. A consistent approximation is only formed at the end of all substeps.

In addition to numerical errors introduced when integrating each substep in the scheme, a splitting method also introduces an approximation error, referred to as a *splitting error*, due to the splitting itself. A simple, first order accurate ADS splitting for (3.19) is

$$\begin{aligned}
\frac{d\mathbf{w}^{(1)}}{dt} &= \mathbf{f}^A\left(\mathbf{w}_1^{(1)}, \mathbf{w}_2^{(1)}\right), \qquad t \in \left[t^n, t^{n+1}\right], \quad \mathbf{w}^{(1)}(t^n) = \mathbf{w}^n, \\
\frac{d\mathbf{w}^{(2)}}{dt} &= \mathbf{f}^R\left(\mathbf{w}_1^{(2)}, \mathbf{w}_2^{(2)}\right), \qquad t \in \left[t^n, t^{n+1}\right], \quad \mathbf{w}^{(2)}(t^n) = \mathbf{w}^{(1)}(t^{n+1}),
\end{aligned} \tag{3.20}$$

giving $\mathbf{w}^{n+1} = \mathbf{w}^{(2)}(t^{n+1})$ as the approximation at t^{n+1}. A symmetrical, second order accurate splitting, known as *Strang splitting* (Strang, 1968), can be achieved in the following way

$$\begin{aligned}
\frac{d\mathbf{w}^{(1)}}{dt} &= \mathbf{f}^A\left(\mathbf{w}_1^{(1)}, \mathbf{w}_2^{(1)}\right), \quad t \in \left[t^n, t^{n+1/2}\right], \quad \mathbf{w}^{(1)}(t^n) = \mathbf{w}^n, \\
\frac{d\mathbf{w}^{(2)}}{dt} &= \mathbf{f}^R\left(\mathbf{w}_1^{(2)}, \mathbf{w}_2^{(2)}\right), \quad t \in \left[t^n, t^{n+1}\right], \quad \mathbf{w}^{(2)}(t^n) = \mathbf{w}^{(1)}(t^{n+1/2}), \\
\frac{d\mathbf{w}^{(3)}}{dt} &= \mathbf{f}^A\left(\mathbf{w}_1^{(3)}, \mathbf{w}_2^{(3)}\right), \quad t \in \left[t^{n+1/2}, t^{n+1}\right], \quad \mathbf{w}^{(3)}(t^{n+1/2}) = \mathbf{w}^{(2)}(t^{n+1}),
\end{aligned} \tag{3.21}$$

giving $\mathbf{w}^{n+1} = \mathbf{w}^{(3)}(t^{n+1})$ as the approximation at t^{n+1}. Here, the advection step is symmetrically split in half. This concept of introducing *fractional steps* at the splitting scheme level can be generalized to design higher order splitting methods (Hundsdorfer and Verwer, 2003). Fractional steps can also be introduced at the substep level. ADS methods define a global timestep, which is the overall timestep of the splitting scheme, but subprocesses can be integrated with smaller timesteps, which are appropriate for each physical process. In addition to individual timestepping, the substeps in (3.20) and (3.21) can be integrated with specialized numerical methods. As such, ADS methods provide a flexible framework for designing tailored integration schemes for complex, multiscale processes.

In IMEX methods the overall equation is not decoupled in the same sense as for ADS methods. A single integration scheme is applied, but the operator variables are treated either explicitly or implicitly. The choice of explicit or implicit treatment can be made for the entire equation or for each individual

operator as illustrated by

$$\mathbf{w}^{n+1} = \mathbf{w}^n + \Delta t \mathbf{f}\left(\mathbf{w}_1^{n+1}, \mathbf{w}_2^n\right), \tag{3.22}$$

$$\mathbf{w}^{n+1} = \mathbf{w}^n + \Delta t \left[\mathbf{f}^A\left(\mathbf{w}_1^{n+1}, \mathbf{w}_2^n\right) + \mathbf{f}^R\left(\mathbf{w}_1^n, \mathbf{w}_2^{n+1}\right)\right]. \tag{3.23}$$

The familiar IMPES (Implicit Pressure Explicit Saturation) scheme in reservoir simulation is an example of an IMEX method of type (3.22), where pressure is implicit and saturations are explicit. The explicit treatment of certain variables reduces computational cost, but introduces stability restrictions. Each stage of an IMEX scheme is a consistent approximation to the full equation. Although IMEX methods do not allow specialized treatment of subprocesses, the main advantage of the methods is that they can be applied to problems with non-separable operators, which is not the case for ADS methods. The flow/transport coupling in the ISC equations is non-separable, and IMEX methods are the only feasible alternative to full coupling.

3.2.2 Applications of operator splitting

Operator splitting techniques are used in a number of applications areas including atmospheric chemistry (Zlatev, 1995), open-air combustion (Westbrook et al., 2005) and mathematical biology (Hundsdorfer and Verwer, 2003). In the context of reactive porous media transport, splitting techniques are extensively used in subsurface contaminant transport problems (see e.g. Arbogast et al., 1996). The chemical components in contaminant transport models are often present in small amounts in an aqueous phase, but undergo a range of chemical processes including oxidation-reduction, dissolution-precipitation, adsorption-desorption, and ion exchange (Walter et al., 1991). The transport equations usually account for advection, dispersion and molecular diffusion, and the chemical reactions are either equilibrium controlled or mixed equilibrium and kinetically controlled (Walter et al., 1991; Yeh and Tripathi, 1991). The chemical processes typically have little or no influence on the flow, and the flow and transport problems are therefore naturally decoupled. The coupled transport and reaction problem is often solved using splitting techniques similar to (3.20) and (3.21). The transport terms are spatially connected, but uncoupled between chemical components. Reaction terms, on the other hand, are spatially disconnected, but coupled through chemical components. A solution methodology based on decoupling the transport and reaction terms therefore results in a transport step, where the (linear) component transport equations are solved individually, and a reaction step, where the chemical equilibrium equations are solved gridblock by gridblock. In the groundwater hydrology literature this approach is referred to as the Sequential Non-Iterative Approach (SNIA) (Walter et al., 1991). To reduce splitting error, a Sequential Iterative Approach (SIA) is often used, where the transport and reaction steps are iterated until convergence (Yeh and Tripathi, 1991).

Operator splitting techniques for contaminant transport models have been implemented in several simulators including HYDROGEOCHEM (Yeh and Tripathi, 1991), THOUGHREACT (Xu et al., 2004) and PARSIM (Arbogast et al., 1996).

3.2.3 A splitting scheme for the ISC equations

Compared to subsurface contaminant transport models, the ISC equations are, in a sense, more tightly coupled. Most importantly, there is a strong feedback on flow from reactions. The heat released in reactions increases oil mobility, and the gases evolved act as a gas drive ahead of the combustion front. Solid deposition from cracking reactions reduces the rock porosity, which therefore affects flow. In general, volume changes due to reactions as well as phase behavior have a strong impact on flow and transport.

We propose a Strang splitting (3.21) for the flow/transport and reaction terms in the ISC equations, where the flow/transport substep is split in half. The flow/transport substep is solved fully implicitly using a similar scheme as described in Section 3.1 for the coupled problem. The reaction substep is solved independently in each gridblock using a subclass of Runge-Kutta methods denoted ESDIRK (Explicit Singly Diagonally Implicit Runge-Kutta), which are tailored for stiff chemical kinetics problems.

In principle, the volume and phase behavior constraint equations are active at all times, i.e. in both the flow/transport and reaction substeps. However, if the volume constraint is enforced in the reaction substep, and the pressure is allowed to increase as gases evolve from reactions, the resulting pressure field after the reaction substep will be non-physical with higher values in gridblocks, where significant reaction took place. Instead we propose a relaxed volume formulation, where the volume constraint is omitted and the pressure is kept constant in the reaction substep. As a result, the phase volumes do not match the pore volume after the reaction step. This volume inconsistency is corrected during the final half-step on flow/transport, such that a consistent solution is obtained at the end of the splitting step. The phase equilibrium constraints are active in both substeps.

Let $\mathbf{f}^t \in \mathbb{R}^{N_b(n_c+2)}$ denote the vector of discrete fluxes, and let $\mathbf{Q}^w \in \mathbb{R}^{N_b(n_c+2)}$ and $\mathbf{Q}^r \in \mathbb{R}^{N_b(n_c+1)}$ denote the vectors of source/sink terms and reaction terms, respectively, as given by

$$\mathbf{f}^t = \begin{bmatrix} \mathbf{f}_1^t \\ \vdots \\ \mathbf{f}_{N_b}^t \end{bmatrix}, \qquad \mathbf{f}_k^t = \begin{bmatrix} f_1^m \\ \vdots \\ f_{n_c}^m \\ f^h \\ 0 \end{bmatrix}_k, \tag{3.24}$$

$$\mathbf{Q}^w = \begin{bmatrix} \mathbf{Q}_1^w \\ \vdots \\ \mathbf{Q}_{N_b}^w \end{bmatrix}, \qquad \mathbf{Q}_k^w = \begin{bmatrix} Q_1^{m,well} \\ \vdots \\ Q_{n_c}^{m,well} \\ Q^{h,well} + Q^{h,htr} \\ V_p - \sum_j V^j \end{bmatrix}_k, \tag{3.25}$$

$$\mathbf{Q}^r = \begin{bmatrix} \mathbf{Q}_1^r \\ \vdots \\ \mathbf{Q}_{N_b}^r \end{bmatrix}, \qquad \mathbf{Q}_k^r = \begin{bmatrix} Q_1^{m,reac} \\ \vdots \\ Q_{n_c}^{m,reac} \\ Q^{h,reac} \end{bmatrix}_k, \tag{3.26}$$

where the residual of the volume constraint is included with the well terms. We define in addition the block diagonal matrix $\mathbf{M} \in \mathbb{R}^{N_b(nc+2)\times N_b(n_c+2)}$

$$\mathbf{M} = \begin{bmatrix} \mathbf{M}_1 & & \\ & \ddots & \\ & & \mathbf{M}_{N_b} \end{bmatrix}, \qquad \mathbf{M}_k = \begin{bmatrix} 1 & & & \\ & \ddots & & \\ & & 1 & \\ & & & 0 \end{bmatrix}_k. \tag{3.27}$$

The discrete fluxes in (3.24) are

$$f_i^m = \frac{1}{V_b}\left[\sum_j \Lambda_{i,k-1/2}^j T_{k-1/2}\Delta^- \Phi_k^j - \Lambda_{i,k+1/2}^j T_{k+1/2}\Delta^+ \Phi_k^j\right], \tag{3.28}$$

$$\begin{aligned} f^h = \frac{1}{V_b}\Bigg[\sum_j \Lambda_{k-1/2}^{j,h} T_{k-1/2}\Delta^- \Phi_k^j - \Lambda_{k+1/2}^{j,h} T_{k+1/2}\Delta^+ \Phi_k^j \\ + \frac{S_{k-1/2}k_{c,k-1/2}}{\Delta x_{k-}}\Delta^- T_k - \frac{S_{k+1/2}k_{c,k+1/2}}{\Delta x_{k+}}\Delta^+ T_k\Bigg]. \end{aligned} \tag{3.29}$$

We note that $f_i^m = 0$ for $i \in \mathcal{I}^s$.

The splitting steps can now be formulated as

1. Solve flow/transport for $t \in \left[t^n, t^{n+1/2}\right]$

$$\mathbf{M}\frac{d\mathbf{u}^{(1)}}{dt} = \mathbf{f}^t\left(\mathbf{u}^{(1)}\right) + \mathbf{Q}^w\left(\mathbf{u}^{(1)}\right), \qquad \mathbf{u}^{(1)}\left(t^n\right) = \mathbf{u}^n. \tag{3.30a}$$

2. Solve reactions for $t \in \left[t^n, t^{n+1}\right]$ and $k = 1, \ldots, N_b$

$$\frac{d\tilde{\mathbf{u}}_k^{(2)}}{dt} = \mathbf{Q}_k^r\left(\tilde{\mathbf{u}}_k^{(2)}\right), \qquad \tilde{\mathbf{u}}_k^{(2)}\left(t^n\right) = \tilde{\mathbf{u}}_k^{(1)}\left(t^{n+1/2}\right), \tag{3.30b}$$

where $\tilde{\mathbf{u}}$ denotes the vector of primary variables, but without pressure, which is assumed constant during the reaction step.

3. Solve flow/transport for $t \in \left[t^{n+1/2}, t^{n+1}\right]$

$$\mathbf{M}\frac{d\mathbf{u}^{(3)}}{dt} = \mathbf{f}^t\left(\mathbf{u}^{(3)}\right) + \mathbf{Q}^w\left(\mathbf{u}^{(3)}\right), \quad \mathbf{u}^{(3)}\left(t^{n+1/2}\right) = \mathbf{u}^{(2)}\left(t^{n+1}\right), \tag{3.30c}$$

which gives $\mathbf{u}^{n+1} = \mathbf{u}^{(3)}\left(t^{n+1}\right)$ as the final approximation.

A nontrivial issue with splitting methods relates to the treatment of boundary conditions. Boundary conditions are imposed on the whole system and conditions for the substeps are missing. In the proposed scheme, the well terms are included with the flow/transport step, but could, in principle, also have been included with the reaction step. The choice made here is based primarily on physical intuition regarding which operators in the equations are influenced the most by the well terms. Clearly, the treatment of boundary conditions requires further analysis, but we shall not pursue it here.

Although the Strang splitting is formally second order accurate, Hundsdorfer and Verwer (2003) note that possible order reductions can occur due to boundary conditions or stiff terms in the equations. Here, we apply Strang splitting primarily due to its symmetry, where the last half-step on flow/transport can be regarded as a corrector-step to correct for the volume inconsistency after the reaction step.

A natural next step in the development of a splitting scheme would be to reduce the implicitness by introducing an IMEX splitting for the flow/transport step, where pressure is solved implicitly, but component concentrations are updated explicitly (i.e. an IMPEC scheme – Implicit Pressure Explicit Composition). In fact, Younis and Gerritsen (2006) have designed a hybrid IMEX-ADS scheme with this feature, but here we limit the discussion to the simpler ADS scheme.

3.3 Efficient reaction integration

In the reaction substep (3.30b), each gridblock is effectively treated as a small chemical reactor or kinetic cell. Paper I in Chapter 5 focusses on this isolated problem and develops a class of ESDIRK integration methods, which are particularly well suited for operator splitting integration of stiff kinetics. An overview of the derivation of the methods is given in Appendix A. Most importantly, as the ESDIRK methods belong to the Runge-Kutta class, they are one-step methods and therefore well suited for short-interval integration as required in an operator splitting framework, where multi-step methods typically perform better on longer intervals. Moreover, ESDIRK methods can be constructed with strong stability properties making them attractive for stiff problems.

We use fractional steps when integrating the reaction substep, where the step length is adjusted automatically during integration based on local error estimates. In this way, the chemical reactions are integrated to meet a user specified tolerance, and localization of the computational effort is achieved, since

multiple fractional steps are only required in gridblocks where significant reaction takes place. As shown in Chapter 4, the fraction of gridblocks requiring more than one integration step on reactions is less than 10% in a 1D simulation. For higher dimensional problems this fraction will be even lower.

3.4 Phase disappearance/reappearance

A second important contribution in Paper I is the development of an algorithm for robust treatment of phase changes. Phase changes are known to cause convergence problems for the integration method. The disappearance or reappearance of a phase introduces non-smooth transitions in the equations. Straightforward integration across these non-smooth points may lead to poor convergence and repeated step failures. Paper I proposes an algorithm for detection and location of phase changes based on discrete event system theory. Experiments show that the algorithm improves the robustness of the integration process near phase boundaries by lowering the number convergence and error test failures compared to direct integration without the new algorithm. We leave the details to Paper I, but present a general overview here.

The phase change detection algorithm was developed and tested for the isolated, single-cell reaction subproblem (i.e. the VKC), and it has not yet been extended to the 1D problem. In the VKC, the primary mass and energy balance equations and the secondary phase equilibrium constraints are solved simultaneously. To detect and locate phase changes we consider the VKC as a discrete event problem. The appearance or disappearance of a fluid phase marks the occurrence of a *discrete event*, e.g. a change from a single phase region to a two-phase region, or vice versa. The time of the phase change cannot be determined a priori, and a change generally occurs between mesh points. The detection of a phase change and subsequent location of the exact time of change are the main components of the discrete event algorithm.

The detection part of the algorithm is based on monitoring sign changes in special event functions. A sign change marks the occurrence of an event. Within each integration step the system is locked in its current state. The event functions are evaluated at the end of each step, and if any sign changes have occurred, the exact time of occurrence is located. The approach is based on the assumption that the system of equations is mathematically well behaved in a small neighborhood of the phase changes.

Paper I focusses on the ideal mixture case with K-value correlation based phase behavior. The algorithm was extended to EoS based phase behavior in Kristensen et al. (2007*a*), and we summarize the results here. For phase changes involving the oil and gas phases, disappearance of a phase is detected by monitoring phase fractions. In two-phase oil-gas regions the molar phase fractions can be evaluated explicitly from the primary and secondary variables. The gas phase fraction defines the event functions for switches to single phase oil or gas. We

exploit the existence of the negative flash (Whitson and Michelsen, 1989) in an extended region around the phase envelope. In the negative flash the equilibrium conditions (2.15) are satisfied with physically meaningful phase compositions, but with $\beta^g > 1$ (single phase gas) or $\beta^g < 0$ (single phase oil). Converging the negative flash to a solution with $\beta^g > 1$ or $\beta^g < 0$ indicates that the mixture is stable as single phase to the same certainty provided by a traditional stability test (Whitson and Michelsen, 1989). Thus, we rely on monitoring the phase fraction to detect changes into single phase regions. The most important property of the negative flash is that the phase properties vary smoothly across phase boundaries, and therefore that the reaction kinetic expressions have continuous derivatives at phase boundaries.

Detecting a change from single phase gas or oil to a two-phase oil-gas region is more involved for the EoS based approach than for the ideal K-value based approach. A given mixture is stable as a single phase if, and only if, the total Gibbs energy is at its global minimum. Detecting phase instability requires a stability analysis, which in principle involves a global search in composition space (Michelsen, 1982). Therefore, no event function exists that can be evaluated explicitly to determine a change to a two-phase region. Instead, the event function is defined implicitly as the outcome of a stability analysis, which considerably increases the complexity of the problem.

We use the Gibbs tangent plane condition to verify stability (Michelsen, 1982). The tangent plane distance function is defined as

$$tpd(\mathbf{x}^{trial}) = \sum_i x_i^{trial} \left(\left[\ln x_i^{trial} + \ln \varphi_i(\mathbf{x}^{trial}) \right] - \left[\ln z_i + \ln \varphi_i(\mathbf{z}) \right] \right), \quad (3.31)$$

where $\mathbf{z}$ is the overall mixture composition. A necessary and sufficient condition for phase stability is that (3.31) is non-negative for any trial phase compositions, $\mathbf{x}^{trial}$. The function is non-negative everywhere if it is non-negative at its minima. In practice it is intractable to search the entire composition space, so we perform a one-sided stability analysis (Michelsen, 1982) by looking for the "missing phase". For example, if we are in a single phase oil region, we search for a gas phase by minimizing (3.31) using a gas-like initial estimate for $\mathbf{x}^{trial}$. The event function associated with changes into two-phase regions is defined in terms of the minimum of the *tpd* function

$$tpd_{min}\left(T, P, \mathbf{z}\right) \equiv \min_{\mathbf{x}^{trial}} tpd\left(\mathbf{z}, T, P, \mathbf{x}^{trial}\right). \quad (3.32)$$

When approaching the phase boundary from the single phase region, the *tpd* function has a positive non-trivial minimum. When $tpd_{min} < 0$, the mixture is unstable and will split into two phases, which then defines our event function. The situation is illustrated in Figure 3.2. The first plot shows the Gibbs energy of mixing for a binary mixture. At three overall compositions near the phase change we draw the tangents to the Gibbs energy curve and construct the tangent plane distance curves (bottom figure). When approaching the phase

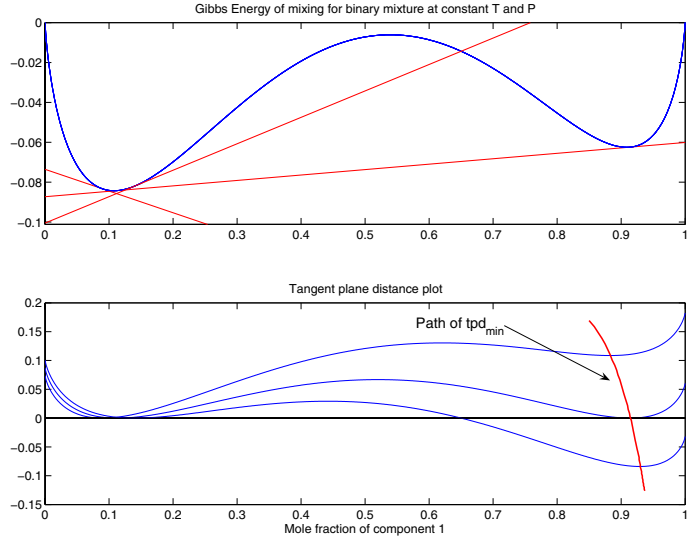

Figure 3.2: Gibbs energy of mixing and tangent plane distance plot for a binary mixture. Tangents are drawn at three different overall compositions corresponding to a stable, equilibrium and unstable mixture. The path of tpd_{min} when approaching and crossing the phase boundary is indicated in the bottom figure.

boundary, the non-trivial minimum of the *tpd* function approaches zero, and the path of tpd_{min} then defines our event function.

Event functions are evaluated at the end of each integration step. Event functions associated with changes into a two-phase region, which require minimization of the tangent plane distance function, are computationally more demanding than the other event functions, which can all be evaluated explicitly. In the current work we have emphasized robustness of the algorithm. A possible efficiency improvement could be realized by exploiting shadow regions as in Rasmussen et al. (2006), which will reduce the number of stability analyses required.

3.5 Comments on simulator implementation

In this section we discuss briefly important implementational details for both the fully coupled and operator splitting schemes. Implementation of the ESDIRK schemes is discussed in Paper I. The simulator was developed using the Fortran 90/95 language and the Compaq Visual Fortran compiler. In the implementation we have emphasized a clear and logical code structure with flexibility to

add new features, and to a lesser extent computational aspects such as optimal memory usage and time efficiency.

The sequence of tasks carried out by the simulator can be summarized in the following pseudo-code:

```
Read user input
Perform preprocessing operations
Initialize gridblocks in equilibrium
while time less than final time do
  Compute global timestep
  if FIM scheme then
    Advance one FIM step...
    while residual larger than tolerance do
      Flash all gridblocks
      Compute properties
      Evaluate residual and Jacobian of (3.13)
      Solve linear system and perform update (3.16)
    end while
  else
    Advance one SPLIT step...
    Perform half step on flow/transport (3.30a)
    Perform full step on reactions (3.30b)
    Perform half step on flow/transport (3.30c)
  end if
  if step converged then
    Update time and solution
  else
    Reset solution and reduce time step
  end if
end while
```

We make the following comments:

- The simulator reads inputs from files. These include
  - Static grid properties: block size, void porosity, and permeability.
  - Component and phase properties: critical parameters, binary interaction coefficients, liquid reference densities, heat capacity correlation constants, viscosity correlation constants, and thermal conductivities.
  - Reaction kinetic data: reaction stoichiometry, activation energies, pre-exponential factors, and reaction enthalpies.
  - Initial conditions: temperature, pressure, and overall composition.
  - Well data: injection rates, temperature, and composition. Production well bottom-hole pressure.

  - Heat controller specifications: heater size, set point, gain, and timing (on/off switches).
  - Numerical specifications: time integration scheme (fully coupled or splitting) and convergence tolerances.

- The preprocessing operations include calculation of grid transmissibilities, well indices and initialization of the gridblocks from initial conditions. The gridblocks are initialized in thermodynamic equilibrium. Initialization for simultaneous gravity and thermodynamic equilibrium has not been implemented.

- Timesteps in the fully coupled scheme and global timesteps in the splitting scheme are calculated from the timestep formula (Aziz and Settari, 1979)

$$\Delta t^{n+1} = \Delta t^n \min_{i,k} \left[\frac{(1+\lambda)\,\Delta u_{ik}^n}{\Delta u_i^* + \lambda \Delta u_{ik}^n} \right], \tag{3.33}$$

  where Δu_{ik}^n is the change in variable i in gridblock k over the previous time step, Δu_i^* is the target change, and λ is a tuning factor.

- The termination criterion for the Newton-Raphson iterations is based on the max-norm of the normalized residual

$$e_{res}^{(l)} = \|\tilde{\mathbf{R}}^{(l)}\|_\infty, \tag{3.34}$$

  where the components of the normalized residual are

$$\begin{aligned} \tilde{R}_{ik}^{(l)} &= \left(\frac{R_{ik}}{C_{ik}} \right)^{(l)}, \qquad i = 1, \ldots, n_c, \\ \tilde{R}_{ik}^{(l)} &= \left(\frac{R_{ik}}{U_k} \right)^{(l)}, \qquad i = n_c + 1, \\ \tilde{R}_{ik}^{(l)} &= \left(\frac{R_{ik}}{\phi_v V_b} \right)^{(l)}, \qquad i = n_c + 2, \end{aligned} \tag{3.35}$$

  i.e. on a gridblock basis the component balances are normalized by the total component amounts, the energy balance is normalized by the total internal energy, and the residual of the volume constraint is normalized by the pore volume.

- Although only 1D problems are considered here, the simulator is designed in such a way that a different gridding module can easily be included. In the computation of interblock flux terms, the simulator kernel only sees a list of gridblock connections with associated transmissibilities, and no assumptions are made regarding grid geometry at this level.

- The derivatives required in the Jacobian of the fully coupled, implicit system, as well as the Jacobian of the implicit flow/transport substep in the splitting scheme, are approximated by numerical differences. This approach is flexible when adding new features or changing property models, but computationally more expensive than analytical derivatives. The perturbations in the numerical derivatives are chosen according to

$$\delta u_{ik} = \sqrt{\epsilon_m \max\left(10^{-5}, |u_{ik}|\right)}, \tag{3.36}$$

  where ϵ_m denotes the machine precision. The grid structure is exploited in the computation of Jacobians, so that several variables are perturbed simultaneously. The overall computational cost scales linearly with the number of gridblocks. We note that STARS also uses a numerical approximation to the Jacobian (CMG, 2004).

- Exact flashes are performed in each Newton-Raphson iteration using information from the previous iteration as starting guess. Stability analysis is performed in single phase gridblocks to determine if the current state is stable.

- Two linear solvers are included for solution of the linear equation systems arising in each Newton-Raphson iteration:

  - MA48: a direct solver based on sparse Gaussian elimination (Duff and Reid, 1996).
  - GMRES: an ILU preconditioned GMRES solver from the SPARSKIT library (Saad, 1994).

Chapter 4

Simulation examples

To illustrate the behavior of ISC in combustion tube experiments, and as a supplement to the results presented in the research papers, we consider in this chapter a number of simulation examples. We study the influence of boundary and initial conditions and conclude with an example illustrating the splitting scheme proposed in the previous chapter.

Influence of boundary and initial conditions

As a first example we consider simulation of a dry combustion tube experiment. The reaction and component model is introduced in Paper I and detailed data is given in Section B.1. The model has six components: two oil pseudo components, oxygen, solid coke, water, and inert gas. The reactions include direct oxidation of the oil components, cracking of the oil into solid coke, and oxidation of the coke component. The oil has an API gravity of 25.

Air is injected at a rate of $16\,\mathrm{L/hr}$ (surface conditions) into an oil saturated core, which is preheated to 311 K and pressurized to 137 atm. The injection end is heated for the first half hour of the simulation by a constant rate energy input. For the remainder of the simulation the combustion tube is operated adiabatically. Figure 4.1 shows the temperature, oil saturation, water saturation, and solid coke concentration profiles at four different times during the simulation. As air is injected and the tube heated, a combustion front is established, which propagates slowly into the core and displaces the oil. No initial water is present, but a small amount of water is formed in reactions, which moves ahead of the combustion front.

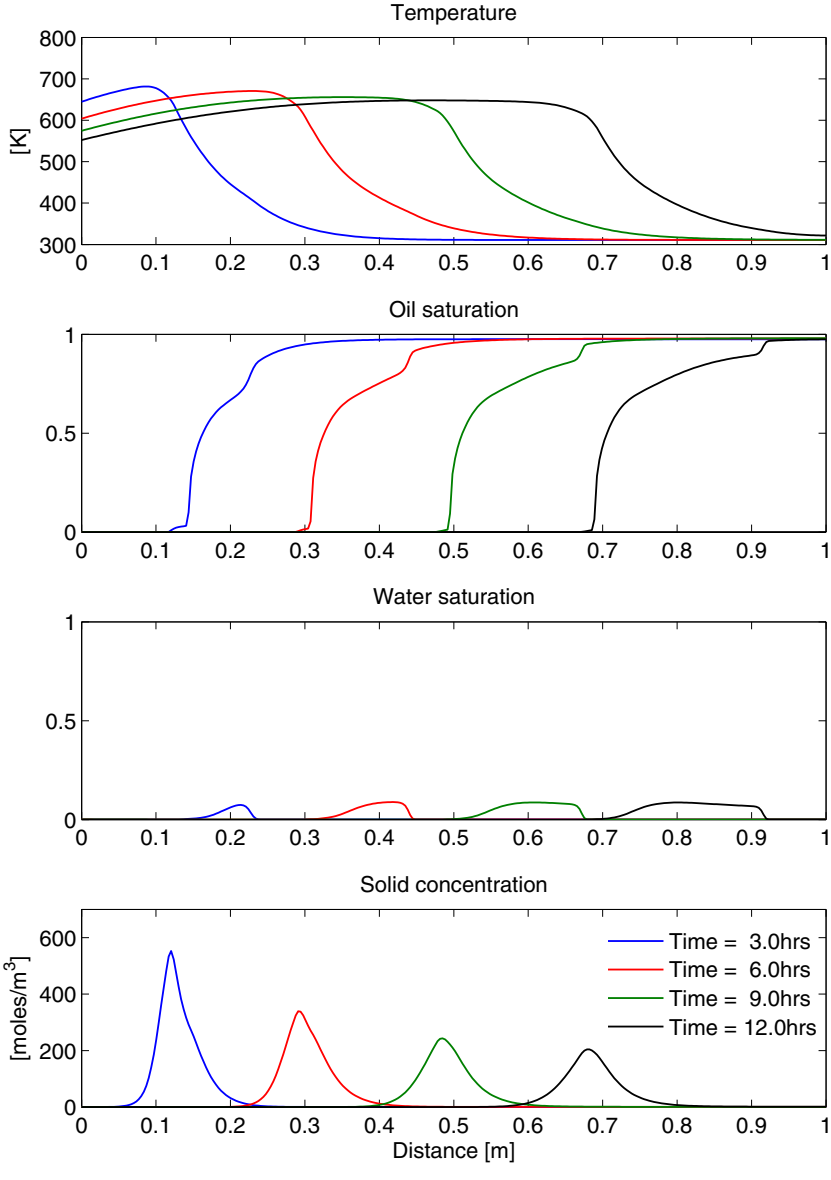

Figure 4.1: Dry combustion simulation results for the minimal reaction model. Temperature, saturation, and solid coke concentration profiles are shown at four different times during the simulation.

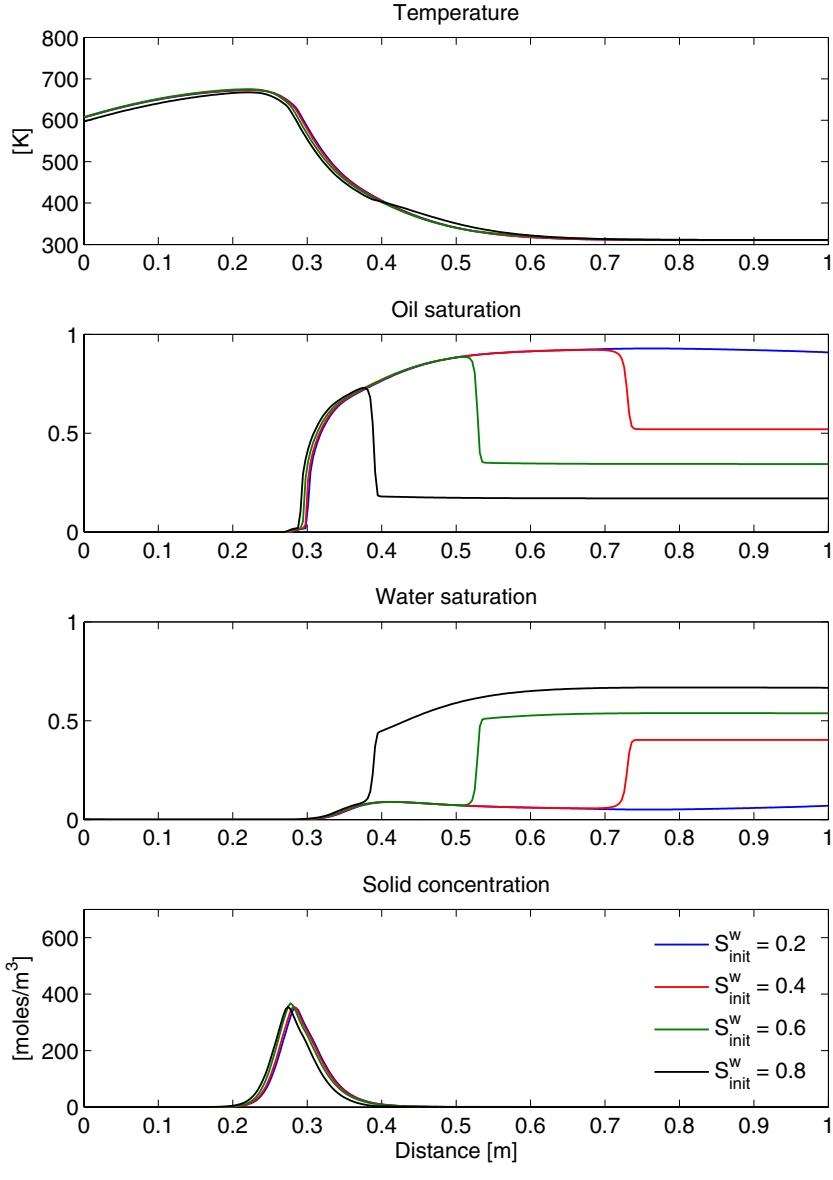

Figure 4.2: Dry combustion simulation results with varying initial water saturation. Temperature, saturation, and solid coke concentration profiles are shown at $t = 6$ hrs and four different initial water saturations.

In the next example we consider a similar setup as above, but we study the influence of the initial water saturation. Figure 4.2 shows temperature, saturation, and coke concentration profiles at $t = 6$ hrs for four different initial water saturations. Figure 4.3 shows the corresponding production curves in terms of the total cumulative hydrocarbon recovery and the fraction of hydrocarbons burned in reactions. As observed from Figure 4.2, the initial water saturation does not influence the amount of coke lay-down and thereby the front propagation speed. In all cases a combustion front is established. An oil bank is formed downstream of the combustion front, and further downstream the water is displaced by the oil bank. Since the same amount of coke is formed, the relative amount of hydrocarbons burned in reactions increases with decreasing initial oil saturation, and the ultimate recovery is therefore lower with low initial oil saturation.

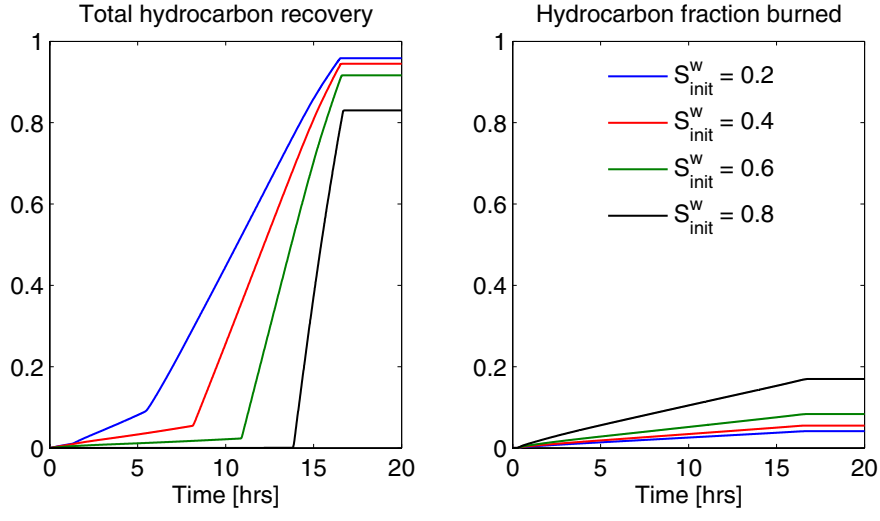

Figure 4.3: Production curves for dry combustion simulation with varying initial water saturation. The total cumulative hydrocarbon recovery is shown along with the fraction of hydrocarbons consumed in reactions.

With no initial water present we consider in Figure 4.4 and 4.5 a variation in the oxygen feed concentration. The injection is fixed at $16\,^{\mathrm{L}}/_{\mathrm{hr}}$, and the oxygen mole fraction in the feed is varied from 0.1 to 0.7. The feed concentration has direct influence on the front propagation speed as seen from Figure 4.4. An oxygen mole fraction of 0.1 is too low to sustain combustion. The initial amount of coke formed, when heating the injection end of the combustion tube, is never consumed. For higher feed concentrations a combustion front is established. This example clearly illustrates the inefficiency of the process when proper ignition conditions are not reached.

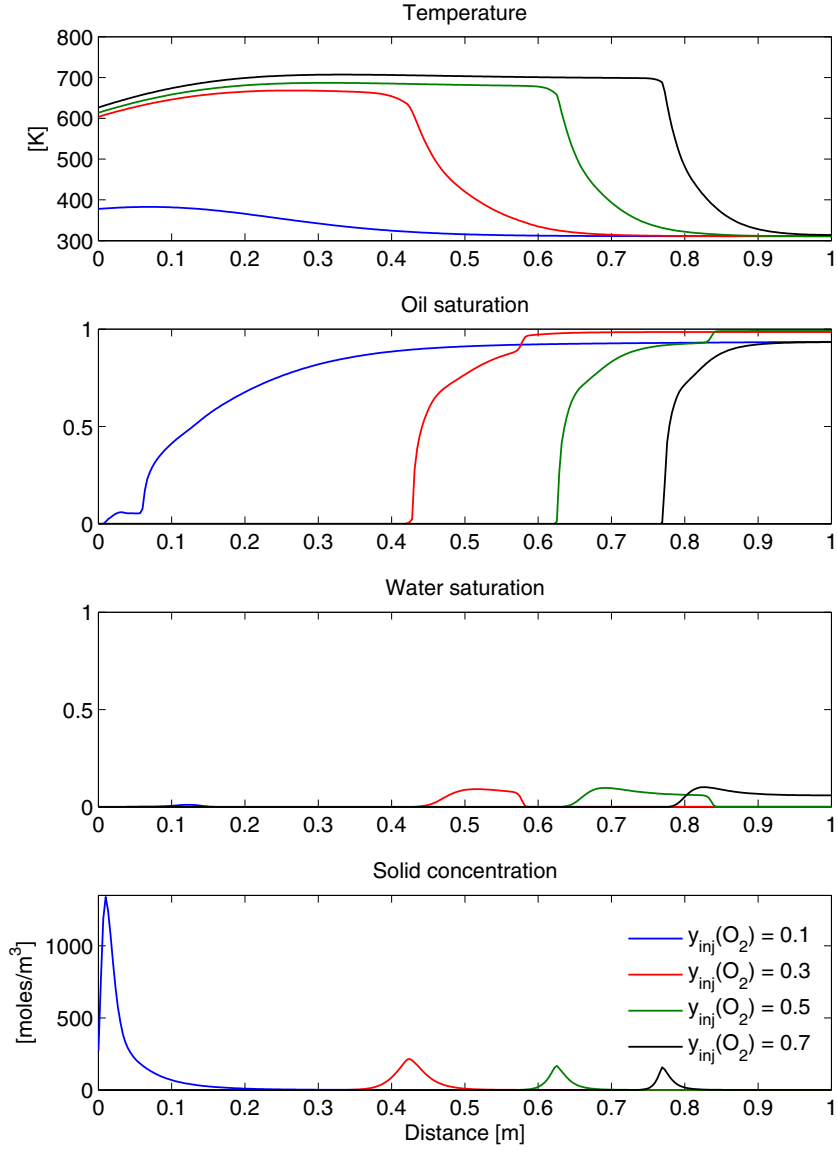

Figure 4.4: Dry combustion simulation results with varying oxygen feed concentration. Temperature, saturation, and solid coke concentration profiles are shown at $t = 6$ hrs and four different oxygen feed concentrations.

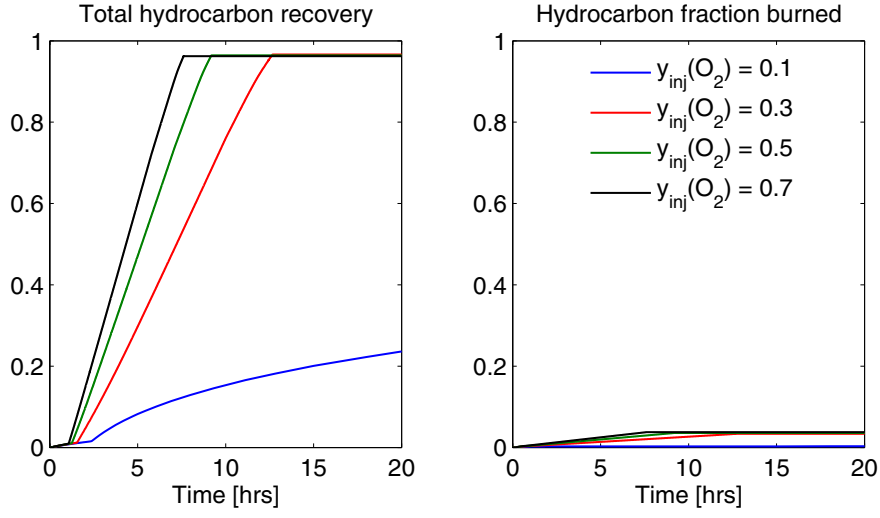

Figure 4.5: Production curves for dry combustion simulation with varying oxygen feed concentration. The total cumulative hydrocarbon recovery is shown along with the fraction of hydrocarbons consumed in reactions.

A large part of the energy generated in dry combustion processes remains behind the combustion front as heat absorbed in the reservoir rock. Because of the low heat capacity of air, the heat in the burned zone is not transported efficiently by the injected air, as observed in e.g. Figure 4.4. To overcome this inefficiency water is sometimes injected simultaneously with air, the risk being that the water will quench the combustion and lead to extinction. Figure 4.6 and 4.7 show results from wet combustion simulations with varying amounts of water. By injecting water, the energy behind the combustion front is swept forward more efficiently than for dry air injection, and the combustion front is propagated faster. However, at a water rate of 0.05 $^{\text{pvi}}/_{\text{hr}}$ the process is effectively quenched. We note also that coke is left behind the combustion front due to the rapid decrease in formation temperature caused by water injection.

A heavy oil example

The second reaction and component model considered in this thesis is based on a characterization of the oil in terms of its SARA (Saturates, Aromatics, Resins and Asphaltenes) fractions. The model has 14 components and 14 reactions. The oil has an API gravity of 16. Complete input data for the simulation is given in Section B.2.

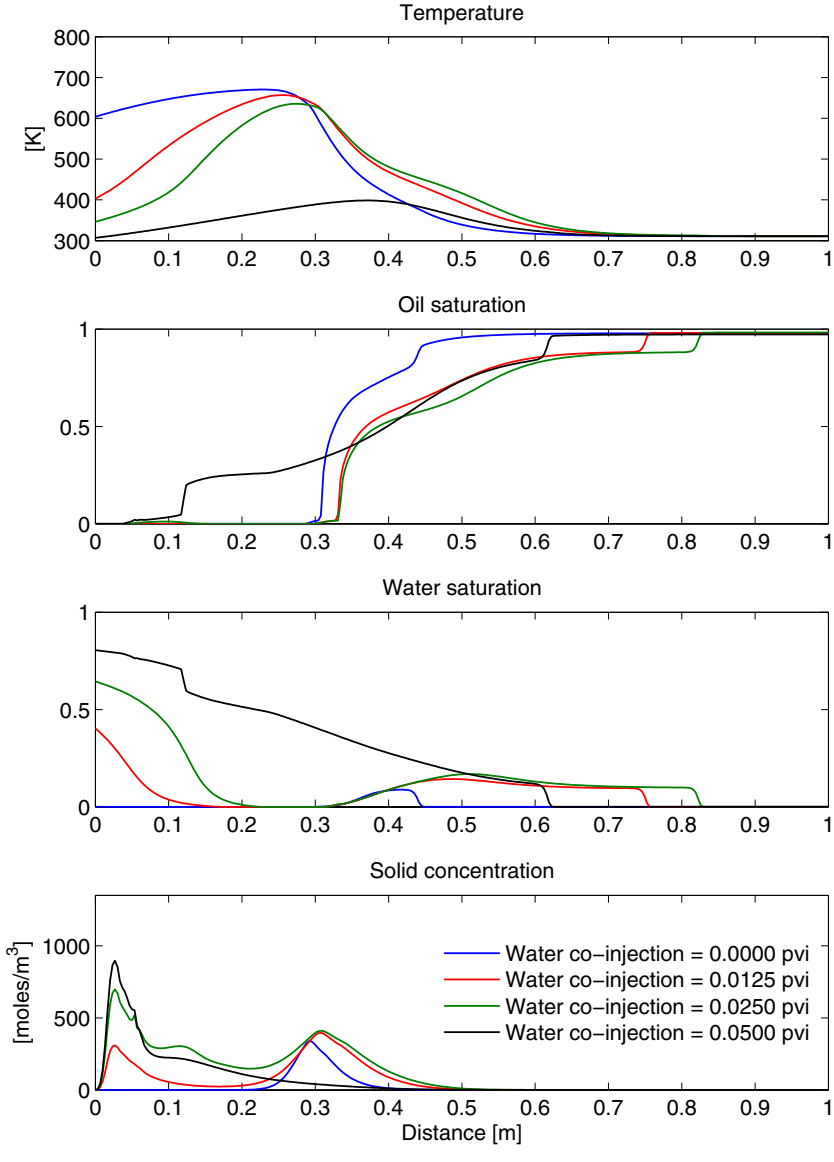

Figure 4.6: Wet combustion simulation results with varying water co-injection rate. Temperature, saturation, and solid coke concentration profiles are shown at $t = 6$ hrs and four different water rates. The rates are given in pore volumes injected per hour.

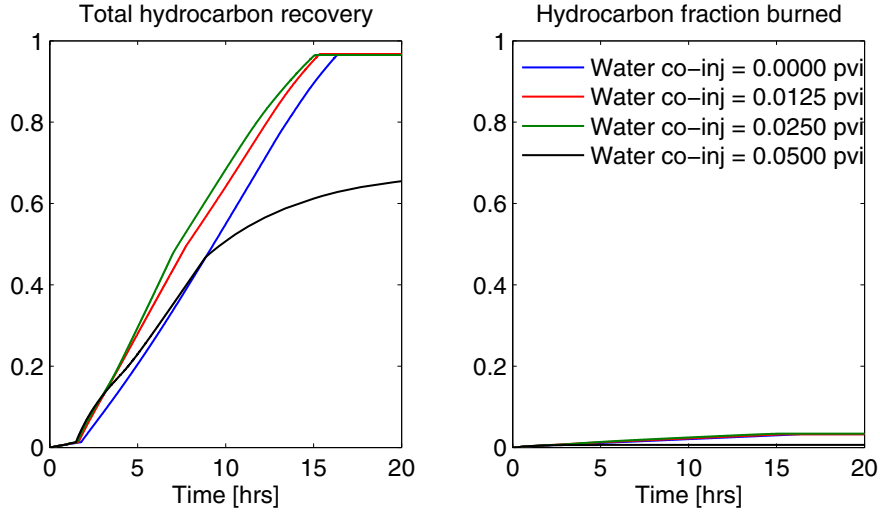

Figure 4.7: Production curves for wet combustion simulation with varying water co-injection rates. The total cumulative hydrocarbon recovery is shown along with the fraction of hydrocarbons consumed in reactions.

We consider a simple dry combustion simulation. Air is injected at a rate of $45\,{}^{\mathrm{L}}/_{\mathrm{hr}}$ (surface conditions) into an oil/water saturated core. The initial core temperature and pressure are 323 K and 14.5 atm, respectively, and the initial water saturation is 0.25. Again, to initiate combustion, the injection end of the combustion tube is heated externally for the first half hour of the simulation. For the remainder of the simulation a proportional heat loss along the core is accounted for according to Eqn. (2.20) with a heat controller gain of $4\,{}^{\mathrm{kJ}}/_{\mathrm{m}^2\cdot\mathrm{K}\cdot\mathrm{hr}}$ and controller set point of 323 K.

Figure 4.8 shows the temperature, oil saturation, water saturation, and pressure profiles at four different times during the simulation. As the combustion front propagates into the core, the oil is banked ahead of the front creating an almost fully oil saturated zone. The temperature in this zone is still at the initial level, and the mobility is therefore very low, which causes the pressure to increase behind the front. This phenomenon has been observed in practical laboratory combustion tube tests for heavy oils (Moore et al., 1995). In laboratory tests, as well as in the field, equipment capabilities will limit the injection pressure, and formation of a low-mobility oil bank, as observed in Figure 4.8, will effectively plug the system and stall the combustion front. The break-down in oxygen supply to the front shifts the reactions to the low-temperature regime with partial oxidation reactions, which is generally an unfavorable operating regime. Plugging of the system is a common cause of failure in laboratory combustion tests (Moore et al., 1995).

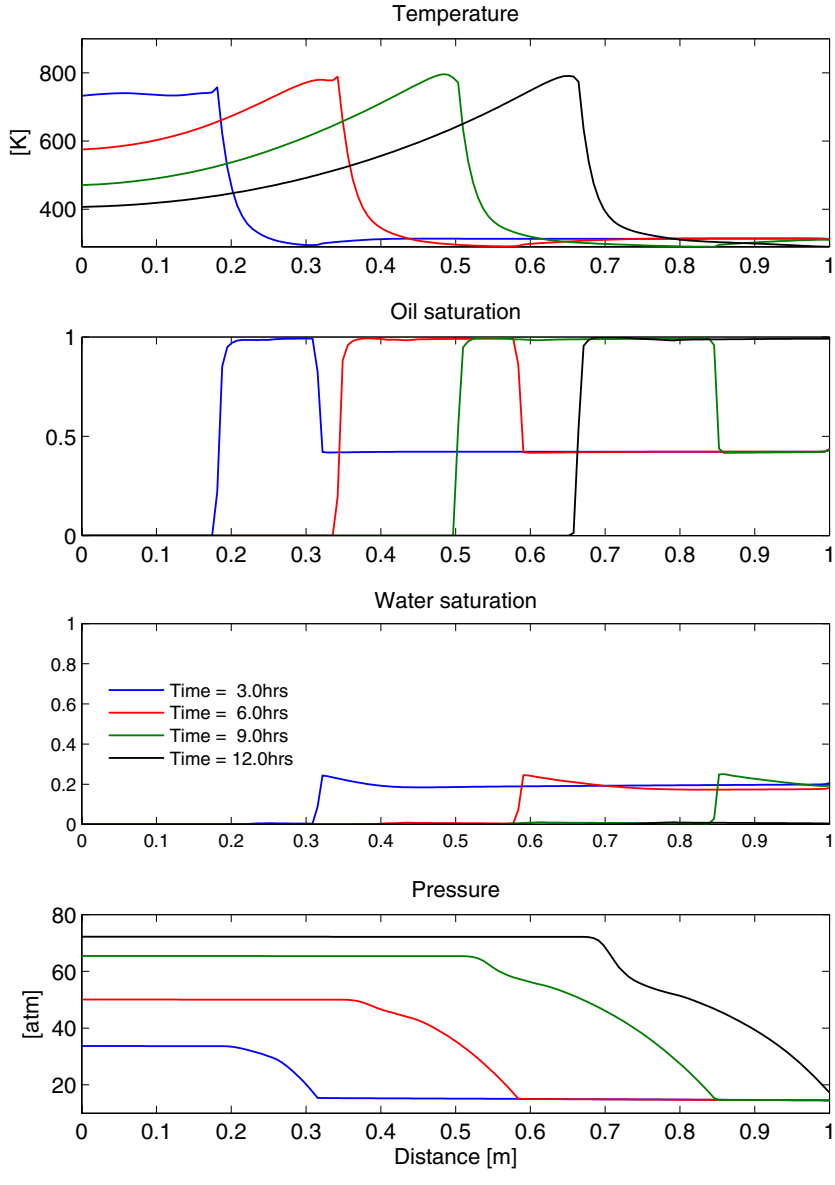

Figure 4.8: Dry combustion simulation results for the SARA based reaction model. Temperature, saturation, and pressure profiles are shown at four different times during the simulation.

Local adaptivity from splitting integration

As a final example we consider integration using the proposed splitting scheme. For a fixed grid with 100 cells we simulate a dry combustion experiment using the minimal reaction model. We compare solutions obtained from the fully coupled scheme (FIM) and the splitting scheme.

During the onset of combustion we use the FIM scheme with timesteps calculated from Eqn. (3.33). To allow comparison we then continue with a fixed (global) timestep of $\Delta t = 0.05$ hrs when a stable combustion front is established. Thus, the time step used in the FIM scheme, from this point onwards, corresponds to the global timestep in the splitting scheme. The reaction substep is integrated using ESDIRK34 (see Paper I or Appendix A) with absolute and relative error tolerances set to 10^{-4} and 10^{-3}, respectively. The solutions from the FIM and splitting schemes are compared to a solution obtained on the same grid with the FIM scheme, but with timesteps of $\Delta t = 0.001$ hrs.

Figure 4.9 shows temperature, oil saturation, and coke concentration profiles for the FIM scheme, the splitting scheme, and the reference solution. The bottom plot in Figure 4.9 shows the number of fractional reaction steps required in the splitting scheme in each cell to meet the integration tolerances. We see that the ESDIRK solver adapts to the reaction dynamics in each cell. Only 5–10% of the cells near the combustion front require more than one integration step. The computational effort is thereby localized, which is one of the main advantages of a splitting based method.

We have verified that the reference solution in Figure 4.9 (solid line) is temporally converged. By comparing the solution profiles we observe that the splitting based solution is slightly more accurate than the FIM solution. The splitting scheme uses two fully implicit half-steps on flow/transport and is, hence, more expensive than the FIM scheme, although fewer nonlinear iterations are required in each half-step compared to a full step in the FIM scheme. The results presented here for the splitting scheme are preliminary. More work is needed to properly validate the splitting implementation and compare the accuracy and performance of the scheme to the FIM approach.

We make the following general observations:

- The splitting scheme is more accurate, but computationally more expensive on a per time step basis than the FIM scheme.
- The maximum global splitting step is limited by convergence in the flow/transport substeps. It is comparable in length to the maximum FIM step.
- The flow/transport substeps dominate the computing time. Approximately 10% of the time is spent on reaction integration.

We note that no effort has been made to optimize the splitting scheme with respect to choice of order of the ESDIRK method and error tolerances for the reaction integration.

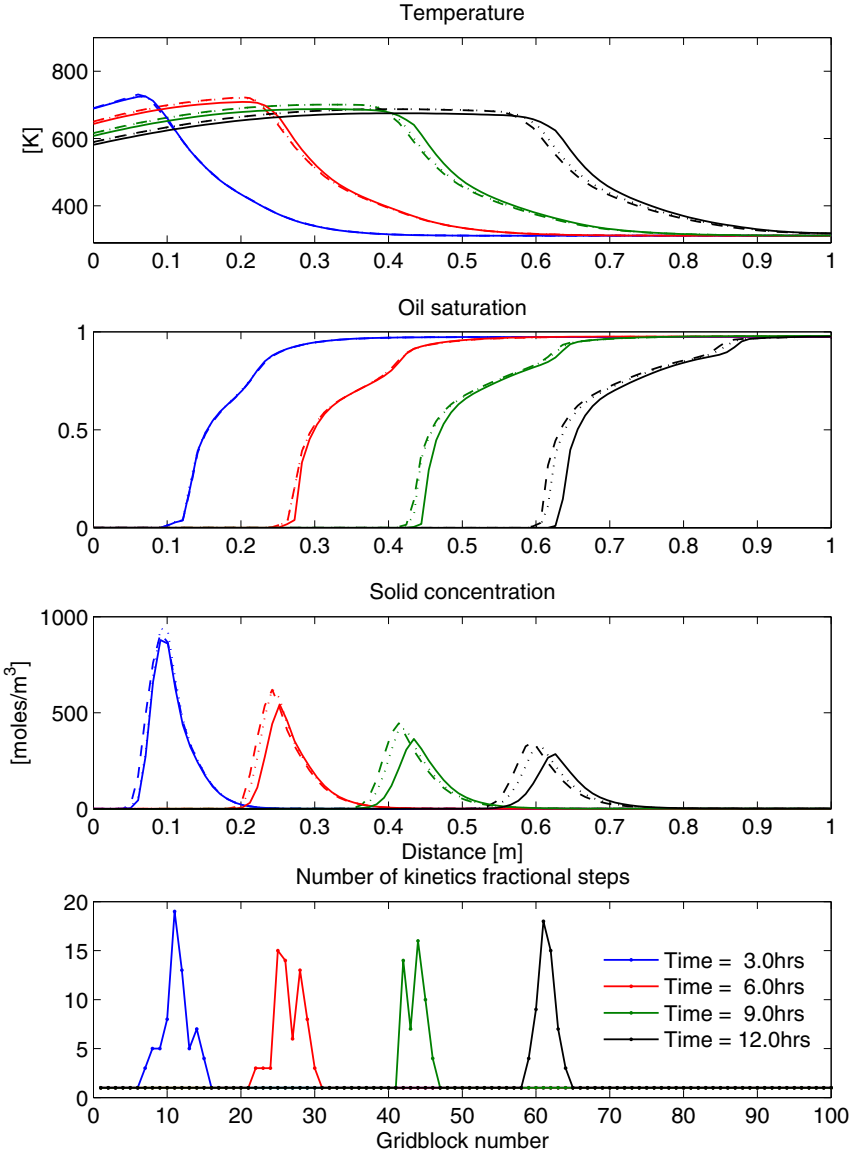

Figure 4.9: Temperature, oil saturation, and solid coke concentration profiles. Comparison is made between the FIM scheme (dashed line), the Strang splitting scheme (dotted line), and a temporally converged FIM solution (solid line). The bottom plot shows the number of fractional steps on kinetics for each cell in the grid.

Paper I

Morten R. Kristensen, Margot G. Gerritsen, Per G. Thomsen,
Michael L. Michelsen and Erling H. Stenby:

Efficient Integration of Stiff Kinetics with Phase Change Detection for Reactive Reservoir Processes

Published in *Transport in Porous Media*, **69**(3):383–409, 2007.

Chapter 5

Integration of stiff kinetics for reactive reservoir processes

Abstract:
We propose the use of implicit one-step ESDIRK (Explicit Singly Diagonal Implicit Runge-Kutta) methods for integration of the stiff kinetics in reactive, compositional and thermal processes that are solved using operator-splitting type approaches. To facilitate the algorithmic development we construct a virtual kinetic cell model. The model serves both as a tool for the development and testing of tailored solvers as well as a testbed for studying the interactions between chemical kinetics and phase behavior. As case study, two chemical kinetics models with 6 and 14 components, respectively, are implemented for in-situ combustion, a thermal oil recovery process. Through benchmark studies using the 14 component reaction model the new ESDIRK solvers are shown to improve computational speed when compared to the widely used multi-step BDF methods DASSL and LSODE.

Phase changes are known to cause convergence problems for the integration method. We propose an algorithm for detection and location of phase changes based on discrete event system theory. Experiments show that the algorithm improves the robustness of the integration process near phase boundaries by lowering the number convergence and error test failures by more than 50% compared to direct integration without the new algorithm.

Keywords: Reactive transport processes, stiff ODE solvers, differential-algebraic equations, ESDIRK methods, discrete event systems, phase change detection, multi-scale methods, operator splitting, enhanced oil recovery, in-situ combustion

5.1 Introduction

In this paper we discuss the development of efficient algorithms for the integration of stiff chemical reactions in reactive multi-phase, multi-component processes in porous media. We illustrate the solvers we developed using In-Situ Combustion (ISC) applications that are receiving strong renewed interest in the petroleum industry, but the solvers are applicable to general reactive porous media processes. The processes under consideration generally have a strong multiscale character. Physical subprocesses, such as mass and heat transport, have associated temporal, and often also spatial, scales that are typically much larger than those for kinetics. Operator splitting methods, such as those developed in Younis and Gerritsen (2006), are attractive for solving processes with disparate temporal scales. They allow subprocesses to be essentially decoupled so that each subprocess can be solved using tailored numerical methods and time steps. For example, stiff kinetics is best treated by implicit methods and requires relatively small time steps, whereas convective transport can often be integrated explicitly with much larger time steps. In this work, we assume that the compositional and thermal problem of interest is solved using an operator splitting method. In a reaction substep, each grid block is then effectively treated as a small kinetic cell with homogeneous pressure and temperature and well mixed fluids. We focus on the design of efficient numerical integration of the stiff kinetics. High computational efficiency is very desirable as a typical simulation may involve millions of reaction substeps.

Phase behavior, that is the transfer of components between phases, adds further complexity to compositional and thermal processes. For non-reacting systems, it is reasonable to assume that the time scales for component transfer between phases to reach an equilibrium state are faster than for other subprocesses. The validity of the assumption for reactive systems is unclear, but in lack of better alternatives we shall assume thermodynamic equilibrium conditions. How to numerically treat the interaction of phase behavior with kinetics is, as yet, not fully understood in processes such as in-situ combustion. We expect that predictions are very sensitive to the approach chosen, because phase behavior and kinetics both affect the amount and composition of the combustion fuel, the heat released and the combustion gases produced.

The main contributions of this work are threefold:

- We develop a kinetic cell model, which we refer to as the Virtual Kinetic Cell (VKC), that facilitates the construction of efficient, tailored integration methods for stiff kinetics, and also enables isolated sensitivity studies of the kinetics / phase behavior interaction.

- We investigate efficient numerical integrators for fast kinetics based on specialized Runge-Kutta methods.

- We propose an algorithm for robust detection and location of phase changes

based on discrete event system theory.

The paper is organized as follows. Section 5.2 provides a review of physical models for in-situ combustion reactions and serves to motivate the development of the VKC. Two VKC models based on in-situ combustion kinetics are presented in this section also. The VKC model equations are presented in Section 5.3. Section 5.4 discusses specialized Runge-Kutta methods and the development of an algorithm for robust detection and location of phase changes. Finally, Section 5.5 presents the results from performance comparisons between the new solver and state-of-the-art stiff ODE solvers.

5.2 In-situ combustion reaction models

5.2.1 The in-situ combustion process

ISC, also known as high pressure air injection or fire-flooding, is receiving strong renewed interest because the easy to produce oil reserves are declining. This thermal process can be effective in improving recovery of existing reservoirs as well as unlocking the vast reserves of heavy oil in the US and elsewhere in an environmentally sound manner (Prats, 1986; Castanier and Brigham, 2004). ISC is the process of injecting air into an oil reservoir to oxidize a small fraction of the hydrocarbons present. A schematic is shown in Figure 5.1.

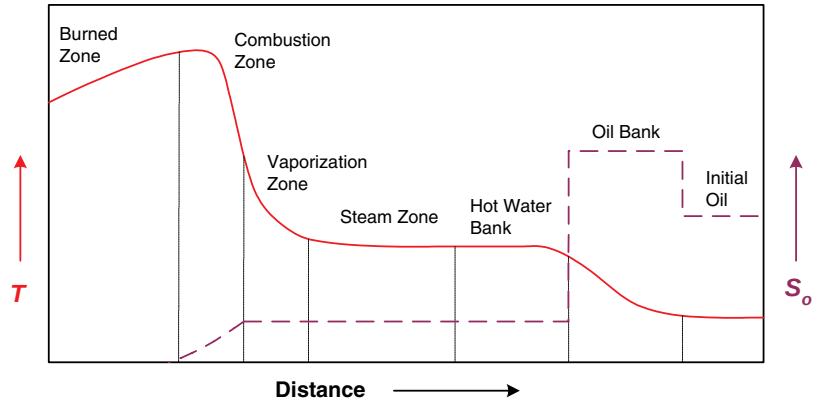

Figure 5.1: Schematic representation of characteristic temperature and saturation distributions in forward in-situ combustion (adapted from Prats (1986), not to scale).

The slow moving combustion front is propagated by a continuous flow of air. Figure 5.1 gives a schematic representation of characteristic temperature and saturation zones in ISC (Prats, 1986). Starting from the injection well the burned zone is the volume already swept by the combustion zone. In the

combustion zone injected oxygen reacts with residual hydrocarbons generating carbon oxides and water, and producing heat. Hydrocarbons contacted by the leading edge of the high temperature zone undergo thermal cracking and vaporization. Mobilized light components are transported downstream where they mix with the original crude. The heavy residue, which is normally referred to as coke, is deposited on the core matrix and is the main fuel source for the combustion. Downstream of the vaporization zone is the steam plateau which is formed from water of combustion and vaporization of formation water. Further downstream the steam condenses when the temperature drops below the steam saturation temperature, and a hot water bank is formed . The leading edge of this bank is the primary area of oil mobilization where the oil is banked by the hot water.

Thermal conduction allows heat to sweep areas of the reservoir not directly contacted by hot fluid. For heavy oils, the recovery efficiency is substantially improved because of the dramatic reduction of the viscosity of heavy oils with temperature. But, ISC is applicable to lighter oils as well because it also promotes production through flue-gas drive, thermal expansion, steam and water drive, and vaporization of lighter oils (Gillham et al., 1997; Clara et al., 2000). ISC can recover oil economically from a variety of reservoir settings.

Existing ISC models include convective mass transfer, convective and conductive heat transfer, kinetically controlled chemical reactions, and fluid phases in thermodynamic equilibrium (Crookston et al., 1979; Grabowski et al., 1979; Coats, 1980). In Younis and Gerritsen (2006), an operator splitting method was proposed for ISC simulations which combines the traditional IMPEC (IMplicit Pressure Explicit Composition) approach with an explicit temperature treatment based on a symmetric additive splitting method for the convection and reaction operators.

5.2.2 Chemical reactions

A typical crude oil is a complex mixture of hundreds of different chemical species. In various applications, such as combustion engines, increasingly large reaction models are being used with often hundreds of elementary reactions, in order to adequately compute not only the energy released by the reactions, but also the end products formed. Of particular interest in combustion engines, for example, is the formation of pollutants such as nitrous oxides. In reactive processes in porous media, such as ISC, the chemical reactions are generally lumped together in a limited set of empirically derived equations.

Today it is generally accepted that three classes of reactions dominate in ISC processes: (1) low temperature oxidation reactions (LTO), (2) medium temperature reactions and (3) high temperature oxidation reactions (HTO) (Castanier and Brigham, 2004). The temperature ranges associated with each group of reactions are roughly 150 to 300°C for LTO, 300 to 450°C for medium temperature reactions and above 450°C for HTO. The nature of the reactions in each

regime depends on the type of oil. For heavy oils the LTO reactions are oxygen addition reactions producing partially oxygenated compounds, such as alcohols, ketones, and aldehydes, and only few carbon oxides. Lighter oils undergo full H/C bond breaking combustion reactions in the LTO regime but may undergo oxygen addition reactions at lower temperatures. At intermediate temperatures a series of cracking or pyrolysis reactions take place that form coke, the fuel for the HTO reactions. Finally, in the HTO reactions the coke is burned generating carbon oxides and water. Both LTO and HTO reactions are generally believed to be heterogeneous gas/liquid or gas/solid reactions (Fassihi et al., 1984*b*; Castanier and Brigham, 2004). Oxygen from the gas stream diffuses to the surface of the oil/coke, adsorbs on the surface and reacts with a hydrocarbon component. The combustion products desorb and diffuse back into the gas stream. Each of these processes can be rate limiting, but it is generally assumed that the overall process is kinetically controlled (Islam et al., 1989).

LTO reactions are by far the least understood, and no generally accepted LTO reaction models exist today (Adegbesan et al., 1987). The role of LTO in controlling fuel availability is unclear, and LTO is generally regarded as undesirable. Negative effects of LTO include an increase in oil viscosity due to oxygen addition, and enhanced trapping of oil as a result of gas phase shrinkage (Moore et al., 2002*b*).

The ISC process is highly sensitive to reservoir heterogeneity and operating conditions. ISC projects may fail if insufficient air is injected. Reservoir heterogeneity may cause oxygen to be channeled around the front causing LTO reactions downstream. Excessive fuel deposition may choke the pores and retard the rate of advance of the combustion front, whereas insufficient fuel deposition may not provide enough heat for self-sustained combustion.

5.2.3 Reaction models

The minimal model

This model includes a minimal realistic set of components and reactions to represent ISC behavior. The components are in the model are light oil (LO), heavy oil (HO), coke (C), oxygen (O_2), water (W), and inert gas (IG). The model reactions are given by

$$\begin{aligned} \mathrm{LO} + \mathrm{O_2} &\rightarrow \mathrm{IG} + \mathrm{W} \\ \mathrm{HO} + \mathrm{O_2} &\rightarrow \mathrm{IG} + \mathrm{W} \\ \mathrm{HO} &\rightarrow \mathrm{LO} + \mathrm{C} + \mathrm{IG} \\ \mathrm{C} + \mathrm{O_2} &\rightarrow \mathrm{IG} + \mathrm{W}. \end{aligned} \tag{5.1}$$

The first two reactions model oxidation of the light and heavy oil, respectively. The cracking of heavy oil is modeled with the third reaction, while the last reaction models complete oxidation of the deposited fuel (coke). This minimal

Component Name	Abbreviation	Phase(s)
Water	H_2O	water
Inert oil	InertOil	oil
Oxidized resins/aromatics	OxdResAr	oil
Oxidized saturates	OxdSat	oil
Asphaltenes	Asph	oil
Resins	Resins	oil
Aromatics	Arom	oil/gas
Saturates	Sat	oil/gas
Light oil	Lites	oil/gas
Carbon dioxide	CO_2	oil/gas
Nitrogen	N_2	gas
Oxygen	O_2	gas
Oxidized asphaltenes	OxdAsph	solid
Pyrolysis coke	PyrCoke	solid

Table 5.1: List of (pseudo) components for the SARA based model. The components can exist in the phase(s) listed in the last column.

model is the common model used in many ISC simulations and it is the default model available in the commercial simulator CMG STARS (CMG, 2004).

The SARA based model

In the SARA (Saturates, Aromatics, Resins, and Asphaltenes) approach, chemical reactivity and phase behavior is taken into account when grouping the components. Saturates are saturated hydrocarbons with straight or branched chains, little ring-structure, and only little nitrogen, sulfur, and oxygen content. Aromatics contain one or more aromatic rings. Resins are the second heaviest fraction with high polarity due to considerable nitrogen, sulfur, and oxygen content. Asphaltenes are defined as the fraction of the crude insoluble in n-heptane. Within each fraction, groups are distinguished based on reactivity. A further subdivision of the fractions based on boiling point may be used to obtain improved representation of phase behavior.

The model we consider in this work contains 14 (pseudo) components, listed in Table 5.1, and the 14 reactions given below. Details of this model can be found in Freitag and Verkoczy (2005), Freitag and Exelby (2006) and Ren et al. (2005). The reactions include pyrolysis, LTO, and HTO of the SARA fractions along with HTO of partially oxidized LTO residue and the coke formed by pyrolysis. The LTO residues of resins, aromatics, and saturates are non-volatile

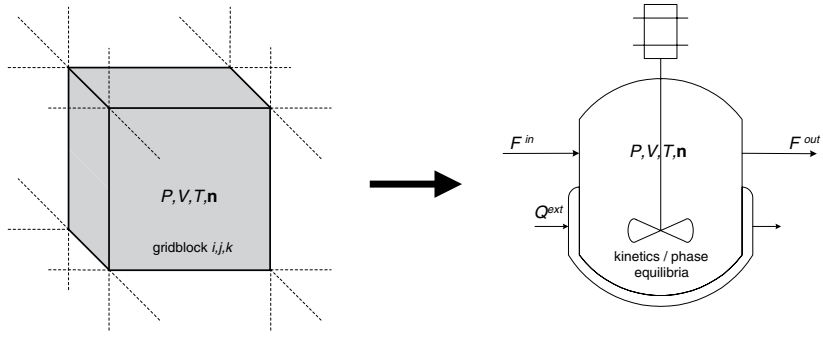

Figure 5.2: Using an operator splitting approach, each gridblock is effectively treated as a small chemical reactor.

oil components whereas the LTO residue of asphaltenes is solid.

$$
\begin{array}{ll}
\text{cracking/} & \left\{\begin{array}{lcl}
\text{Asph} & \rightarrow & \mathrm{H_2O} + \text{Arom} + \text{Sat} + \text{Lites} + \text{PyrCoke} \\
\text{Resins} & \rightarrow & \mathrm{H_2O} + \text{Asph} + \text{Arom} + \text{Sat} + \text{Lites} \\
\text{Arom} & \rightarrow & \text{Asph} + \text{Lites}
\end{array}\right. \\
\text{pyrolysis} & \\
\\
\text{LTO} & \left\{\begin{array}{lcl}
\text{Asph} + \mathrm{O_2} & \rightarrow & \mathrm{H_2O} + \mathrm{CO_2} + \text{OxdAsph} \\
\text{Resins} + \mathrm{O_2} & \rightarrow & \mathrm{H_2O} + \mathrm{CO_2} + \text{OxdResAr} \\
\text{Arom} + \mathrm{O_2} & \rightarrow & \mathrm{H_2O} + \mathrm{CO_2} + \text{OxdResAr} \\
\text{Sat} + \mathrm{O_2} & \rightarrow & \mathrm{H_2O} + \mathrm{CO_2} + \text{OxdSat}
\end{array}\right. \\
\\
\text{HTO} & \left\{\begin{array}{lcl}
\text{PyrCoke} + \mathrm{O_2} & \rightarrow & \mathrm{H_2O} + \mathrm{CO_2} \\
\text{OxdAsph} + \mathrm{O_2} & \rightarrow & \mathrm{H_2O} + \mathrm{CO_2} \\
\text{OxdResAr} + \mathrm{O_2} & \rightarrow & \mathrm{H_2O} + \mathrm{CO_2} \\
\text{OxdSat} + \mathrm{O_2} & \rightarrow & \mathrm{H_2O} + \mathrm{CO_2} \\
\text{Asph} + \mathrm{O_2} & \rightarrow & \mathrm{H_2O} + \mathrm{CO_2} \\
\text{Resins} + \mathrm{O_2} & \rightarrow & \mathrm{H_2O} + \mathrm{CO_2} \\
\text{Arom} + \mathrm{O_2} & \rightarrow & \mathrm{H_2O} + \mathrm{CO_2}
\end{array}\right.
\end{array}
\tag{5.2}
$$

5.3 Building a Virtual Kinetic Cell (VKC)

As mentioned in the introduction, we assume that the numerical model of our compositional and thermal process is based on operator splitting. Each grid block in a reaction substep is treated as a small chemical reactor, or kinetic cell, in which only chemical kinetics and phase behavior are taken into account, see Figure 5.2. In this way, the stiff reaction kinetics can be integrated with implicit

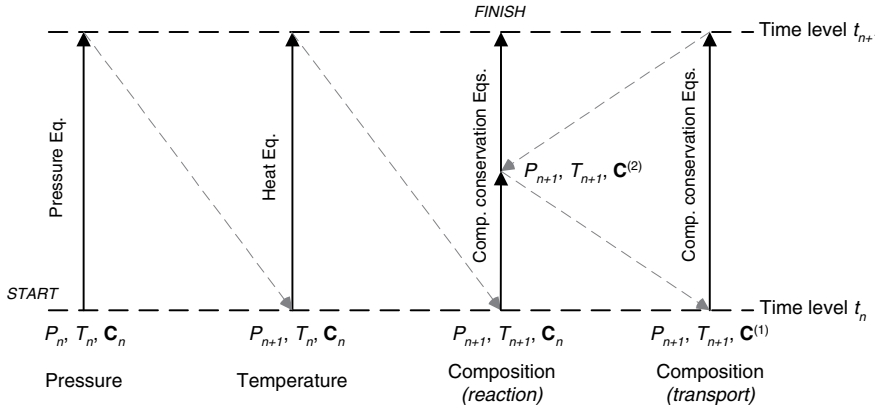

Figure 5.3: Illustration of the splitting scheme proposed by Younis and Gerritsen (2006) for thermally reactive, compositional reservoir simulation.

methods designed for stiff ODEs, whereas, for example, convective transport can be integrated with high-resolution explicit methods. The solutions to the subproblems are subsequently tied back together to form an approximation to the full equation.

Figure 5.3 illustrates one global time step of the scheme proposed by Younis and Gerritsen (2006) for reactive, compositional, and thermal reservoir simulation. It consists of five substeps. Initial conditions for each substep are indicated in the figure. In the first two substeps, the pressure and temperature are solved using an IMEX approach for the pressure and heat equations, respectively. Next, reaction and transport are solved using Strang splitting (Strang, 1968), as illustrated. We focus in this section on building a model for the reaction substep, which we will use later when designing efficient solvers. We have extended the model with inflow and outflow boundary conditions for mass and energy, as well as external heating and cooling terms to investigate possible interactions in the reservoir between gridblocks. For example, we can investigate the sensitivity to oxygen availability by varying the oxygen inflow rate. We can also apply the VKC in an inverse mode to determine kinetic parameters from data obtained through laboratory kinetic cell experiments.

We model a closed system consisting of 3 fluid phases (oil, water, and gas), an immobile solid phase, and the porous medium. Temperature, pressure, and component concentrations are assumed to be uniform in the cell. For convenience, we introduce the molar concentration c_i^j of a component $i, i = 1, \ldots, n_c$, in a phase j, $j \in \{o, w, g\}$, and the overall molar concentration C_i of component

i. They are given by

$$c_i^j = \phi_f x_i^j \xi^j S^j, \tag{5.3}$$

$$C_i = \sum_{j\in\{o,w,g\}} c_i^j, \tag{5.4}$$

where S^j are the phase saturations, ξ^j the molar phase densities, and x_i^j the mole fraction of component i in phase j. ϕ_f is the fluid porosity which varies with solid fuel concentration in the pore space according to

$$\phi_f = \phi_v - \frac{C_s}{\xi^s}, \tag{5.5}$$

where C_s and ξ^s are the density and concentration of the solid component, respectively. The solid concentration is defined with respect to total volume. The mass conservation of each chemical component can be expressed as

$$\frac{dC_i}{dt} = \sum_\gamma A_{i\gamma} R_\gamma + \frac{F_i^{in} - F_i^{out}}{V_T}, \qquad i = 1, \ldots, n_c. \tag{5.6}$$

Here, F_i^{in} and F_i^{out} are the molar flow rates of component i in and out of the cell, respectively, V_T is the cell volume, R_γ the kinetic expression for the γ^{th} chemical reaction, and $A_{i\gamma}$ is the stoichiometric coefficient for component i in reaction γ.

The energy conservation equation is given by

$$\frac{dU}{dt} = \sum_\gamma (-\Delta H_\gamma^r) R_\gamma + \frac{H^{in} - H^{out} + Q^{ext}}{V_T}, \tag{5.7}$$

where H^{in} and H^{out} are the fluxes of enthalpy in and out of the cell, and Q^{ext} is a heat source/sink term due to external heating or cooling, which is given by

$$Q^{ext} = -u_a (T - T^{ext}), \tag{5.8}$$

where T^{ext} is the heating/cooling temperature and u_a is an overall heat transfer coefficient.

Finally, the total internal energy of the system per unit volume, U, is given by

$$U = (1 - \phi_v) U^r + (\phi_v - \phi_f) \xi^s U^s + \phi_f \sum_{j\in\{o,w,g\}} \xi^j S^j U^j. \tag{5.9}$$

Since the cell volume is assumed constant, gases are allowed to leak out of the cell when volume changes occur due to chemical reactions and temperature changes. When only components in the gas phase can leave the cell, the molar flow rates in (5.6) may be expressed as

$$F_i^{out} = Q^{out} \xi^g x_i^g, \tag{5.10}$$

where ξ^g is the gas density and Q^{out} is the volumetric flow rate, given by

$$Q^{out} = k_v \left(P - P^{ext}\right). \tag{5.11}$$

Here, k_v denotes a valve coefficient.

Since pressure and temperature variations and chemical reactions cause volume changes, a constraint is needed in order for the fluid and solid volumes, V^f and V^s, to match the void pore volume, V_p. We set

$$V_p = V^f + V^s. \tag{5.12}$$

The chemical reactions occurring are assumed to be kinetically driven. They are modeled using the Arrhenius rate relations

$$K_\gamma = \alpha_\gamma \exp\left(-\frac{E_a^\gamma}{R_g T}\right), \tag{5.13}$$

where α_γ and E_a^γ are the pre-exponential factor and activation energy for reaction γ, respectively, and R_g is the universal gas constant. We will assume that the reactions are first order in all reactants. Oxidation reaction rates for components in phase j are modeled as

$$R_\gamma = K_\gamma \cdot \left(P x^g_{O_2}\right) \cdot \left(\phi_f \xi^j S^j x_i^j\right). \tag{5.14a}$$

For cracking/pyrolysis reactions, we use

$$R_\gamma = K_\gamma \cdot \left(\phi_f \xi^j S^j x_i^j\right). \tag{5.14b}$$

Reaction kinetic parameters for ISC models are normally obtained from laboratory experiments. It is still an open question how to upscale kinetics from the laboratory scale to the reservoir scale. Lacking better alternatives, we will use the laboratory parameters directly, as is generally done.

We assume that components partition into at most two phases, that components in the solid phase exist exclusively in this phase, and that the water phase consists of water only. For simplicity, the equilibrium between hydrocarbon components in the gas and oil phases is described by

$$K_i = \frac{x_i^g}{x_i^g}, \tag{5.15}$$

where the equilibrium factors are assumed to vary only with pressure and temperature according to

$$K_i = \frac{a_1}{P} \cdot \exp\left(\frac{a_2}{T - a_3}\right), \tag{5.16}$$

with a_1, a_2 and a_3 correlation constants. Using this simplified phase equilibrium description the flash calculation reduces to solving the Rachford-Rice equation for the molar gas phase fraction, β^g, given by

$$\sum_{i\in\{hc\}} (x_i^g - x_i^o) = \sum_{i\in\{hc\}} \frac{C_i(K_i - 1)}{1 - \beta^g + \beta^g K_i}. \tag{5.17}$$

The assumption that the equilibrium factors do not vary with composition is generally valid away from critical regions. The simplified phase description is a good starting point for model and algorithm development. In future work, we plan to extend the model with an equation-of-state (EoS) based phase equilibrium description. The challenges associated with this extension to a full phase equilibrium description are discussed in Section 5.6.

As primary variables we choose temperature, pressure and the n_c overall component concentrations. The VKC equations, (5.6), (5.7) and (5.12), comprise a set of differential-algebraic equations (DAEs). Including the total internal energy as a variable and Eqn. (5.9) as an extra constraint, we can write the DAE in semi-explicit form. In this formulation, temperature is aligned with the energy constraint (5.9) and pressure with the volume constraint (5.12). In multiphase regions Eqn. (5.17) is appended to the equation system and aligned with the gas phase fraction. The two ISC reaction models discussed in the previous section are used for testing and benchmarking.

We note at this point that the mass balance equations (5.6) are solved using overall component concentrations as dependent variables. For batch reactor problems in general, a reformulation is often used based on extent of reaction (Aris, 1989), which changes the number of ODEs from n_c to n_r. Thus, for problems with more components than independent reactions this may be advantageous. The extent of reaction concept has been generalized to open systems involving flow (Friedly, 1991; Friedly and Rubin, 1992). For certain reactive porous media transport problems in water resources modeling this generalized extent of reaction formulation leads to a reduced and simpler set of equations to be solved (Friedly and Rubin, 1992; Kräutle and Knabner, 2005). For the ISC problem, however, with a nonlinear transport part and component transfers between phases due to phase behavior, the reformulation is not directly applicable. We solve the ISC equations using overall quantities (such as total component concentrations) as primary variables. We therefore formulate the kinetic cell model in the same set of variables.

5.4 Numerical modeling

5.4.1 Choice of integration method for reactions

The kinetic cell equations consist of coupled ordinary differential equations (ODEs) and algebraic equations (AEs). We will consider the general form of

the resulting differential algebraic equation (DAE) system

$$\mathbf{M}\frac{d\mathbf{u}}{dt} = \mathbf{f}(t, \mathbf{u}), \qquad \mathbf{u}(t_0) = \mathbf{u}_0, \tag{5.18}$$

where $\mathbf{u} \in \mathbb{R}^m$ is a vector of state variables depending on t, and $\mathbf{f}$ is a vector function mapping $\mathbb{R} \times \mathbb{R}^m$ into $\mathbb{R}^m$. For the kinetic cell model the mass matrix, $\mathbf{M} \in \mathbb{R}^m \times \mathbb{R}^m$, is simply a diagonal matrix. The diagonal elements M_{ii} are one when the i^{th} equation is a differential equation, and zero when it is algebraic. The initial conditions are assumed consistent with the algebraic constraints. In the VKC model, the right-hand-side functions may be discontinuous because of phase changes. The number of elements in the state vector is typically between 10 and 20. We require results to have between 2 and 4 correct significant digits (relative accuracy between $10^{-2} - 10^{-4}$). This requirement is based on our expectations of the temporal and spatial accuracies in other parts of the equations. As we will show later, the performance of the proposed methods is not sensitive to small variations in the required accuracy.

The short integration intervals between operator splitting updates in the VKC and the stiff reaction kinetics are the primary characteristics guiding our choice of integration method. When integrating from t^n to t^{n+1} one-step methods only use state information from t^n whereas multi-step methods use information from several previous integration steps, t^{n-j}, with $j = 0, 1, \ldots, s$ (Hairer et al., 1996). Multi-step methods are often implemented in a variable order formulation, in which they start out at low order and with small time steps. They build up to higher order as more information becomes available, and are, at that stage, generally outperforming one-step methods. This suggests that multi-step methods are attractive for problems with long and smooth integration intervals, whereas one-step methods are preferable on shorter intervals and on problems with frequent discontinuities in the solution. Hence, we will focus here on one-step methods. Of the one-step methods, we limit ourselves to the family of Runge-Kutta (RK) methods (Runge, 1895; Kutta, 1901), which are well studied in the literature. Other classes of methods could be considered also, such as the Rosenbrock methods (Rosenbrock, 1963) or the extrapolation methods (Hairer et al., 1996), but we will consider Runge-Kutta methods exclusively in this paper. For stability reasons we shall further limit our search to implicit RK methods that allow efficient integration of the stiff kinetics.

A general s-stage Runge-Kutta scheme for solving the DAE system (5.18) may be expressed as:

$$\mathbf{M}\mathbf{U}_i = \mathbf{M}\mathbf{u}_n + \Delta t^n \sum_{j=1}^{s} a_{ij}\mathbf{f}(t^n + c_j\Delta t^n, \mathbf{U}_j), \tag{5.19a}$$

$$\mathbf{M}\mathbf{u}_{n+1} = \mathbf{M}\mathbf{u}_n + \Delta t^n \sum_{i=1}^{s} b_i\mathbf{f}(t^n + c_i\Delta t^n, \mathbf{U}_i). \tag{5.19b}$$

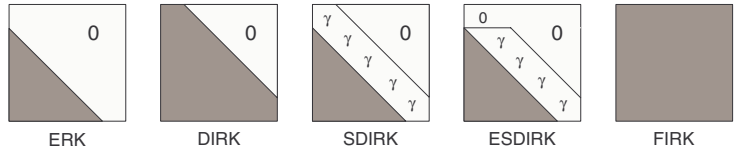

Figure 5.4: Structure of the **A** matrix in the Butcher tableau for different classes of RK methods.

Here, $\mathbf{U}_i$ denotes the solution at the i^{th}, $(i = 1, \ldots, s)$, internal stage of integration step n and Δt^n denotes the time step length.

$$\begin{array}{c|cccc} c_1 & a_{11} & a_{12} & \ldots & a_{1s} \\ c_2 & a_{21} & a_{22} & \ldots & a_{2s} \\ \vdots & \vdots & \vdots & \ddots & \vdots \\ c_s & a_{s1} & a_{s2} & \ldots & a_{ss} \\ \hline \mathbf{u}_{n+1} & b_1 & b_2 & \ldots & b_s \end{array} = \begin{array}{c|c} \mathbf{c} & \mathbf{A} \\ \hline & \mathbf{b}^T \end{array} \tag{5.20}$$

Runge-Kutta methods are classified according to the structure of their Butcher tableau as illustrated in Figure 5.4. For explicit methods (ERK), the matrix **A** is strictly lower triangular, which implies that all the internal stages (5.19a) can be calculated explicitly, making ERK methods computationally fast and straightforward to implement. However, ERK methods generally have poor stability properties, which make them unsuitable for stiff problems (Hairer et al., 1996). The four remaining subclasses of Runge-Kutta methods are all implicit, that is, the values of the internal stages are no longer calculated explicitly from the values of the previous stages. Each integration step of an implicit method requires the solution of a system of ms nonlinear equations. Normally, an iterative method, such as Newton's method, is applied. For diagonally implicit RK (DIRK) methods, the stage values can be calculated sequentially. Hence, the computational costs of DIRK methods are lower than those of fully implicit RK (FIRK) methods, for which all ms equations must be solved simultaneously. If all diagonal elements of **A** are identical and its upper diagonal elements are zero, the method is said to be a singly diagonally implicit (SDIRK). If the first stage of an SDIRK method is explicit, the method is said to be explicit singly diagonally implicit (ESDIRK).

For our purposes, the ESDIRK methods, for which the general form of the Butcher tableau can be found in e.g. Kværnø (2004), are attractive. The diagonal structure of these methods allows sequential evaluation of the internal stages, and because the diagonal elements are equal, the iteration matrix for solving the nonlinear stage equations (5.19a) need only be evaluated and factorized once per integration step. ESDIRK methods can be constructed such that they are both A- and L-stable as well as stiffly accurate (Hairer and Wanner, 1996). Stiffly

accurate methods avoid the order reduction phenomenon observed by Prothero and Robinson (1974) when applied to stiff ODEs. Also, the explicit first stage of ESDIRK methods ensures high stage order (≥ 2) which is important for the order of accuracy in the algebraic components of the DAE (Hairer and Wanner, 1996). An additional advantage of having high stage order is that it allows the construction of high order interpolants to be used for generating output between mesh-points. We will exploit these interpolants when constructing an algorithm for locating the discontinuities that occur due to phase changes.

The Butcher tableau for ESDIRK methods takes the following form

$$\begin{array}{c|cccccc} 0 & 0 & 0 & & & & \\ c_2 & a_{21} & \gamma & 0 & & & \\ c_3 & a_{31} & a_{32} & \gamma & 0 & & \\ \vdots & \vdots & \vdots & \ddots & \ddots & \ddots & \\ c_{s-1} & a_{s-1,1} & a_{s-1,2} & a_{s-1,3} & \cdots & \gamma & 0 \\ 1 & b_1 & b_2 & b_3 & \cdots & b_{s-1} & \gamma \\ \hline \mathbf{u}_{n+1} & b_1 & b_2 & b_3 & \cdots & b_{s-1} & \gamma \end{array} \tag{5.21}$$

Alexander (2003) proposed a four stage ESDIRK method of order 3 with an embedded error estimator of order 4. Williams et al. (2002) also published a four stage ESDIRK method suited for index 2 DAEs, but with orders 2 and 3 for the error estimator and advancing method, respectively. Finally, Kværnø (2004) recently published a range of ESDIRK methods of orders 3 to 5 emphasizing strong stability properties of both the error estimator and the advancing method. ESDIRK methods have been applied as time integrators in fully implicit fluid dynamics simulations (Bijl et al., 2002) as well as in operator splitting methods for integrating the reaction part of convection-diffusion-reaction equations (Kennedy and Carpenter, 2003).

5.4.2 Efficient implementation

We implemented four ESDIRK methods of orders 2-5. The lowest order method is simply the trapezoidal rule. When combined with the implicit Euler method we have an embedded pair of methods of orders 1 and 2. We refer to this method as ESDIRK12 and use a similar notation for higher order ESDIRK schemes. The bulk of the computational costs in an ESDIRK method is in the solution of the nonlinear algebraic equations that arise in each internal stage. Efficient control of the iterative scheme applied to these equations and of the discretization error by step size adjustments are the two main design challenges.

Error and convergence control

The step size is adapted based on an error estimate for the lowest order method obtained by subtracting the two solutions of orders p and $p-1$. This error

estimate is essentially free, since it involves no additional function evaluations or system solves.

Adjusting the step size to meet an accuracy requirement is, in essence, a control problem. We implemented the predictive controller

$$\Delta t^n = \frac{\Delta t^{n-1}}{\Delta t^{n-2}} \left(\frac{\varepsilon}{r_n} \right)^{k_2/(p+1)} \left(\frac{r_{n-1}}{r_n} \right)^{k_1/(p+1)} \Delta t^{n-1} \tag{5.22}$$

suggested by Gustafsson (1992). In Eqn. (5.22) k_1 and k_2 are the gain parameters for the controller, while ε is the desired tolerance (including a safety factor). Gustafsson (1992) suggests using $k_1 = k_2 = 1$ based on experiments, where the number of integration steps is measured for a given problem as a function of k_1 and k_2. The number of steps required is not sensitive to k_1 and k_2 for the interval $[k_1, k_2] \in [0.5, 1.5\ ;\ 0.5, 1.5]$. Within this interval, variations in k_1 and k_2 result in changes in the number of integration steps of less than 5%. Our experiments using the VKC model show similar results, so we choose $k_1 = k_2 = 1$. The variable r_n is the norm of the estimated local error at t^n, given by

$$r_n = \sqrt{\frac{1}{m} \sum_{i=1}^{m} \left(\frac{err_i}{atol_i + rtol_i \cdot |u_i|} \right)^2} \tag{5.23}$$

in which *atol* and *rtol* are (componentwise) absolute and relative error tolerances specified by the user. Experiments have shown that the controller (5.22) gives a small reduction in the number of failed integration steps along with a smoother variation of step sizes compared to the conventional control law $\Delta t^n = (\varepsilon / r_n)^{1/(p+1)} \Delta t^{n-1}$ that is commonly implemented in ODE solvers.

Stage value predictions

The nonlinear equations arising in each internal stage of the ESDIRK methods are solved using a modified Newton's method given by

$$\left[\mathbf{M} - \Delta t^n \gamma \frac{\partial \mathbf{f}}{\partial \mathbf{u}} \right] \Delta \mathbf{U}_i = \mathbf{M}\mathbf{u}_n + \Delta t^n \sum_{j=1}^{i-1} a_{ij} \mathbf{f}(t^n + c_j \Delta t^n, \mathbf{U}_j^{(k)}) - \mathbf{M}\mathbf{U}_i^{(k)}, \tag{5.24a}$$

$$\mathbf{U}_i^{(k+1)} = \mathbf{U}_i^{(k)} + \Delta \mathbf{U}_i. \tag{5.24b}$$

The iteration matrix $\mathbf{M} - \Delta t^n \gamma \partial \mathbf{f} / \partial \mathbf{u}$ is evaluated and factorized once per integration step. Because the state dimension is low, modified Newton approaches, where the Jacobian is reused over several consecutive steps, will not have a significant impact. Hence, we re-evaluate and factorize the iteration matrix in each integration step. We construct an initial guess for the stage value

at each internal stage by continuous extension of the method as suggested in (Enright et al., 1986). The continuous extension is given by

$$\mathbf{u}(t^n + \theta\Delta t^n) = \mathbf{u}_n + \Delta t^n \sum_{i=1}^{s} b_i^*(\theta)\mathbf{f}(t^n + c_i\Delta t^n, \mathbf{U}_i), \tag{5.25}$$

where the quadrature weights, b_i^*, depend on θ according to

$$b_i^*(\theta) = b_{i,1}^*\theta + b_{i,2}^*\theta^2 + \ldots + b_{i,p}^*\theta^p. \tag{5.26}$$

The coefficients for the continuous extension are determined by requiring that the set of order conditions used to determine the coefficients of the ESDIRK method itself is satisfied. A prediction of the stage value at the i^{th} internal stage is then obtained by substituting $\theta_i = 1 + c_i\Delta t^{n+1}/\Delta t^n$ in (5.25).

The iterations are terminated when

$$\|\mathbf{R}^{(k)}\|_2 \leq \kappa \cdot rtol, \tag{5.27}$$

with $\mathbf{R}$ the scaled vector of residuals, $rtol$ the relative error tolerance for the local discretization error. The parameter κ is normally chosen between 0.5 and 0.01. For reasons of robustness we chose $\kappa = 0.01$, such that the errors allowed in the iteration process are much smaller and do not interfere with the estimation and control of the local integration error. Experiments show that the cost of the extra iterations needed using $\kappa = 0.01$ compared to, for example, $\kappa = 0.1$, is minor, since the tighter value of κ also reduces the total number of integration steps.

During iterations the convergence rate is estimated as

$$\alpha_k = \frac{\|\mathbf{R}^{(k)}\|_2}{\|\mathbf{R}^{(k-1)}\|_2}. \tag{5.28}$$

If for some k during iterations $\alpha_k > 1$, the iterations are terminated and the step size decreased. The estimated convergence rate is also used by the step size controller to limit the step size if convergence in the previous step was too slow. A target minimum convergence rate of 0.3 is used as suggested by Gustafsson (1992) which from experiments on small scale problems similar to the VKC was found to balance the trade-off between many short integration steps, but with rapid convergence, and longer steps requiring more iterations per step.

5.4.3 Discontinuities due to phase changes

Phase changes in the VKC cause discontinuities in the right-hand-side functions of Eqn. (5.6) and (5.7). Straightforward integration across these discontinuities may lead to non-physical phase changes, poor convergence and repeated step failures. In this section, we propose an algorithm for robust detection and

location of phase changes by considering the kinetic cell as a discrete event problem. The appearance or disappearance of a fluid phase marks the occurrence of a "discrete event", e.g. a change from a single phase region to a two-phase region, or vice-versa. The time of the phase change can not be determined a priori. The detection of a phase change and subsequent location of the exact time of change are the main components of the proposed discrete event algorithm.

Discrete event systems

We will represent the discrete event DAE system in the following form:

$$\frac{d\mathbf{v}}{dt} = \mathbf{f}(t, \mathbf{v}, \mathbf{w}), \qquad \mathbf{v}(t_0) = \mathbf{v}_0 \tag{5.29a}$$

$$0 = \mathbf{g}(t, \mathbf{v}, \mathbf{w}), \qquad \mathbf{w}(t_0) = \mathbf{w}_0 \tag{5.29b}$$

$$0 < q_j(t, \mathbf{v}, \mathbf{w}), \qquad j = 1, \ldots, n_{ev} \tag{5.29c}$$

where the DAE system, originally given in Eqn. (5.18), has been reformulated in semi-explicit form. Now, $\mathbf{v} \in \mathbb{R}^{m_d}$ is the vector of differential variables and $\mathbf{w} \in \mathbb{R}^{m_a}$ is the vector of 'algebraic' variables. $\mathbf{f}$ and $\mathbf{g}$ are vector functions mapping $\mathbb{R} \times \mathbb{R}^{m_d} \times \mathbb{R}^{m_a}$ into $\mathbb{R}^{m_d}$ and $\mathbb{R}^{m_a}$, respectively. We will assume that $\partial\mathbf{g}/\partial\mathbf{v}$ is non-singular (index one DAE). The q_j's are event functions associated with the current system state and n_{ev} denotes the number of event functions. In general, the system may change between many different states. If the attainable states are indexed as $p \in \mathcal{I}_{state}$ then each state is represented in the form (5.29) with $\{m_d, m_a, n_{ev}\}_p$.

To illustrate the concepts we consider the discrete event formulation of the VKC. We neglect changes associated with the water phase and consider only the two-phase equilibrium between hydrocarbon components in the oil and gas phases. Three attainable states exist for this system: (1) single phase oil, (2) single phase gas, and (3) two-phase oil-gas. In the two-phase region, the active equations for the VKC are

$$\frac{dC_i}{dt} = \sum_\gamma A_{i\gamma} R_\gamma + \frac{F_i^{in} - F_i^{out}}{V_T}, \qquad i = 1, \ldots, n_c, \tag{5.30a}$$

$$\frac{dU}{dt} = \sum_\gamma (-\Delta H_\gamma^r) R_\gamma + \frac{H^{in} - H^{out} + Q^{ext}}{V_T}, \tag{5.30b}$$

$$0 = U - \left[(1 - \phi_v) U^r + (\phi_v - \phi_f) \xi^s U^s + \phi_f \sum_j \xi^j S^j U^j \right], \tag{5.30c}$$

$$0 = V_p - V^f - V^s, \tag{5.30d}$$

$$0 = \sum_{i \in \{hc\}} \frac{C_i (K_i - 1)}{1 - \beta^g + \beta^g K_i}. \tag{5.30e}$$

Here, $m_d = n_c + 1$, $m_a = 3$ and $n_{ev} = 2$. The two event functions associated with the two-phase region are

$$0 < \sum_{i \in \{hc\}} C_i(1 - K_i), \tag{5.31}$$

$$0 < \sum_{i \in \{hc\}} C_i \left(1 - \frac{1}{K_i}\right), \tag{5.32}$$

corresponding to disappearance of the gas phase and the oil phase, respectively. When a change to a single phase region occurs, Eqn. (5.30e) is omitted from the formulation. Each single phase state then has one associated event function defining the criterion for a switch back to the two-phase region.

Discrete event algorithm

Several general purpose event detection algorithms have been suggested in the literature, see, for example, Park and Barton (1996) and Thomsen (2006). Our event detection algorithm is based on the principle of discontinuity locking (Park and Barton, 1996). Within each integration step the system is locked in its current state, even if one or more event functions are satisfied. The event functions are evaluated at the end of each step, and if any of them are satisfied, the exact time of occurrence is located. The approach is based on the assumption that the system of equations is mathematically well behaved in a small neighborhood of the phase changes.

Since the changes often occur between mesh points, we need to interpolate the differential and algebraic variables of the DAE in order to evaluate the event functions. For differential variables we use the continuous extension (5.25) provided by the ESDIRK methods. The algebraic variables could, in principle, also be interpolated by a suitable polynomial. However, after location of the event, a consistent initialization calculation is required to restart the integration in the new system state. That is, based on values for the differential variables, the algebraic constraints are solved to find consistent initial values for the algebraic variables. This consistency calculation may result in the numerical phenomenon referred to as *discontinuity sticking* (Park and Barton, 1996). The problem is illustrated in Figure 5.5.

Assume that the event function $q^*(t, \mathbf{v}, \mathbf{w}) > 0$ was satisfied in the integration step $[t^n, t^{n+1}]$. The exact event time, t^*, may than be located by solving the scalar equation

$$q^*(t^*, \mathbf{v}^p(t^*), \mathbf{w}^p(t^*)) = \delta, \tag{5.33}$$

where $\mathbf{v}^p(t)$ and $\mathbf{w}^p(t)$ are interpolating polynomials for the differential and algebraic variables, respectively. δ is a small tolerance employed to ensure $q^* > 0$ at t^*. However, a consistent initialization at t^* may result in values of the algebraic variables that are different from $\mathbf{w}^p(t^*)$ if t^* does not coincide with

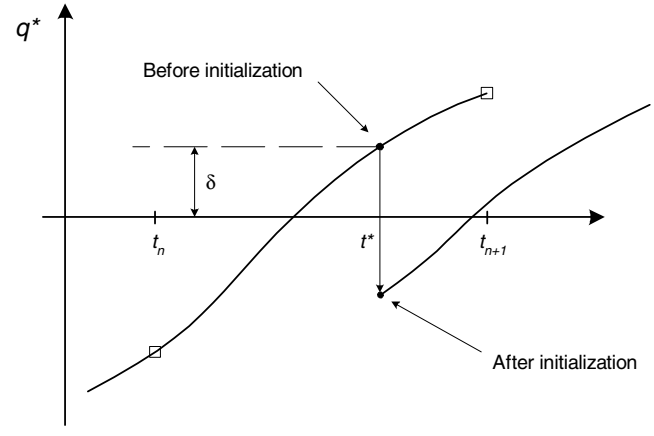

Figure 5.5: Illustration of discontinuity sticking resulting from inconsistent algebraic variables. (Figure adapted from Park and Barton (1996)).

the mesh points or the internal quadrature nodes of the ESDIRK scheme

$$\mathbf{w}^p(t^*) \neq \mathbf{w}(t^*), \qquad \text{if} \qquad t^* \neq t^n + c_i \Delta t^n, \quad i = 1, \ldots, s. \tag{5.34}$$

Consequently, the value of the event function may have changed

$$q^*(t^*, \mathbf{v}^p(t^*), \mathbf{w}^p(t^*)) \neq q^*(t^*, \mathbf{v}^p(t^*), \mathbf{w}(t^*)), \tag{5.35}$$

and the event function may no longer be satisfied ($q^*(t^*, \mathbf{v}^p(t^*), \mathbf{w}(t^*)) < 0$). If this is the case, the same event is detected again immediately in the next integration step.

To avoid discontinuity sticking problems, we locate the phase changes by solving the system of equations

$$\mathbf{g}(t^*, \mathbf{v}^p(t^*), \mathbf{w}(t^*)) = 0 \tag{5.36a}$$

$$q^*(t^*, \mathbf{v}^p(t^*), \mathbf{w}(t^*)) = \delta, \tag{5.36b}$$

where the unknowns are the algebraic variables, $\mathbf{w}$, and the event time, t^*. Only few Newton iterations are required to solve (5.36), since good starting guesses are available. The structure of the ESDIRK integration algorithm with discrete event detection is given by

Require: $t_{initial}$, t_{final}, $\mathbf{u}(t_{initial})$, initial system state
  while $t \leq t_{final}$ **do**
    Advance solution from t^n to t^{n+1} using the ESDIRK scheme
    Compute error estimate
    if *integration_error_acceptable* **then**

Initial and operational conditions	
Water	0.00 moles
Light oil	0.00 moles
Heavy oil	0.55 moles
Oxygen	0.00 moles
Inert gas	0.45 moles
Coke	0.00 moles
Temperature	373 K
Pressure	13.88 MPa [137 atm]
Total cell volume	$0.0014\,\mathrm{m}^3$
Air feed rate	$2.78 \cdot 10^{-6}\,\mathrm{m}^3/\mathrm{s}$ [$10\,\mathrm{L}/\mathrm{hr}$]
Rock porosity	0.40
Heat transfer coefficient	$60\,\mathrm{kJ}/\mathrm{mole \cdot K}$
Valve coefficient	$2.74 \cdot 10^{-11}\,\mathrm{m}^3/\mathrm{s \cdot Pa}$ [$10\,\mathrm{L}/\mathrm{hr \cdot atm}$]

Table 5.2: Initial and operational conditions for simulating the ramped temperature experiment using the VKC.

```
    Evaluate event functions
    if sign_change_occurred then
      Locate time of change by solving (5.36)
      Set time equal to t*
      Initialize in new system state
    end if
    Adjust time step based on error estimate
  else
    Recompute time step with reduced Δt
  end if
end while
```

5.5 Results

5.5.1 VKC simulation of a ramped temperature experiment

As a first example, we illustrate the VKC by simulating a ramped temperature experiment using the minimal reaction model presented in Section 5.2.3. Ramped temperature experiments are often carried out in the laboratory to determine burning characteristics for different oils.

The simulated setup consists of an oil sample placed in the kinetic cell which is heated externally from 373 K to 873 K over a period of 10 hours with a con-

stant feed of air of $2.78 \cdot 10^{-6}\,\mathrm{m^3/s}$ [$10\,\mathrm{L/hr}$]. Initial and operational conditions are summarized in Table 5.2. Figure 5.6 shows the cell temperature, oxygen consumption rate, and concentrations of light oil, heavy oil, coke, and oxygen at 3 different concentrations of oxygen in the feed.

The minimal reaction model used in this experiment does not include LTO reactions in the traditional sense of oxygen addition reactions, but we still observe two peaks in oxygen consumption rate originating from direct oxidation of the oil based components and oxidation of coke which occurs at a higher temperature. The variation with oxygen feed concentration shows that, as expected, a low oxygen concentration promotes cracking of heavy oil whereas a high oxygen concentration favors the direct oxidation which leads to a significant increase in temperature.

In the second example we study the influence of the activation energy. We again simulate the ramped temperature experiment with an oxygen feed concentration of 21%. We perform a base simulation using the original reaction parameters and two perturbed simulations, in which we first increase and then decrease activation energies for all reactions by a factor of 2. We choose the pre-exponential factors such that the nominal and perturbed reaction rate constants coincide at a specified temperature, so that

$$\alpha_{perturbed} = \alpha_{nominal} \cdot \exp\left(\frac{1}{R_g T_{coin.}}\left(E_{perturbed} - E_{nominal}\right)\right). \tag{5.37}$$

Here, $E_{nominal}$ and $E_{perturbed}$ refer to the nominal and perturbed activation energies, respectively, and $T_{coin.}$ is the temperature at which the two rate expressions coincide. We choose $T_{coin.} = 623\,\mathrm{K}$, which corresponds to the mean temperature during the simulation.

Figure 5.7 shows the cell temperature, oxygen consumption rate, and concentrations of light oil, heavy oil, coke, and oxygen at the three different activation energies. Again, we see two peaks in oxygen consumption rate originating from direct oxidation of the oil components and oxidation of coke. Increasing the activation energies results in an initial delay of the reaction onset time, but a more rapid oxidation of oil and coke after onset, which is also reflected in the increase in oxygen consumption rate.

5.5.2 Phase changes

For the case with 20% oxygen in the feed, a change from single phase oil to two-phase oil-gas occurs at $t = 3.15\,\mathrm{hrs}$. Attempting to integrate directly across the phase change results in repeated step failures in the solver as illustrated in Figure 5.8. The figure shows the step size sequence as selected by the controller (5.22) for a section of the integration interval near the phase change. Each time the solver attempts a step across the phase boundary, a convergence or error test failure results forcing the solver to reduce the step size. The solver fails 8 times and reduces the step size by a factor of 100 before stepping across

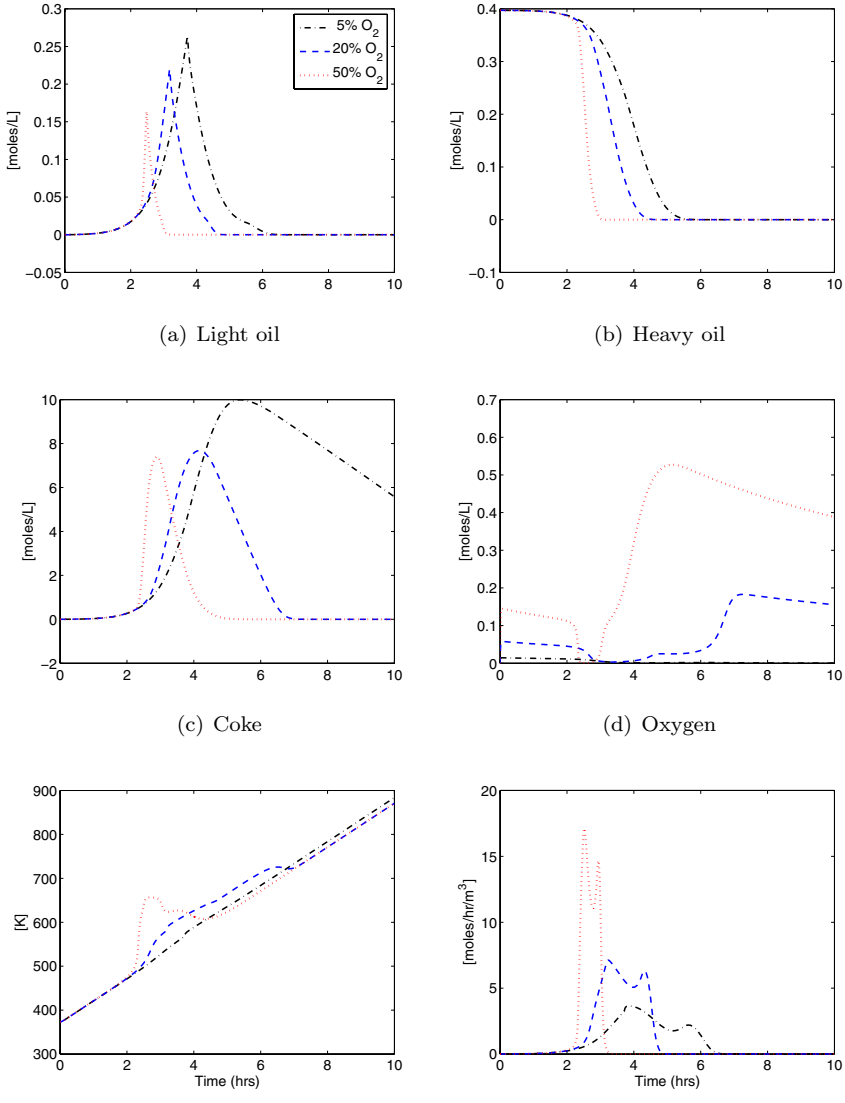

(a) Light oil

(b) Heavy oil

(c) Coke

(d) Oxygen

(e) Temperature

(f) Oxygen consumption rate

Figure 5.6: Simulation results from a ramped temperature experiment using the minimal reaction model. The temperature is raised from 373 K to 873 K over a period of 10 hours. Cell temperature, oxygen consumption rate, and component concentrations are shown for 3 different oxygen feed concentrations.

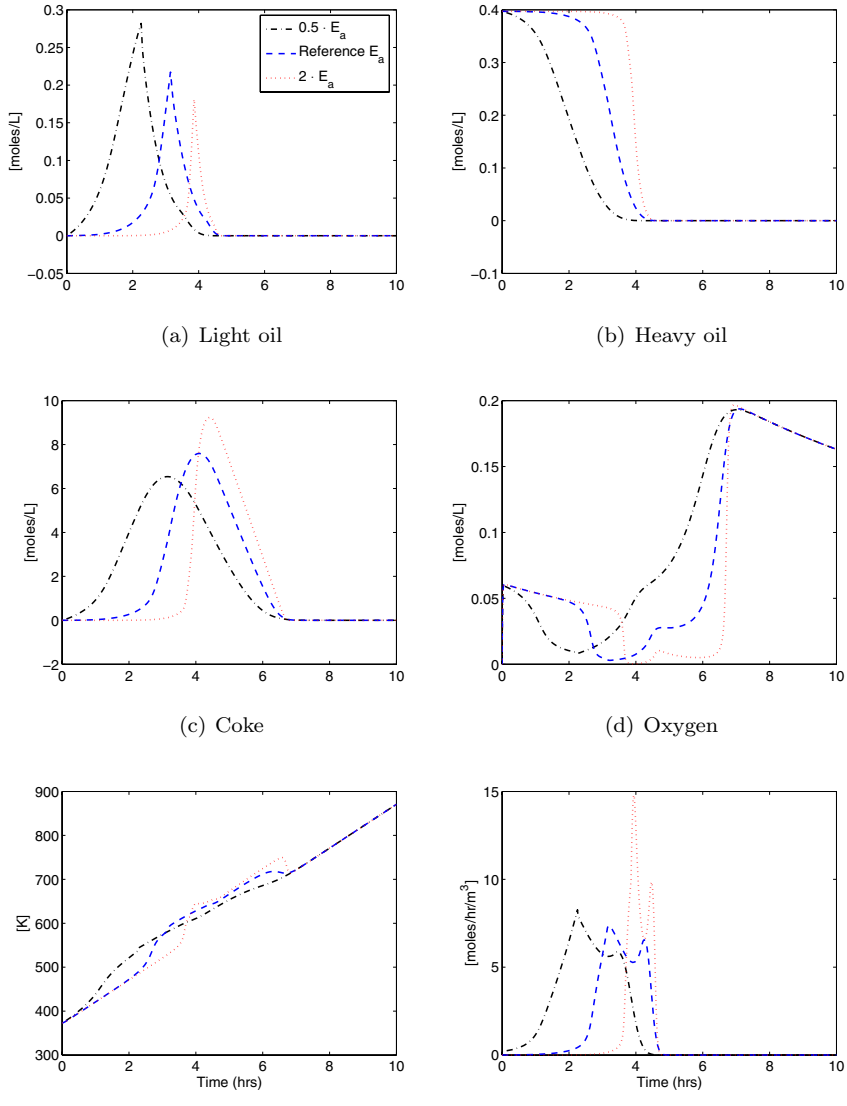

(a) Light oil

(b) Heavy oil

(c) Coke

(d) Oxygen

(e) Temperature

(f) Oxygen consumption rate

Figure 5.7: Simulation results from a ramped temperature experiment using the minimal reaction model. The temperature is raised from 373 K to 873 K over a period of 10 hours. Cell temperature, oxygen consumption rate, and component concentrations are shown for at 3 different reaction activation energies.

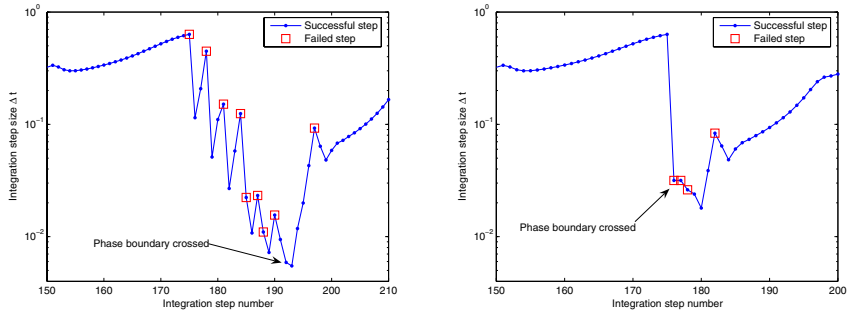

(a) Without phase change detection.

(b) With phase change detection.

Figure 5.8: Step size sequences for the ESDIRK23 solver near a phase change when simulating the ramped temperature experiment. The phase change algorithm improves the integration robustness when crossing phase boundaries.

successfully. Using the phase change detection algorithm, the change is detected and consistently located without failed steps. Initialization in the new two-phase region, however, results in 4 step failures and a step size reduction by a factor of approximately 30. Completely avoiding step failures and step size reductions is difficult since a change into the two-phase region changes the dynamics of the problem.

5.5.3 Performance comparison

To evaluate the performance of the new, tailored ESDIRK implementations we have compared them to two stiff ODE solvers that are commonly used: DASSL (Petzold, 1982) and LSODE (Hindmarsh, 1983). Both solvers are based on backward differentiation formulas (BDF), and are variable order. We show results for four ESDIRK methods, namely

ESDIRK12: Two stage, second order trapezoidal rule with implicit Euler as error estimator.

ESDIRK23: Three stage method, described in Kværnø (2004). Second order method with third order error estimator.

ESDIRK34: Four stage method, described in Alexander (2003). Optimal third order method with fourth order error estimator.

ESDIRK45: Seven stage method, described in Kværnø (2004). Fourth order method with fifth order error estimator.

Coefficients for the methods can be found in the cited references.

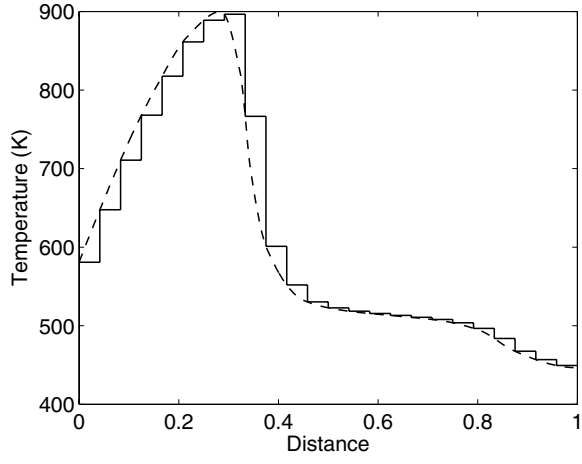

Figure 5.9: The temperatures for the integration subintervals in the performance comparison are obtained by sampling the characteristic ISC temperature profile. The continuous temperature profile is shown along with a zero-order parametrization corresponding to $N = 25$ equidistant subintervals.

We split the total integration interval into N subintervals. We assume the pressure is constant throughout the entire integration. The temperature is kept fixed in each subinterval. Its value is obtained by sampling the characteristic ISC temperature profile as shown in Figure 5.9. Thus, we mimic implementation of the solvers within an operator splitting environment for the full ISC equations. In each subinterval the VKC equations reduce to the set of ODEs given by Eqn. (5.6), along with the phase equilibrium constraint (5.17). For DASSL and LSODE, which are not equipped with functionality for handling discontinuities due to phase changes, we solve the implicit equation (5.17) whenever the ODE right-hand-side functions are evaluated.

We use the SARA based reaction model presented in Section 5.2.3. In terms of number of components and reactions we think that this model best represents the requirements in realistic ISC simulations. We assume ideal fluid phases and use a pressure and temperature correlation for the equilibrium K-factors. Initial compositions are listed in Table 5.3. A pressure of 2.023 MPa [20 atm] is used in all subintervals . Air is cycled through the cell at a constant rate. The total simulation time is 100 hrs and two experiments are carried out using $N = 25$ and $N = 100$ subintervals, respectively.

The numerical results are compared to a very accurate reference solution computed by ESDIRK34 using $atol = rtol = 10^{-14}$. The measure of accuracy is based on the max-norm of the relative error at the end of the integration interval. The accuracy is represented as the minimum number of significant

Component	Mole fraction
Water	0.0000
Inert oil	0.0005
Oxidized resins/aromatics	0.0000
Oxidized saturates	0.0000
Asphaltenes	0.0229
Resins	0.0914
Aromatics	0.2680
Saturates	0.5625
Light oil	0.0547
Carbon dioxide	0.0000
Nitrogen	0.0000
Oxygen	0.0000
Oxidized asphaltenes	0.0000
Pyrolysis coke	0.0000

Table 5.3: Initial overall oil composition for the SARA based model.

correct digits, SCD, in the solution, defined as

$$\mathrm{SCD} := -\log_{10}\left[\max_i \left|\frac{u_i(t_{end}) - u_i^{ref}(t_{end})}{u_i^{ref}(t_{end})}\right|\right]. \tag{5.38}$$

Solver comparisons are presented as work-precision diagrams where efficiency is measured using CPU time. Thus, to produce the diagrams the problem is solved using a range of input tolerances for each of the solvers tested. All codes are compiled using the Compaq Visual Fortran compiler with the same optimization settings. The CPU time for each case is averaged over 25 runs on a Pentium 4, 3GHz PC with 512MB RAM. The input tolerances are chosen as $atol = rtol = 10^{-(1+j/3)},\ j = 0, \ldots, 21$. The initial integration step size is computed internally by the solvers. For this purpose, the ESDIRK solvers use the algorithm suggested by Hairer and Wanner (1996). Between subintervals the last step of the current interval is passed as a guess for the first step in the next interval. All solvers require the Jacobian of the ODE right-hand-side functions. These are computed analytically using the automatic differentiation tool Tapenade ver. 2.2 (Hascoët and Pascual, 2004).

Figure 5.10 shows the work-precision diagrams when solving the SARA based reaction model using 25 and 100 subintervals. The resulting accuracies in the solution are, of course, different from the local tolerances provided as input to the solvers that govern the local error and step size control. In the high accuracy range (4–6 significant correct digits) the methods perform according to their order: The high order methods (DASSL, LSODE and ESDIRK45) outperform

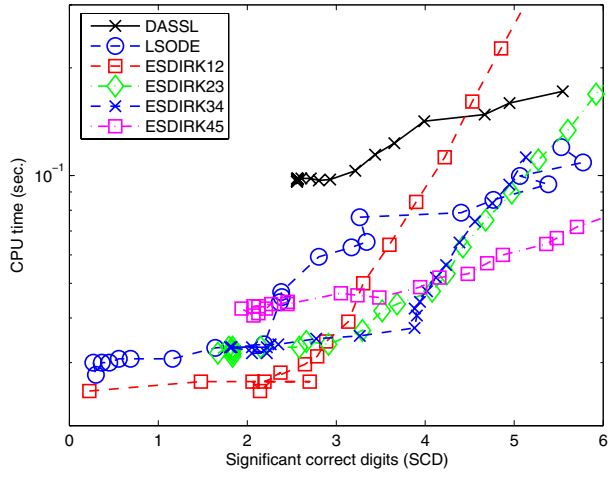

(a) 100 subintervals.

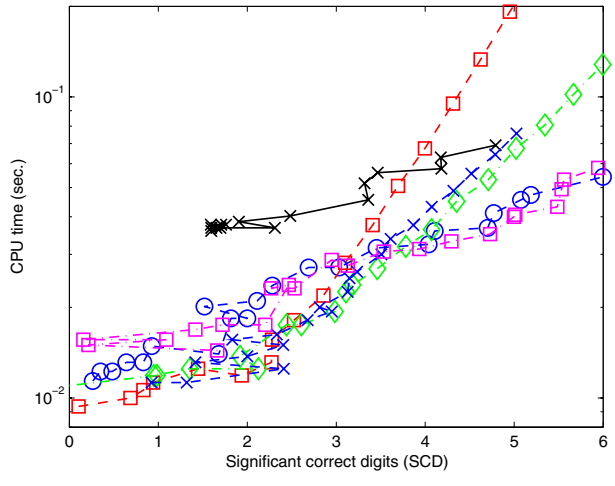

(b) 25 subintervals.

Figure 5.10: Work-precision diagrams for the SARA based ISC reaction model. The tailored ESDIRK implementations are compared to the widely used DASSL and LSODE codes. Comparisons are made for 25 and 100 subintervals

the lower order methods (e.g. ESDIRK12 and ESDIRK23). However, we are mainly interested in the accuracy range corresponding to 2–4 significant correct

digits, since we expect the accuracies obtained in other parts of the equation to fall in this range. The low and intermediate order methods perform best in this range. For example, with 100 subintervals and 3 significant correct digits the ESDIRK23 solver is two times faster than LSODE and 3-4 times faster than DASSL.

The work-precision curves for the ESDIRK solvers settle at a constant level in the low accuracy range instead of continuing the linear trend found for high accuracies. Moreover, the behavior in this range is more erratic. This can be partly attributed to the error and convergence controller. Consider, for example, ESDIRK45. An input tolerance level of $atol = rtol = 10^{-1}$ gives better than expected results (SCD = 2), but this comes at the cost of increased computation time. Inspection shows that the step size is limited by convergence in the nonlinear solver and not by the local error. The relatively large step sizes allowed by the error controller lead to convergence failures in the nonlinear solver, which then forces a step size reduction. This shows that ODE error control devices perform best when operating at low tolerance levels.

Comparing the results for $N = 25$ and $N = 100$ shows that all solvers need more time when the integration is interrupted frequently. The BDF methods have the largest restart overhead because, when restarted, they revert to first order requiring small time steps, and slowly build up higher order information.

Both DASSL and LSODE manage to integrate across the phase changes. Inspection of the process shows, however, that both methods experience a high number of step failures, and lower their order before successfully stepping across. The loss in efficiency associated with these step failures alone is difficult to isolate but is reflected in the results shown in Figure 5.10.

The differences in performance are relatively small when using only 25 subintervals. The advantage of one-step methods over multi-step methods is, however, clearly observed when the number of subintervals is increased, the difference between DASSL and the ESDIRK solvers being the most notable.

Figure 5.10 also shows that none of the solvers are very sensitive to the required accuracy. Although with some irregularities in the low accuracy range, the computational cost increases linearly with the required accuracy in the solution.

5.6 Discussion

The work presented in this paper addresses time integration of reactive, compositional, and thermal porous media processes, and focusses in particular on the design of specialized solvers for integration of stiff chemical kinetics subject to phase equilibrium constraints.

To facilitate the algorithmic development we constructed a virtual kinetic cell. The VKC allows us to study the kinetics and phase behavior of reactive transport processes in an isolated setting. Through user prescribed inflow and

outflow boundary conditions, interactions with the reservoir can be studied. Two ISC reaction models with 6 and 14 components, respectively, were implemented and tested. The VKC was demonstrated with a ramped temperature experiment using the 6-component model. Ramped temperature experiments are routinely carried out in the laboratory. In future work we will validate the simulation results against experimental data. Although not explored in this work, the VKC can also be applied to help determine optimal experimental conditions in the design phase. For example, parametric sensitivity studies can be used to determine regions of the parameter space where additional laboratory experiments should be carried out. A more rigorous approach involves optimal model based design, where the experimental conditions (such as oxygen flow rate and concentration in ramped temperature kinetic cell experiments) are optimized in an iterative loop. The optimality criterion is then related to the statistical quality of the parameter estimates that results from using the experimental data to estimate model parameters. Optimal experimental design is explored in e.g. Bauer et al. (2000).

Because of the stiff chemical kinetics, the low to medium accuracy required in the solution, and the short integration intervals experienced in an operator splitting environment, we selected the class of ESDIRK methods for the temporal integration of the chemical reactions. To increase computational efficiency, we select the time step size with a predictive controller for the local integration error, and generate starting guesses for the modified Newton iterations using continuous extensions of the ESDIRK methods. Performance comparisons between the ESDIRK solvers and the popular stiff ODE solvers DASSL and LSODE, show that the higher order ESDIRK solvers are at least comparable if not superior in terms of computational speed, especially over the relatively short integration intervals that are generally required in an operator splitting environment. If we aim for two to four correct digits in the solution, which we expect to be of practical interest in ISC simulations, the low and medium order ESDIRK methods (ESDIRK12, ESDIRK23 and ESDIRK34) are two times faster than LSODE and three or four times faster than DASSL. Apart from the ESDIRK methods, other classes of integration methods could be of interest, such as the Rosenbrock methods (Sandu, Verwer, Loon, Carmichael, Potra, Dabdub and Seinfeld, 1997; Sandu, Verwer, Bloom, Spee, Carmichael and Potra, 1997), which we will consider in future work.

We extended the ESDIRK methods to handle the discontinuities that arise due to phase changes. Phase changes are detected by monitoring sign changes of special event functions. The proposed algorithm proved robust in detecting and locating phase changes, and lowered the number of convergence and error test failures by more than 50%. The DASSL and LSODE solvers that are not equipped with a phase change algorithm will, in most cases, successfully integrate across the change after repeated step size reductions caused by convergence and error test failures. Overall efficiency gains from using the phase change algorithm when measured over a long integration interval with only one

or two phase changes occurring are modest, but the improved robustness near phase boundaries is certainly valuable.

The VKC model uses a simplified constant K-value phase equilibrium description. We are currently working on the extension to full equation-of-state based phase equilibrium. In a rigorous flash algorithm the phase state depends on the outcome of a stability analysis which cannot be expressed in closed form and, hence, does not directly fit into the framework of event functions. For transitions from a two-phase region to a single phase region, we can still detect changes by monitoring phase fractions. In the reverse situation the problem is now more complicated. In principle, this would require a stability analysis to be performed each time conditions change to check if the new single phase state is unstable. A possible solution is to exploit shadow regions as in Rasmussen et al. (2006) to speed up flash calculations, which will reduce the number of stability analyses required.

5.7 Conclusions

The main conclusions of this work are:

- The virtual kinetic cell (VKC) is a novel and useful tool for analyzing kinetics and phase behavior in reactive, compositional, and thermal processes. It can provide simulation support for laboratory kinetic cell experiments, and be used for studying interactions between kinetics and phase behavior as well as interactions with the reservoir through specialized boundary conditions.
- ESDIRK methods are well-suited for integration of the stiff kinetics due to their strong stability properties. In particular, when implemented in an operator splitting environment, the ESDIRK methods outperform stiff multi-step methods. Experiments show that the methods lead to 50–75% reductions in computational costs compared to multi-step methods.
- Phase change detection using a discrete event system approach is an attractive tool which significantly reduces integration step failures and therefore computational time.

Acknowledgements

The authors would like to thank Norman Freitag, Saskatchewan Research Council, Canada, for generously providing detailed reaction kinetic data for the SARA based reaction model.

Paper II

Morten R. Kristensen, Margot G. Gerritsen, Per G. Thomsen,
Michael L. Michelsen and Erling H. Stenby:

An Equation-of-State Compositional In-Situ Combustion Model: A Study of Phase Behavior Sensitivity

Submitted to *Transport in Porous Media*, 2008.

Chapter 6

An equation-of-state compositional in-situ combustion model

Abstract:
To facilitate the study of reactive-compositional porous media processes we develop a virtual kinetic cell (single-cell model) as well as a vitual combustion tube (one-dimensional model). Both models are fully compositional based on an equation of state. We employ the models to study phase behavior sensitivity for in-situ combustion, a thermal oil recovery process.

For the one-dimensional model we first study the sensitivity to numerical discretization errors and provide grid density guidelines for proper resolution of in-situ combustion behavior. A critical condition for success of in-situ combustion processes is the formation and sustained propagation of a high-temperature combustion front. Using the models developed we study the impact of phase behavior on ignition/extinction dynamics as a function of the operating conditions. We show that when operating close to ignition/extinction branches, a change of phase behavior model will shift the system from a state of ignition to a state of extinction or vice versa. For both the rigorous equation of state based and a simplified, but commonly used, K-value based phase behavior description we identify areas of operating conditions which lead to ignition. For a particular oil we show that the simplified approach overestimates the required air injection rate for sustained front propagation by 17% compared to the equation of state based approach.

Keywords: Reactive transport processes, compositional processes, phase behavior, multi-scale methods, enhanced oil recovery, in-situ combustion

6.1 Introduction

Multi-component, multi-phase reactive porous media processes are critical to a wide range of field applications including contaminant transport, enhanced oil recovery and geologic CO_2 sequestration. One such application is in-situ combustion (ISC), also known as fire flooding or high pressure air injection. ISC is an effective way to enhance the recovery of oils that are difficult to produce, such as heavy oils, and is receiving strong new interest in the petroleum industry due to the vast heavy oil reserves and rapid decline in conventional, easier-to-produce reserves (Prats, 1986; Castanier and Brigham, 2004). Air injected into the reservoir oxidizes a small portion of the oil, which raises the temperature in the reservoir sufficiently to form steam, reduce the viscosity of the oil and thus allow for improved oil production. ISC is also attractive because the production process is much cleaner than the common methods of steam injection, or steam assisted gravity drainage, which require large amounts of gas to be burned in order to produce the steam. Its use is currently not widespread, partly because of difficulties in accurately predicting ISC performance through numerical simulation. One reason why such processes are challenging to simulate accurately is that the temporal and spatial scales of the important physical sub-processes in these systems vary widely. For example, scales associated with advection or heat conduction are typically much larger than those governing chemical reactions, which in turn are considered larger than the scales associated with the transfer of components between phases. The multi-scale character requires the formulation of sub-grid scale models in numerical simulations. This coarse graining, or upscaling, is far from trivial for sub-processes with very small spatial or temporal extent, such as the combustion kinetics in ISC. The physical sub-processes are also strongly nonlinearly coupled. This coupling is strengthened by the thermodynamic equilibrium conditions that govern phase behavior. Because of the nonlinearity, numerical solutions are very sensitive to modeling errors as well as numerical errors. Figure 6.3, which shows the convergence history of a one-dimensional combustion experiment, illustrates this sensitivity. Only at fine temporal and spatial grid step sizes the impacts of numerical and modeling errors are reduced sufficiently to give reasonable predictions of combustion front speed and reservoir temperature. In practical settings, this number is computationally intractable.

To increase solver accuracy and robustness for multi-phase reactive porous media processes in general, and ISC processes in particular, we seek to improve our understanding of the interplay between upscaling techniques, mathematical models and numerical algorithms. In previous work (Kristensen et al., 2007*b*,*a*) we presented tailored integration methods for stiff kinetics along with algorithms for robust handling of phase changes, which we tested using a Virtual Kinetic Cell (VKC). In this paper we extend our study to the influence of phase behavior treatment on kinetics and on performance predictions. Compositional effects and their impact on reaction paths, and hence on overall process per-

formance, are not fully understood for processes like ISC. There are two main reasons why we expect kinetics and performance prediction to be sensitive to phase behavior models. First, chemical reactions in ISC processes are assumed to be heterogeneous gas-liquid or gas-solid reactions, where reaction rates depend on phase component concentrations, which are sensitive to phase behavior. Second, in ISC processes a limited number of pseudo-components is used to represent the very large number of liquid and gas components in reservoir settings. The pseudoization is generally driven by the kinetics, not the phase behavior. For example, a pseudo-component may be used to model kinetically similar hydrocarbons with widely varying boiling points. Reliable phase behavior models are therefore difficult to develop, and it is natural to expect sensitivities to the chosen formulation. We again use the VKC to study this interaction between phase behavior and kinetics, as well as a novel one-dimensional, in-house ISC simulator, which we refer to as the Virtual Combustion Tube (VCT). Both the VKC and the VCT are equipped with a family of phase behavior models, including a Peng-Robinson equation of state (Peng and Robinson, 1976), and two types of equilibrium K-value correlations described in Section 6.2.3.

More specifically, the main contributions of this work are:

- We develop a one-dimensional combustion tube model (VCT). The VCT is fully compositional with a dual strategy for describing the phase behavior, using either equilibrium K-value correlations or the Peng-Robinson Equation of State (EoS). The VCT is the first EoS based ISC simulator published in the literature. As in the VKC, two reaction models are implemented: the so-called minimal model, used in STARS and most commercial applications, and the more involved SARA fractions model, suggested by e.g. Freitag and Verkoczy (2005). The VCT and the VKC provide a flexible platform for the study of laboratory scale combustion experiments.

- We perform extensive grid sensitivity tests on the VCT to better understand the grid dependency of ISC simulations. The test results are used to guide the selection of grid step sizes to ensure reliable, grid independent, numerical solutions.

- We investigate the interaction between kinetics and phase behavior models using both the VKC and the VCT. In particular, we analyze ignition/extinction phenomena, and show that in certain operation regimes the choice of phase behavior model will critically change the reaction dynamics and the performance of the ISC process.

The published work on ISC processes is limited in its extent, but important recent work in this area has been done by various authors including Akkutlu and Yortsos (2003), who focus on analytical techniques and analyze ISC problems where the combustion zone is treated as a discontinuous front. On the numerical side, we note the existence of STARS (CMG, 2004), the most commonly used thermal simulator in the oil industry. To properly resolve the fine

scale behavior of ISC reaction zones, both Christensen et al. (2004) and Nilsson et al. (2005) have developed adaptive gridding techniques. Temporal adaptivity was addressed by Younis and Gerritsen (2006), who proposed a framework for integration of ISC processes based on operator splitting techniques, and by Kristensen et al. (2007*b*), who developed a class of efficient integration methods for ISC kinetics. On the experimental side, the ISC literature is richer, recent contributions including the work by e.g. Moore et al. (1999) and Christofari et al. (2006).

The paper is organized as follows. Section 6.2 reviews the ISC process and introduces the reaction and phase behavior models used in this paper. The combustion tube model is presented in Section 6.3. Section 6.4 discusses the numerical solution of the model and presents a convergence study along with simulation comparisons with the commercial code STARS. The ignition/extinction experiments and analyses of phase behavior sensitivity are presented in Section 6.5.

6.2 Models for chemical reactions and phase behavior in ISC

6.2.1 The in-situ combustion process

ISC is the process of injecting air into an oil reservoir to oxidize a small fraction of the hydrocarbons present. Figure 6.1 gives a schematic representation of characteristic temperature and saturation zones in ISC (Prats, 1986). A slow moving combustion front is propagated by a continuous flow of air. In the combustion zone injected oxygen reacts with residual hydrocarbons gener-

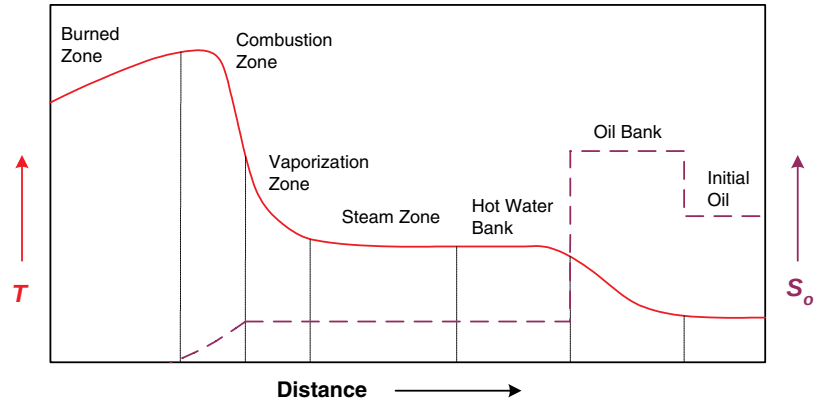

Figure 6.1: Schematic representation of characteristic temperature and saturation distributions in forward in-situ combustion (adapted from Prats (1986), not to scale).

ating carbon oxides and water, and producing heat. Hydrocarbons contacted by the leading edge of the high-temperature zone undergo thermal cracking and vaporization. Mobilized light components are transported downstream where they mix with the original crude. The heavy residue, which is normally referred to as coke, is deposited on the core matrix and is the main fuel source for the combustion. Downstream of the combustion zone is the steam plateau which is formed from water of combustion and vaporization of formation water. The leading edge of this plateau is the primary area of oil mobilization.

Thermal conduction allows heat to sweep areas of the reservoir not directly contacted by hot fluid. For heavy oils, the recovery efficiency is substantially improved because of the dramatic reduction of the viscosity of heavy oils with temperature. But, ISC is applicable to lighter oils as well because it also promotes production through flue-gas drive, thermal expansion, steam and water drive, and vaporization of lighter oils (Gillham et al., 1997; Clara et al., 2000). ISC can recover oil economically from a variety of reservoir settings. For further discussion of the process we refer to Prats (1986) and Castanier and Brigham (2004).

The efficiency of ISC depends critically on the process reaching ignition conditions and operating in a high-temperature oxidation regime. ISC projects may fail if insufficient air is injected, or if insufficient heat is supplied during ignition. Unlike other enhanced oil recovery methods, such as gas injection, small changes to the operating conditions may change the system dynamics dramatically. When designing ISC projects it is therefore of key importance to be able to predict the ignition/extinction behavior of the process.

6.2.2 Reaction models

A typical crude oil is a complex mixture of hundreds of different chemical species. In all reservoir simulation models the oil is lumped into a limited set of (pseudo) components. Likewise, in reactive processes, such as ISC, the chemical reactions are generally lumped together in a limited set of empirically derived equations. For purely compositional models, the process of lumping (pseudoization) is carried out so that the pressure-volume-temperature (PVT) behavior of the resulting set of pseudo components resembles the behavior of the actual oil as closely as possible, the inherent trade-off being to minimize the number of components (for computational speed), while retaining accuracy in the EoS calculations. For reactive processes, the oil is typically lumped based on reactivity with little emphasis on PVT behavior. We are not aware of any published work in the area of pseudoization for reactive-compositional processes, which takes into account both PVT behavior and reactivity. In this paper we use two different component and associated reaction models, both of which are derived primarily to represent the chemical reaction behavior of the oil. The first model includes a minimal realistic set of components and reactions to represent ISC behavior. We refer to this model as the *minimal model*. The components in the model are light

oil, heavy oil, coke, oxygen, water and inert gas. The reactions include direct oxidation of the light and heavy oil, cracking of heavy oil into light oil and coke, and, finally, oxidation of coke. This minimal model is the common model used in many ISC simulations and it is the default model available in STARS. The oil is in the medium range with an API gravity of 25.

The *SARA model* is based on lumping the oil into its SARA (Saturates, Aromatics, Resins and Asphaltenes) fractions. The model we consider in this work contains 14 pseudo components and 14 reactions. Details of this model can be found in Freitag and Verkoczy (2005), Freitag and Exelby (2006) and Ren et al. (2005). The reactions include pyrolysis, low-temperature oxidation (LTO) and high-temperature oxidation (HTO) of the SARA fractions along with HTO of partially oxidized LTO residue and the coke formed by pyrolysis. The API gravity of the particular oil we are using for the SARA model, and for which we present results in the following sections, is 16. The reactions for both models are listed in Section 6.8.

6.2.3 Phase behavior models

Previously published ISC models (Crookston et al., 1979; Grabowski et al., 1979; Coats, 1980) and current industry standard simulators (CMG, 2004) all take an equilibrium K-value based approach to phase behavior, in which the K-values depend only on temperature and pressure. For example, for components distributing between the oil and gas phases, the equilibrium phase compositions, x_i^g and x_i^o, are related by

$$\frac{x_i^g}{x_i^o} = K_i = K_i(T, P), \tag{6.1}$$

where K_i is obtained from a table or a correlation, such as Wilson's correlation (Michelsen and Mollerup, 2004). We will refer to this approach as the *K-value based approach*.

For the K-values we use two different approaches in this work. In the first approach the K-values are obtained from the Wilson correlation (see Section 6.10) and in the second approach they are tuned to the EoS, meaning that they are obtained from pre-calculated tables generated from EoS flashes of the initial oil at varying pressure and temperature. Tabulation of K-values is commonly done when working with commercial simulators. During simulation K-values are then obtained by linear interpolation in the tables. We will refer to the second approach as *optimized K-values*.

In the EoS based approach we use the Peng-Robinson (PR) equation (Peng and Robinson, 1976). The equilibrium phase compositions are obtained by solving the conditions for phase equilibrium: the equility between chemical potentials of a component in all phases. The pseudoization procedure for the Peng-Robinson EoS is based on Whitson's method (Whitson and Brule, 2000).

The lumping of the oil into pseudo components is pre-determined by the components in the reaction models. In Whitson's method critical temperatures and pressures and binary interaction coefficients are estimated from Twu's correlations (Twu, 1984), and the accentric factors are estimated from the Lee-Kesler correlations (Lee and Kesler, 1975). We use critical data obtained in this way for all (fluid phase) pseudo components, and for actual chemical components, such as oxygen and nitrogen, we use literature data.

The obvious advantage of the K-value based approach is the savings in computing time when avoiding the rigorous equilibrium calculation. A possible disadvantage is, however, that the composition dependence of the K-values is neglected, and, hence, that the predicted phase behavior may be inaccurate, especially in near-critical regions. A change in phase behavior will affect the kinetics, which, in turn, will affect the heat released and combustion gases evolved. To explore the importance of accurate phase behavior representation, we develop in the next section a full EoS compositional ISC model.

6.3 A virtual laboratory for reactive porous media processes

In this section we present the governing equations for thermal, compositional and reactive porous media flow. We state the equations in a general form and give details on the constitutive models in the appendix. By ignoring spatial dependencies, thus only looking at the temporal behavior, we then reduce the equations and obtain the model for the kinetic cell.

6.3.1 A Virtual Combustion Tube (VCT)

We model a porous media system containing n_c chemical components distributed among three mobile fluid phases (oil, water, and gas) and one immobile solid phase. Components existing in the solid phase are assumed to do so exclusively. The mobile components are assumed to exist in at most two phases, with the water component partitioning into the water and gas phases, and the remaining components partitioning into the oil and gas phases. The chemical components are indexed as

$$i \in \mathcal{I} = \mathcal{I}^{ol} \cup \mathcal{I}^{w} \cup \mathcal{I}^{s}, \tag{6.2}$$

where

$$\begin{aligned} \mathcal{I}^{ol} &= \{1, \ldots, n_{ol}\}, \\ \mathcal{I}^{w} &= \{n_{ol} + 1\}, \\ \mathcal{I}^{s} &= \{n_c - n_s + 1, \ldots, n_c\}. \end{aligned} \tag{6.3}$$

Thus, the total number of components is $n_c = n_{ol} + n_s + 1$.

Governing equations

Let the porous medium be represented by Ω with boundary $\mathcal{S}$, then the governing equations for ISC can be derived from n_c component conservation equations, an energy conservation equation, and a volume conservation equation. The i-th component conservation equation can be written in integral form as

$$\frac{d}{dt}\int_\Omega C_i d\Omega + \int_\mathcal{S} \mathbf{q}_i^m \cdot \mathbf{n} d\mathcal{S} = \int_\Omega \left(Q_i^{m,reac} + Q_i^{m,well}\right) d\Omega, \tag{6.4}$$

where $i \in \mathcal{I}$, C_i is the total concentration of component i per bulk volume, $\mathbf{q}_i^m$ is the mass flux, and $Q_i^{m,reac}$ and $Q_i^{m,well}$ are the mass source densities due to chemical reactions and wells, respectively. We note that

$$\mathbf{q}_i^m = \mathbf{0}, \qquad i \in \mathcal{I}^s. \tag{6.5}$$

Neglecting capillary forces, we can express the component flux term in (6.4) using the standard multi-phase extension of Darcy's law

$$\mathbf{u}^j = -\frac{k_r^j}{\mu^j}\mathbf{k}\left(\nabla P - \rho^j g \nabla D\right), \tag{6.6}$$

where $\mathbf{u}^j$ is the phase flow velocity, $\mathbf{k}$ is the absolute permeability, k_r^j is the relative permeability, μ^j is the viscosity, ρ^j is the mass density, g is the gravitational constant, and D is the reservoir depth. The total component flux is the sum of the fluxes in the individual phases, given by

$$\mathbf{q}_i^m = \sum_j x_i^j \xi^j \mathbf{u}^j, \tag{6.7}$$

where $j \in \{o, g\}$ for $i \in \mathcal{I}^{ol}$, and $j \in \{w, g\}$ for $i \in \mathcal{I}^w$. x_i^j are the mole fractions of components i in phase j, and ξ^j the molar densities of phase j.

The energy conservation equation is

$$\frac{d}{dt}\int_\Omega U d\Omega + \int_\mathcal{S} \left(\mathbf{q}^{h,adv} + \mathbf{q}^{h,cond}\right) \cdot \mathbf{n} d\mathcal{S} = \int_\Omega \left(Q^{h,reac} + Q^{h,well}\right) d\Omega, \tag{6.8}$$

where U is the total internal energy of the system, $\mathbf{q}^{h,adv}$ is the heat transport due to advection, $\mathbf{q}^{h,cond}$ is the heat transport due to conduction, and $Q^{h,reac}$ and $Q^{h,well}$ are the heat source densities due to chemical reactions and wells, respectively. The advective heat transport is the sum of the heat carried by each mobile phase

$$\mathbf{q}^{h,adv} = \sum_j \xi^j \mathbf{u}^j h^j, \tag{6.9}$$

where h^j is the molar enthalpy. Fourier's law is used to express the transport due to conduction

$$\mathbf{q}^{h,cond} = -\mathbf{k}_c \nabla T, \tag{6.10}$$

where the tensorial quantity $\mathbf{k}_c$ is the effective thermal conductivity of the saturated medium.

Finally, the principle of volume conservation expresses that the fluid and solid phases must fill the pore space exactly

$$V_p = \sum_j V^j, \tag{6.11}$$

where V_p is the void pore volume and V^j is the volume of phase j for $j \in \{o, w, g, s\}$.

Phase equilibrium

In addition to the conservation requirements, we assume that the system is in thermodynamic equilibrium as expressed by the equality between chemical potentials, or equivalently fagacities, of a component in all phases. For components partitioning between the oil and gas phases we have

$$f_i^o = f_i^g, \qquad i \in \mathcal{I}^{ol}, \tag{6.12}$$

where f_i^j is the fugacity of component i in phase j. Details on modeling fugacities along with models for chemical reactions, wells and rock and fluid properties are given in Section 6.10. We assume that the partitioning of the water component between the gas and water phases can be modeled using a simple K-value correlation.

6.3.2 A Virtual Kinetic Cell (VKC)

The Virtual Kinetic Cell (VKC) was developed in Kristensen et al. (2007*b*) and further extended in Kristensen et al. (2007*a*). The VKC is essentially a zero-dimensional version of the above developed model, which allows us to study kinetics and phase behavior in an isolated setting. Adopting the above notation we can write the VKC in the form

$$\frac{dC_i}{dt} = Q_i^{m,reac} + Q_i^{m,well}, \qquad i \in \mathcal{I}, \tag{6.13a}$$

$$\frac{dU}{dt} = Q^{h,reac} + Q^{h,well}, \tag{6.13b}$$

$$0 = V_p - \sum_j V^j, \tag{6.13c}$$

$$0 = f_i^g - f_i^o, \qquad i \in \mathcal{I}^{ol}. \tag{6.13d}$$

6.4 Numerical model for the VCT

In this section we discuss briefly the numerical model for the VCT. Details can be found in Section 6.9 for completeness. The numerical model for the VKC

was presented in Kristensen et al. (2007*b*). For the VKC we developed specialized solvers for the stiff kinetics based on the ESDIRK subclass of Runge-Kutta methods (Butcher and Chen, 2000; Kværnø, 2004). We further extended the solvers with a phase change detection algorithm for robust handling of the discontinuities that occur due to phase changes. The specialized solvers for kinetics are part of our ongoing efforts to develop a full operator splitting based integration scheme for the ISC equations, in which physical subprocesses, such as reaction and transport, are integrated by tailored methods (Younis and Gerritsen, 2006).

6.4.1 Choice of variables

We use the n_c mass balances (6.4) and the energy balance (6.8) as primary equations, and as variables we choose the n_c overall component concentrations, C_i, and temperature and pressure. The advantage of working with overall quantities as variables, as opposed to intensive variables such as mole fractions and saturations, is that we avoid the switching of variables in implicit methods associated with phase disappearance/reappearance. For thermal-compositional models the thermodynamic state (intensive and extensive) of a system is uniquely described in terms of $n_c + 1$ independent primary variables. For convenience, we work with the full set of component concentrations and include the volume constraint (6.11) as an additional equation. Thus, we solve simultaneously a set of $n_c + 2$ equations per gridblock, where temperature is aligned with the energy balance, pressure is aligned with the volume constraint, and the component concentrations are aligned with the respective component balances. For the purpose of the work presented in this paper we are concerned more with robustness than computational efficiency, but we note that the volume constraint and component balances for all immobile solid components can be eliminated from the primary equation set, since both types of equations are local to each gridblock.

6.4.2 Discretization

The governing equations for the VCT are discretized using a control-volume approach on a block-centered Cartesian grid with standard two-point flux approximations. For stability reasons, the time discretization is performed using the backward Euler scheme treating all flow, well and reaction terms implicitly. This fully implicit, control-volume based scheme is common in reservoir simulation, and it is also implemented in the STARS simulator (CMG, 2004), which allows us to validate our code with this commercial code.

The discretized equations comprise a set of nonlinear algebraic equations, which are solved by Newton-Raphson iterations. We perform exact flash calculations in each Newton-Raphson iteration step.

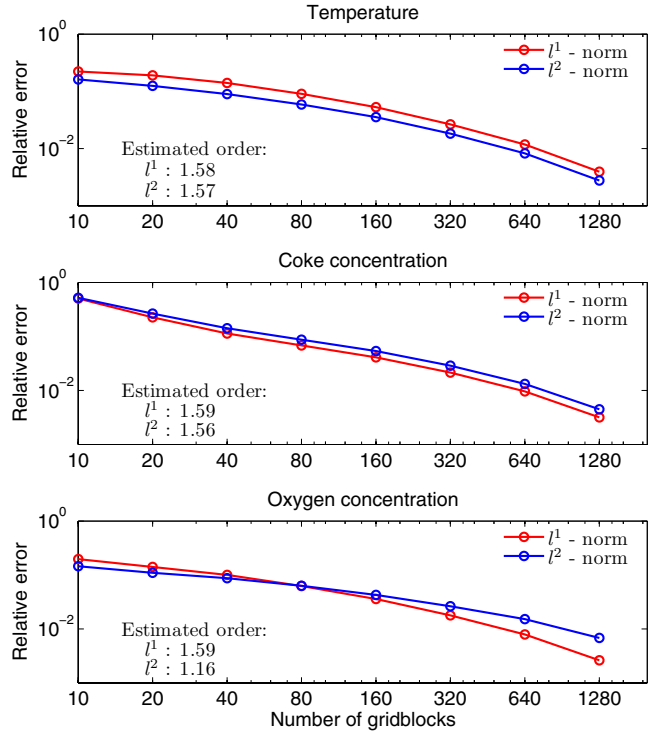

Figure 6.2: Estimated relative error in temperature, coke concentration, and oxygen concentration as a function of the number of gridblocks.

6.4.3 Timestepping

We use the timestep formula due to Aziz and Settari (1979) given by

$$\Delta t^{n+1} = \Delta t^n \min_{i,k} \left[\frac{(1+\lambda)\,\Delta u_{ik}^n}{\Delta u_i^* + \lambda \Delta u_{ik}^n} \right], \tag{6.14}$$

where Δu_{ik}^n is the change in variable i in gridblock k over the previous timestep, Δu_i^* is the target change, and λ is a tuning factor. For the simulations presented in this paper we use $\Delta P^* = 1\,\text{atm}$, $\Delta T^* = 5\,\text{K}$, $\Delta z_i^* = 0.05$ and $\lambda = 0.75$, where $z_i = C_i / \sum_i C_i$ is the overall mole fraction of component i.

6.4.4 Grid sensitivity study

In order to validate our implementation we carry out spatial and temporal grid convergence studies and perform careful comparisons with STARS. We simulate a laboratory dry air combustion tube test using the minimal reaction model. Air is injected at a rate of $0.016\,\mathrm{m^3/hr}$ into an oil saturated core, which is preheated to 311 K. During the first 30 minutes of simulation the injection end is heated by a constant energy input of $211\,\mathrm{kJ/hr}$, which establishes a combustion front. We refer to Kristensen (2008) for a complete list of input parameters for the simulation. We simulate the system until $t^* = 8$ hrs using the time step strategy outlined above. The simulation is repeated for varying grid densities using $N_{blk} = 10 \cdot 2^n$, $n = 0, 1, \ldots, 7$, and compared to a reference solution generated using $N_{blk} = 2560$. The error is measured as

$$e_p = \frac{\|\mathbf{u}(t^*) - \mathbf{u}^{ref}(t^*)\|_p}{\|\mathbf{u}^{ref}(t^*)\|_p}, \qquad p = 1, 2. \tag{6.15}$$

Figure 6.2 shows the errors (6.15) as a function of grid density for three of the key variables: temperature, coke concentration and oxygen concentration. The estimated asymptotic convergence rates are indicated in the figure. To illustrate the grid sensitivity of the solution, the corresponding temperature, coke and oxygen profiles are plotted in Figure 6.3. Super-linear convergence is observed in all variables and in both norms. In order to reduce the error to, say, 5% we observe that approximately 160 gridblocks are required. At coarse grids the smoothing of temperature leads to excessive coke formation, which affects the combustion front propagation. Using 80 gridblocks, the location of the combustion front is underestimated by almost 20% compared to the converged result. With the ignition heater settings used in these simulations, a combustion front is established at all grid densities, but the front propagation speed varies dramatically. The oil recovery is affected both in terms of rate of recovery and ultimate recovery, because at coarse grids a larger fraction of the oil is burned as shown in Figure 6.4.

The above convergence study was carried out using the K-value option for phase behavior. We have carried out an additional study using the EoS option, which indicated similar observations and convergence rates. In general, the number of gridblocks required to reduce the error below a certain threshold accuracy will be process and oil dependent.

6.4.5 Comparison with STARS

To further validate the VCT we compare our simulation results with results obtained using STARS. As above, we simulate dry air injection into an oil saturated core. Comparisons are shown in Figure 6.5 using 200 gridblocks in both simulators. Care was taken to make sure that all input data, treatment of

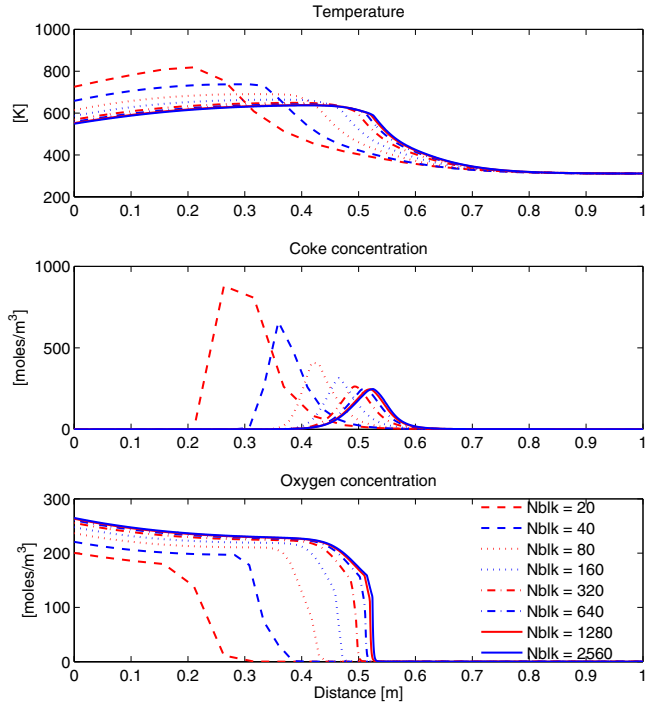

Figure 6.3: Temperature, coke concentration, and oxygen concentration profiles at different grid densities for the combustion tube simulation.

boundary conditions, and numerical settings were the same in both simulations. However, with limited implementational details available for STARS, some differences may still exist. In general, good agreement is observed, and together with the convergence study we take this as sufficient validation of the VCT.

6.5 Ignition/extinction dynamics

For optimum performance we are interested in operating ISC processes at conditions corresponding to combustion in a high temperature regime, where full oxidation reactions take place. For a simplified 1D problem Akkutlu and Yortsos (2003) have shown the existence of multiple (pseudo) steady states in terms of combustion front temperature as a function of the air injection rate and heat loss rate. When operating near ignition/extinction branches it is likely that the system behavior will be very sensitive to the phase behavior model. In this

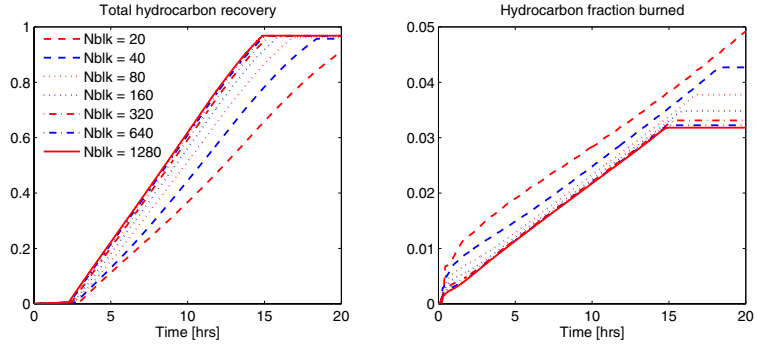

Figure 6.4: Cumulative oil recovery and fraction of oil burned at different grid densities for the combustion tube simulation.

section we carry out simulation studies with both the VKC and the VCT to explore the impact of phase behavior on ignition/extinction dynamics.

6.5.1 Kinetic cell experiments

Kinetic cell experiments are routinely carried out in the laboratory, typically as ramped temperature experiments, where an oil sample placed in the cell is heated, while air is circulated through the cell. Since the kinetic cell is a batch-type experiment, the steady state always corresponds to all the oil being consumed and only the injection gas left in the cell. The paths taken to reach the steady state can be very different. In the simulations discussed below we heat up the cell to a specified temperature, and then keep a constant cooling temperature at this level. The cell heat controller is modeled as

$$Q^{h,htr} = -u_a \left(T - T^{ext}\right), \tag{6.16}$$

where u_a is a heat transfer coefficient (controller gain) and T^{ext} is the external heating/cooling temperature (controller set point). We define ignition as the state, where sufficient heat is evolved from reactions to increase the cell temperature above a threshold temperature as illustrated in Figure 6.6. The ignition/extinction behavior of the system, as defined in this way, is then studied as a function of air injection rate and heat loss rate (u_a). The ignition regime is the area of the parameter space, where the maximum temperature during a simulation is above the threshold temperature. The boundary of the regime corresponds to a level curve for the maximum temperature (where the maximum temperature is equal to the threshold temperature), and we will refer to this curve as an ignition/extinction curve.

We solve the continuation problem in the two parameters (air injection rate and heat loss rate) and map out the ignition/extinction regimes for both the

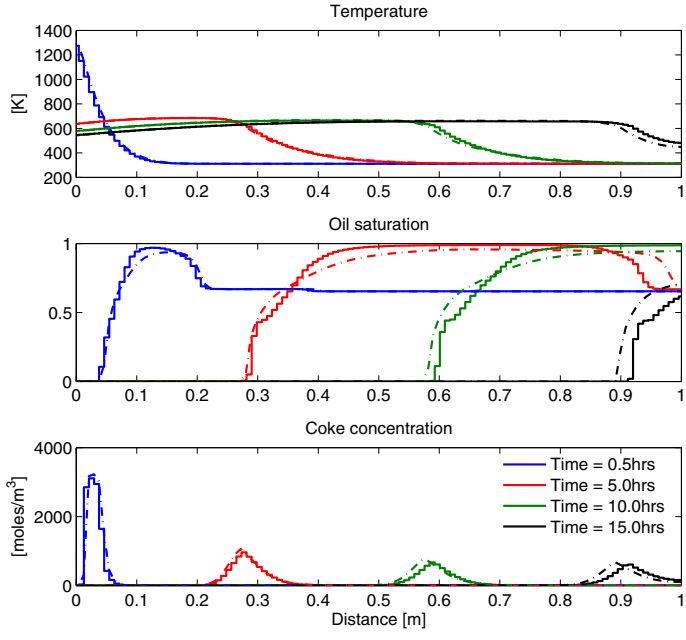

Figure 6.5: Simulation comparison between the VCT and the commercial simulator STARS. Temperature, oil saturation, and coke concentration profiles are shown. Solid lines : STARS, dashed lines : VCT.

minimal and the SARA reaction models, and using both K-value based and EoS based phase behavior descriptions. In both phase behavior approaches we use the same property models (phase densities, enthalpies, etc.), as outlined in Section 6.10, and make sure that the numerical solution is converged, so that the differences observed reflect only differences in phase behavior treatment. We refer to Kristensen (2008) for a complete list of input parameters for the simulations.

We consider first the minimal reaction model. Figure 6.7 shows the ignition/extinction regimes for the EoS and K-value approaches, respectively, using a heat controller temperature of 473 K and a threshold temperature of 500 K. At low air flow rates combustion is not sustained, whereas at high air rates the oil components are stripped from the oil phase before they react. Intermediate flow rates lead to ignition when the heat loss rate is sufficiently low. Increasing the heat loss rate leads to extinction. At the lower part of the ignition regime the phase behavior approaches predict similar behavior. Figure 6.8 shows ignition/extinction regimes for the SARA reaction model. In this case, the heat

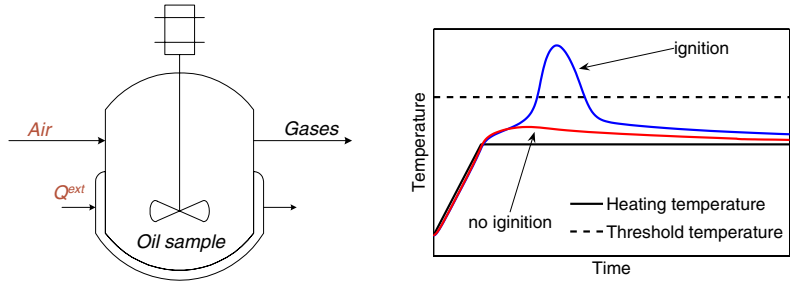

(a) Kinetic cell. (b) Definition of ignition.

Figure 6.6: The VKC is modeled as a batch-type reactor, but with continuous flow of air. Ignition is defined as the state, where the onset of combustion in a ramped temperature experiment releases enough heat to increase the cell temperature above a certain threshold temperature.

controller temperature is 573 K and the threshold temperature 650 K. For both reaction models we have carried out sensitivity studies to assess the dependence on the choice of threshold temperature. In general, only small variations are observed, and only on the lower part of the ignition regime, when the threshold temperature is varied ±50 K. Hence, the conclusions drawn from Figure 6.7 and 6.8 are independent of threshold temperature.

The K-value approaches are based on an ideal assumption of composition independent K-values, which is generally valid away from critical regions. When increasing the air flow rate, the pressure in the cell increases significantly above the initial pressure. A probable explanation for the differences in ignition regimes observed at higher air rates is therefore the increased pressure which leads to less ideal conditions. The Wilson correlation is a generalization of Raoult's law. Since the correlation extends the pure component vapour pressure curves beyond their critical temperature, it tends to overestimate the size of the two-phase region. For both the minimal and the SARA reaction models we observe an extended region of ignition when using Wilson K-values. Since oil components are assumed only to react in the oil phase, underestimation of oil volatility will lead to ignition for a wider range of operating conditions. Thus, our results agree with the expected behavior of the Wilson K-values.

The range of air injection rates typically used in laboratory kinetic cell experiments is 1 to 30 standard cell volumes per minute. The range covered in Figures 6.7 and 6.8 is approximately 0.1 to 100 standard cell volumes per minute (the cell volume is 1 L), so the sensitivities observed occur in the practical range of operating conditions.

Tabulation of K-values optimized to an EoS is the common approach when working with commercial simulators for ISC. Hence, in subsequent sections we

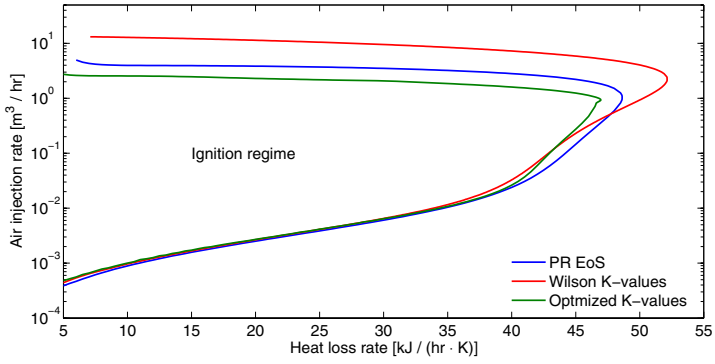

Figure 6.7: Ignition/extinction regimes for the minimal reaction model using the VKC. Comparison is made between EoS based and K-value based phase behavior representations.

will focus on the comparison of optimized K-values with the full EoS.

6.5.2 One-dimensional combustion tube experiments

Kinetic cell experiments do not reflect the quantitative behavior of one-dimensional ISC tube tests. In order to properly translate the observed phase behavior sensitivity to actual ISC processes involving the coupling of flow, transport and reactions, we need to carry out ignition/extinction experiments using the combustion tube model. Ultimately, we are interested in the effect of phase behavior treatment in ISC processes on displacement efficiency, and thereby on the total recovery. Ideally, by extending to multi-dimensional problems, we will be able to assess the effect of phase behavior sensitivity on actual field ISC processes. We prefer, however, a step-wise approach, where the model is gradually extended, which allows us to carefully study the behavior at each stage and isolate the important parts.

We consider a dry air VCT experiment similar to the experiment described in Section 6.4.4. Air is injected into an oil saturated core, which is preheated to 311 K. The injection end is heated for the first half hour of the simulation by a constant rate energy input. We study the ignition/extinction behavior as a function of air injection rate when varying the phase behavior model. We simulate the system for 10 hrs and measure the front temperature as the maximum temperature in the system at the end of the simulation. For an ignition heater rate of 70 $^{\mathrm{kJ}}/_{\mathrm{hr}}$, Figure 6.9(a) shows the front temperature as a function of air injection rate. Comparison is made between the EoS and the optimized K-value based approaches. To ensure that the observed differences are not due to numerical errors, the results are presented at two different grid resolutions. For both phase behavior models, the critical air rate, which triggers ignition,

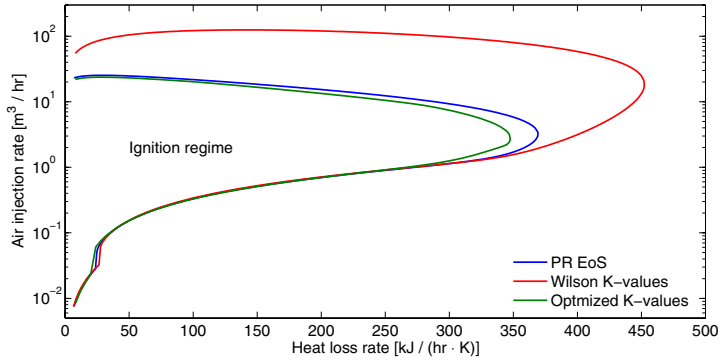

Figure 6.8: Ignition/extinction regimes for the SARA reaction model using the VKC. Comparison is made between EoS based and K-value based phase behavior representations.

does not change when the grid is refined. We take this an indication that the solution has converged. At low air rates, a stable combustion front cannot be sustained, and the system remains in a non-ignited state after the heater is shut off. At a certain point, when the air rate is increased, the system jumps onto a high-temperature ignition branch. This behavior is common to many reaction engineering problems, where two (pseudo) stationary, stable branches exist, corresponding to ignition and extinction. For a certain interval of air injection rate, an intermediate, unstable branch exists, which is, however, not readily captured in our numerical experiment.

In the optimized K-value based approach, a higher air injection rate is required to reach ignition compared to the EoS based approach. Figure 6.9(b) shows the iginition/extinction behavior when also varying the ignition heater rate. The observed behavior is in qualitative agreement with the results from the VKC, in that the EoS approach predicts the largest area of ignition in both cases. Consequently, the optimized K-values may overestimate the required air injection rate to sustain combustion. To illustrate the potentially dramatic difference in system behavior when operating near ignition/extinction branches, we simulate the VCT with an air injection rate of $0.012\,{}^{\mathrm{m}^3}/_{\mathrm{hr}}$ and ignition heater rate of $70\,{}^{\mathrm{kJ}}/_{\mathrm{hr}}$ (see Figure 6.10). With the full EoS, a stable combustion front is established, whereas in the K-value approach the system never reaches ignition.

As a final investigation, we consider the SARA reaction model and study ignition/extinction behavior with the VCT. Figure 6.11 shows the front temperature as a function of air injection rate. Again, a higher rate is required to sustain combustion when using the K-value approach, but the difference is smaller compared to the minimal model, and combustion can generally be sus-

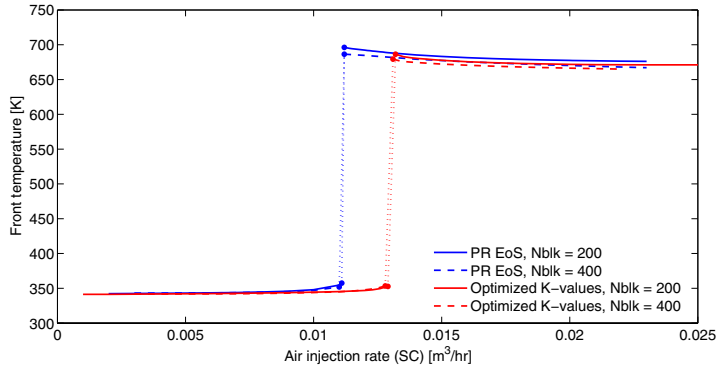

(a) Front temperature vs. air injection rate.

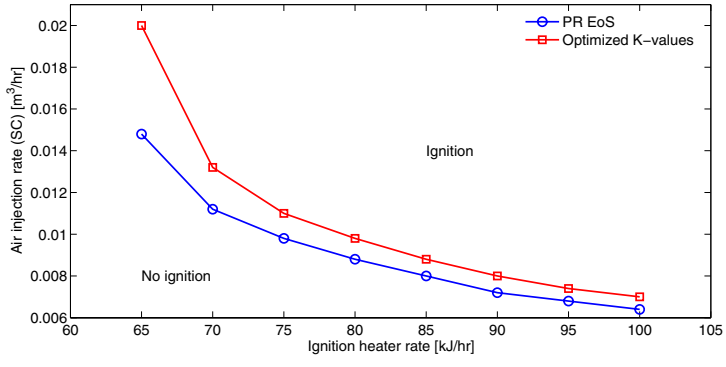

(b) Ignition/extinction curves.

Figure 6.9: Ignition/extinction behavior for the 1D VCT using the minimal reaction model. Above: combustion front temperature as a function of air injection rate for a specific ignition heater rate. Below: Ignition/extinction curves for varying air rates and ignition heater rates.

tained at very low injection rates. The shape of the curves indicates that there are several operation regimes, and the change to the high-temperature combustion regime is more gradual. The SARA model accounts for low-temperature oxidation reactions which dominate when the air supply is insufficient to reach high-temperature combustion.

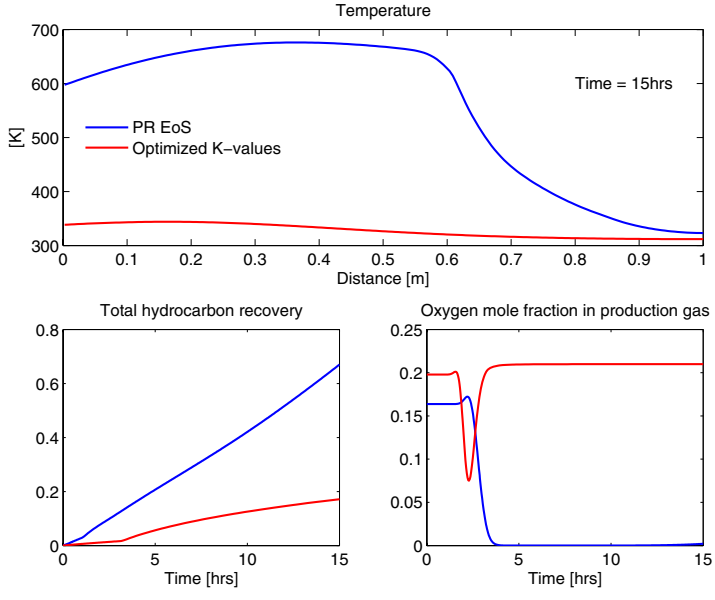

Figure 6.10: VCT simulation comparison for the minimal reaction model when operating near and ignition/extinction branch. Temperature profiles are shown along with total cumulative hydrocarbon recovery and oxygen mole fraction in the production gas.

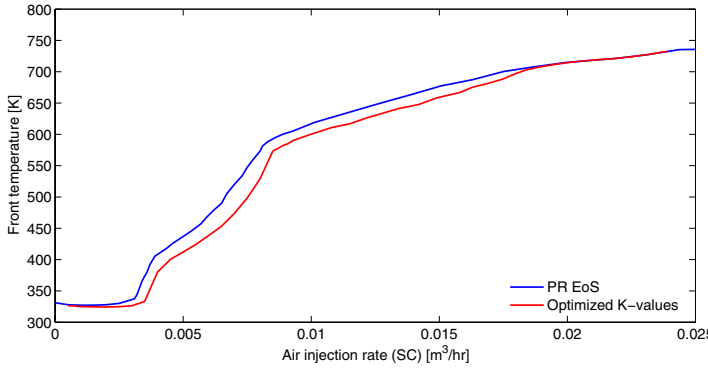

Figure 6.11: Ignition/extinction behavior for the 1D VCT using the SARA based reaction model. The combustion front temperature is shown as a function of air injection rate.

6.6 Discussion and future directions

In this paper we demonstrate that numerical solutions for ISC processes are very sensitive to numerical and modeling errors. The sensitivity to numerical errors is directly evident from the convergence plots shown in Section 6.4.4. At least 200 gridblocks are needed for the numerical errors in space and time not to strongly affect the solution quality. The errors observed are not only due to numerical discretization, but are also a result of upscaling of the kinetics. For the minimal reaction model, coarsening of the grid leads to excessive coke formation, which critically affects the front propagation speed and, hence, the oil recovery. The grid sensitivity study provides guidelines for the number of gridblocks required between wells in a practical reservoir setting in order to achieve a certain level of accuracy in the solution. In fact, for actual reservoirs, upscaling errors will be much larger, and the results here only indicate a lower bound on the number of gridblocks required. For the combustion tube problem we carried out the simulations with a minimum of 200 blocks to reduce numerical errors and isolate phase behavior model differences. In general, the number of gridblocks required to reduce the error below a threshold accuracy will be both process and oil dependent. Hence, it is essential to always conduct a grid convergence study.

The sensitivy to modeling errors is analyzed here for phase behavior models. For the VKC simulations we observe an extended area of ignition when using a K-value approach based on Wilson's correlation. This behavior is expected, since the correlation extends the pure component vapour pressure curves beyond their critical temperature, and, hence, tends to overestimate the size of the two-phase region. Since ISC kinetics is commonly modeled as gas-liquid or gas-solid (in case of reactions involving coke) reactions with rates typically depending on oxygen partial pressure and the concentration of an oil component in the oil phase, underestimation of oil volatility will lead to prediction of ignition for a wider range of operating conditions. Thus, our results for Wilson K-values agree with the expected behavior. The predicted ignition regimes from the EoS approach and the optimized K-values differ only slightly for the VKC, but when coupled with flow and transport in the one-dimensional VCT, the sensitivity seems stronger. For example, from the results in Section 6.5.2, for a particular ignition heater setting, there is a 17% difference in the critical air flow rate required to sustain combustion between the optimized K-value approach and the EoS approach. The optimized K-value approach leads to a smaller ignition regime, which is in agreement with the observed behavior in the VKC. Thus, while the VCT simulates actual ISC processes, the same qualitative conclusions concerning impact of phase behavior models can be obtained from VKC simulations. The ranges of air injection rates in both the VKC and VCT simulations are representative for practical ISC laboratory experiments.

It is not surprising that we find this sensitivity, given the assumption of phase specific reactions, which makes the kinetics sensitive to the distribution of components among phases. The API gravity of the two oils considered in

this work (25 °API and 16 °API, respectively) is in the medium to heavy range. The heavy, SARA based oil shows less sensitivity to phase behavior when simulated in the VCT. It seems intuitive that lighter oils will be more sensitivity to phase behavior, in which case the assumption of only liquid based reactions for hydrocarbon components is questionable. Current industry simulators allow specification of reactions in all phases, but we are not aware of any published work on ISC kinetics for gas phase reactions.

The sensitivity to phase behavior generally means that it is advisable to conduct experiments using a VKC or VCT before any field experimentation to assess how strongly results may be affected. Based on these experiments a decision can be made concerning which phase behavior representation to use. In general, the experience gained from VKC and VCT simulations will reduce the work required and improve understanding of the results when extending simulation to the field.

In the Whitson characterization procedure used for the Peng-Robinson EoS, critical parameters are estimated from liquid density and normal boiling point data through a set of correlations. Several characterization procedures exist, and although not addressed in this work we expect to see sensitivity also to the choice of characterization procedure. Moreover, the pseudoization of the oils considered here was done for kinetics and not for phase behavior. The SARA fractions are kinetically different, but each fraction may span a range of components with very different phase behavior. For example, the saturates pseudo component covers basically all saturated hydrocarbons with straight or branched chains. A further subdivision of the fractions based on boiling point may improve the representation of phase behavior, but it is outside the scope of this paper to study effects of pseudoization. We note, however, that the development of systematic pseudoization techniques for reactive-compositional processes, which take into account both reactivity and phase behavior, is an important area for future research and one of the current bottlenecks in the development of reliable models for ISC.

A natural extension of the work presented in this paper is to consider multi-dimensional problems, which introduces additional parameters affecting the behavior of ISC processes, and which cannot be studied in a one-dimensional model. Of particular interest is the sensitivity to reservoir heterogeneity, the important question being how the formation and sustained propagation of an ISC combustion front is affected by heterogeneities in the reservoir rock. For multi-dimensional problems we need improved numerical methods, and we are currently working on a computational framework, which leverages on adaptive gridding and operator splitting techniques to address the multi-scale nature of ISC processes (Younis and Gerritsen, 2006; Nilsson et al., 2005; Kristensen et al., 2007*b*).

6.7 Conclusions

The main conclusions of this work are:

- The Virtual Combustion Tube (VCT) is a novel, equation of state compositional simulator for in-situ combustion (ISC). The simulator is validated through careful convergence studies as well as comparisons with the industry standard simulator STARS. The VCT is implemented with both equation of state based and simplified K-value based phase behavior descriptions, which enables studies of differences to improve understanding of phase behavior for ISC processes.

- The sensitivity to grid step size shows that careful grid convergence studies are needed in each reservoir study.

- The choice of phase behavior model impacts ISC process performance. Different models lead to different regimes of ignition. Driven by chemical reactions, ISC processes rely critically on reaching proper ignition conditions. Although difficult to rigorously quantify, there are areas of operating conditions (such as air injection rate), where a change from a simple K-value based phase behavior description to an equation of state based description will change the system dynamics, and therefore performance predictions, dramatically (from ignition to extinction). The oils tested here are in the medium to heavy range. More volatile oils are likely to be more sensitive to phase behavior. Strict guidelines cannot be given at this stage as to which phase behavior model to use, but the decision must be based on a sensitivity study for the particular oil.

- The VCT and VKC provide a reliable and flexible platform for the study and support of laboratory scale combustion experiments. Although limited in physics, the VKC sensitivity results agree qualitatively with the VCT, and the VKC can thus be used as a fast screening tool when assesssing different kinetics and phase behavior models. Simulations using the VCT and VKC are the natural first steps before going to full-scale models.

Acknowledgement

The authors would like to thank Wei Yan, IVC-SEP, Technical University of Denmark, for generous help on oil characterization for the SARA fractions model.

Component Name	Abbreviation
Water	H_2O
Inert oil	InertOil
Oxidized resins/aromatics	OxdResAr
Oxidized saturates	OxdSat
Asphaltenes	Asph
Resins	Resins
Aromatics	Arom
Saturates	Sat
Light oil	Lites
Carbon dioxide	CO_2
Nitrogen	N_2
Oxygen	O_2
Oxidized asphaltenes	OxdAsph
Pyrolysis coke	PyrCoke

Table 6.1: List of (pseudo) components for the SARA based model.

6.8 ISC reaction models

6.8.1 The minimal model

The components in the model are light oil (LO), heavy oil (HO), coke (C), oxygen (O_2), water (W) and inert gas (IG). The reactions are

$$\begin{aligned} \mathrm{LO} + \mathrm{O_2} &\rightarrow \mathrm{IG} + \mathrm{W} \\ \mathrm{HO} + \mathrm{O_2} &\rightarrow \mathrm{IG} + \mathrm{W} \\ \mathrm{HO} &\rightarrow \mathrm{LO} + \mathrm{C} + \mathrm{IG} \\ \mathrm{C} + \mathrm{O_2} &\rightarrow \mathrm{IG} + \mathrm{W}. \end{aligned} \tag{6.17}$$

6.8.2 The SARA model

The components of the model are listed in Table 6.1, and the reaction are given below.

$$
\begin{array}{ll}
\text{cracking/} & \begin{cases} \text{Asph} & \rightarrow \quad \text{H}_2\text{O} + \text{Arom} + \text{Sat} + \text{Lites} + \text{PyrCoke} \\ \text{Resins} & \rightarrow \quad \text{H}_2\text{O} + \text{Asph} + \text{Arom} + \text{Sat} + \text{Lites} \\ \text{Arom} & \rightarrow \quad \text{Asph} + \text{Lites} \end{cases} \\
\text{pyrolysis} & \\
\text{LTO} & \begin{cases} \text{Asph} + \text{O}_2 & \rightarrow \quad \text{H}_2\text{O} + \text{CO}_2 + \text{OxdAsph} \\ \text{Resins} + \text{O}_2 & \rightarrow \quad \text{H}_2\text{O} + \text{CO}_2 + \text{OxdResAr} \\ \text{Arom} + \text{O}_2 & \rightarrow \quad \text{H}_2\text{O} + \text{CO}_2 + \text{OxdResAr} \\ \text{Sat} + \text{O}_2 & \rightarrow \quad \text{H}_2\text{O} + \text{CO}_2 + \text{OxdSat} \end{cases} \\
\text{HTO} & \begin{cases} \text{PyrCoke} + \text{O}_2 & \rightarrow \quad \text{H}_2\text{O} + \text{CO}_2 \\ \text{OxdAsph} + \text{O}_2 & \rightarrow \quad \text{H}_2\text{O} + \text{CO}_2 \\ \text{OxdResAr} + \text{O}_2 & \rightarrow \quad \text{H}_2\text{O} + \text{CO}_2 \\ \text{OxdSat} + \text{O}_2 & \rightarrow \quad \text{H}_2\text{O} + \text{CO}_2 \\ \text{Asph} + \text{O}_2 & \rightarrow \quad \text{H}_2\text{O} + \text{CO}_2 \\ \text{Resins} + \text{O}_2 & \rightarrow \quad \text{H}_2\text{O} + \text{CO}_2 \\ \text{Arom} + \text{O}_2 & \rightarrow \quad \text{H}_2\text{O} + \text{CO}_2. \end{cases}
\end{array}
\tag{6.18}
$$

6.9 Control-volume discretization

Consider the 1D case with equidistant grid-spacing, and let $S_k = \{S_{k+1/2}, S_{k-1/2}\}$ denote the surfaces of gridblock k. Substituting (6.6) and (6.7) in (6.4) and introducing the flow potential

$$\nabla\Phi^j = \nabla P - \rho^j g \nabla D, \tag{6.19}$$

the flow terms can then be discretized as

$$
\begin{aligned}
\int_{S_k} \mathbf{q}_i^m \cdot \mathbf{n} d\mathcal{S} &= -\int_{S_k} \sum_j \frac{x_i^j \xi^j k_r^j}{\mu^j} \mathbf{k} \nabla\Phi^j \cdot \mathbf{n} d\mathcal{S} \\
&\simeq \sum_j \Lambda_{i,k+1/2}^j T_{k+1/2} \Delta^+ \Phi_k^j - \Lambda_{i,k-1/2}^j T_{k-1/2} \Delta^- \Phi_k^j,
\end{aligned}
\tag{6.20}
$$

where $T_{k\pm1/2}$ is the transmissibility for the gridblock connections, $\Lambda_{i,k\pm1/2}^j$ is the generalized mobility

$$\Lambda_{i,k\pm1/2}^j = \left(\frac{x_i^j \xi^j k_r^j}{\mu^j} \right)_{k\pm1/2}, \tag{6.21}$$

which is evaluated in the upstream direction, and the discrete flow potentials are

$$
\begin{aligned}
\Delta^+ \Phi_k^j &= P_{k+1} - P_k - \rho_{k+1/2}^j g \left(D_{k+1} - D_k \right) \\
\Delta^- \Phi_k^j &= P_k - P_{k-1} - \rho_{k-1/2}^j g \left(D_k - D_{k-1} \right),
\end{aligned}
\tag{6.22}
$$

where the mass density in the gravity term is evaluated as a saturation weighted average

$$\rho^j_{k\pm1/2} = \frac{S^j_{k\pm1}\rho^j_{k\pm1} + S^j_k\rho^j_k}{S^j_{k\pm1} + S^j_k}. \tag{6.23}$$

The heat flux terms in (6.8) are discretized in a similar way

$$\begin{aligned}\int_{S_k} \left(\mathbf{q}^{h,adv} + \mathbf{q}^{h,cond}\right)\cdot \mathbf{n} d\mathcal{S} &= -\int_{S_k}\left(\sum_j \frac{h^j\xi^j k^j_r}{\mu^j}\mathbf{k}\nabla\Phi^j + \mathbf{k}_c\nabla T\right)\cdot\mathbf{n}d\mathcal{S}\\ &\simeq \sum_j \Lambda^{j,h}_{k+1/2}T_{k+1/2}\Delta^+\Phi^j_k - \Lambda^{j,h}_{k-1/2}T_{k-1/2}\Delta^-\Phi^j_k\\ &\quad + \frac{S_{k+1/2}k_{c,k+1/2}}{\Delta x}\Delta^+T_k - \frac{S_{k-1/2}k_{c,k-1/2}}{\Delta x}\Delta^-T_k,\end{aligned} \tag{6.24}$$

where the fluid dependent parts of the interface heat conductivity $k_{c,k\pm1/2}$ are evaluated upstream in temperature (see Section 6.10.3 for calculation of effective heat conductivity). The fluid dependent part in the discretized advective term is

$$\Lambda^{j,h}_{k\pm1/2} = \left(\frac{h^j\xi^j k^j_r}{\mu^j}\right)_{k\pm1/2}. \tag{6.25}$$

6.10 Constitutive models

The constitutive models used for phase equilibrium, chemical reactions, wells, and rock and fluid properties are given in this section. We have implemented different choices for property models depending on the choice of phase behavior treatment. In the K-value approach we assume ideal mixing of pure component properties, whereas for the EoS approach we use the EoS itself to model phase densities and enthalpies. In all the sensitivity studies in the paper we have used the simplified set of property models, so that the differences observed reflect only differences in phase behavior treatment.

6.10.1 Phase equilibrium

K-value based approach

We use the Wilson correlation

$$\ln K_i = \frac{P^{crit}_i}{P} + 5.373\,(1+\omega_i)\left(1 - \frac{T^{crit}_i}{T}\right), \tag{6.26}$$

where P^{crit}_i, T^{crit}_i and ω_i are the critical pressure and temperature and accentric factor, respectively, for component i.

EoS based approach

In the EoS approach, the fugacities in (6.12) are obtained from an EoS. We use the Peng-Robinson EoS (Peng and Robinson, 1976). Details on the EoS and computation of fugacities can be found in e.g. Michelsen and Mollerup (2004) or Whitson and Brule (2000).

6.10.2 Chemical reactions

The chemical reactions are assumed to be kinetically driven, and are modeled using standard Arrhenius rate relation, where the rate depends on component concentrations in a specific phase. Generally, two different kinds of reactions dominate ISC processes: cracking/pyrolysis reactions and oxidation (full/partial) reactions. The thermal cracking of component i in phase j is modeled as

$$R_\gamma = K_\gamma \cdot \left(\phi_f S^j \xi^j x_i^j\right)^{m_\gamma}, \tag{6.27}$$

where γ is used to index the reaction number and m_γ is the reaction order in the component concentration. Oxidation reactions are generally heterogeneous reactions between oxygen in the gas phase and an oil component in the oil phase, and they are modeled using the oxygen partial pressure

$$R_\gamma = K_\gamma \cdot \left(P x_{o_2}^g\right)^{n_\gamma} \cdot \left(\phi_f S^j \xi^j x_i^j\right)^{m_\gamma}. \tag{6.28}$$

The rate constants are temperature dependent according to Arrhenius's law

$$K_\gamma = \alpha_\gamma \exp\left(-\frac{E_a^\gamma}{R_g T}\right), \tag{6.29}$$

where α_γ is the frequency factor, E_a^γ is the activation energy and R_g is the universal gas constant. From the reaction rates we can express the mass and heat source densities in equations (6.4) and (6.8). The net production of component i in chemical reactions is

$$Q_i^{m,reac} = \sum_\gamma A_{i\gamma} R_\gamma, \tag{6.30}$$

where $A_{i\gamma}$ is the stoichiometric coefficient for component i in reaction γ (negative for reactants, positive for products). Similarly, the net heat generation is

$$Q^{h,reac} = \sum_\gamma (-\Delta H)_\gamma^r R_\gamma, \tag{6.31}$$

where $-\Delta H^r$ is the heat of reaction.

6.10.3 Rock and fluid properties

For comparison purposes we have implemented the same set of property models as used by the commercial simulator CMG STARS (CMG, 2004). In addition, when using the EoS phase behavior approach, we have included an option to use densities and residual enthalpies from the EoS.

Relative permeabilities

Relative permeabilities are modeled using the normalized Stone II model (Stone, 1973).

Effective porosity

The porosity available to fluid flow depends on solid concentration and is modeled as

$$\phi_f = \phi_v - \sum_{i \in \mathcal{I}^s} \frac{C_i}{\xi^s}, \tag{6.32}$$

where C_i is the concentration per unit reservoir volume.

Density

Phase densities are evaluated from the EoS. We may write a general cubic EoS in the form

$$\left(Z^j\right)^3 + c_2 \left(Z^j\right)^2 + c_1 \left(Z^j\right) + c_0 = 0, \tag{6.33}$$

where Z^j is the phase compressibility factor, and where the coefficients c_2, c_1 and c_0 depend on pressure, temperature and phase composition. Solving Eqn. (6.33) for Z^j we can express the molar and mass phase densities as

$$\xi^j = \frac{P}{R_g T Z^j}, \qquad \rho^j = \xi^j \sum_i x_i^j M_i. \tag{6.34}$$

In the ideal case we assume $Z^g = 1$, and pure component liquid densities are obtained from

$$\xi_i^o = \xi_{i,ref}^o \exp\left(c_i^p (P - P_{ref}) - c_i^t (T - T_{ref})\right), \tag{6.35}$$

where $\xi_{i,ref}^o$ is the density at the reference conditions, and the coefficients c_i^p and c_i^t are the compressibility and thermal expansion, respectively. Linear mixing of molar volumes is assumed

$$\frac{1}{\xi^o} = \sum_i \frac{x_i^o}{\xi_i^o}. \tag{6.36}$$

Water density is calculated according to a correlation similar to (6.35).

Viscosity

Accurate modeling of oil phase viscosity is important for ISC processes, since the reduction in oil viscosity with temperature is the primary mechanism for enhanced recovery. Pure component viscosities can be entered either through tables or obtained from the correlation

$$\mu_i^o = a_i^o \exp\left(\frac{b_i^o}{T}\right), \tag{6.37}$$

where a_i^o and b_i^o are correlation constants. The oil phase viscosity is then obtained by logarithmic mixing of the pure component viscosities

$$\ln \mu^o = \sum_i x_i^o \ln \mu_i^o. \tag{6.38}$$

Accuracy in gas phase viscosity is generally less important. The correlation used here is

$$\mu_i^g = a_i^g T^{b_i^g}, \tag{6.39}$$

and the mixing rule used is

$$\mu^g = \sum_i \frac{x_i^g \sqrt{M_i} \mu_i^g}{x_i^g \sqrt{M_i}}. \tag{6.40}$$

Water viscosity is obtained from a correlation similar to (6.37).

Enthalpy

Phase enthalpies are computed from ideal gas heat capacity correlations and vaporization enthalpy correlations. For a pure component gas we have

$$h_i^{g,id} = \int_{T_{ref}}^{T} C_{p,i}(\bar{T}) d\bar{T}, \tag{6.41}$$

where T_{ref} is the temperature of the reference state. In the ideal case the vaporization enthalpy is obtained from the correlation (CMG, 2004)

$$h_i^{vap} = hv_i^1 \left(T_i^{crit} - T\right)^{hv_i^2}, \tag{6.42}$$

where T_i^{crit} is the component critical temperature and hv_i^1 and hv_i^2 are correlation constants. Thus, for the ideal case we have

$$h^g = \sum_i x_i^g h_i^{g,id} \tag{6.43a}$$

for the gas phase and

$$h^o = \sum_i x_i^o \left(h_i^{g,id} - h_i^{vap}\right) \tag{6.43b}$$

for the oil phase. In the non-ideal case the residual enthalpies are obtained from the EoS leading to

$$h^g = \sum_i x_i^g h_i^{g,id} + h^{g,res} \tag{6.44a}$$

$$h^o = \sum_i x_i^o h_i^{g,id} + h^{o,res}, \tag{6.44b}$$

where $h^{j,res}$ is the residual enthalpy of phase j. The water phase enthalpy is obtained from correlations similar to (6.41) and (6.42).

Internal energy

The total internal energy can be expressed as

$$U = (1-\phi_v)\, U^r + (\phi_v - \phi_f)\, \xi^s U^s + \phi_f \sum_j \xi^j S^j U^j, \tag{6.45}$$

where U^r is the volumetric internal energy of rock, and U^j is the molar internal energy of phase j, which is obtained from the enthalpy by subtraction of the mechanical work

$$U^j = h^j - \frac{P}{\xi^j}. \tag{6.46}$$

Thermal conductivity

The mobile and immobile phases have associated with them a scalar thermal conductivity k_c^j. Moreover, the rock has an associated tensorial thermal conductivity denoted $\mathbf{k}_c^r$. The effective thermal conductivity of the saturated porous medium is computed as a weighted volume average

$$\mathbf{k}_c = (1-\phi_v)\, \mathbf{k}_c^r + \left[(\phi_v - \phi_f)\, k_c^s + \phi_f \sum_j S^j k_c^j \right] \mathbf{I} \tag{6.47}$$

In this paper we assume the rock conductivity to be isotropic.

6.10.4 Well models

We consider wells completed in a single gridblock and two types of well operations: fixed single-phase injection rate for injectors and fixed back pressure for producers. Typically, a fixed gas rate (air or oxygen enriched air) is specified, or both water and gas rates are specified as for wet combustion processes. The component source density due to wells can be written

$$Q_i^{m,well} = -\sum_j \frac{x_i^j \xi^j k_r^j}{\mu^j} WI\, (P - P_w)\,, \tag{6.48}$$

where WI is the well index, P is the block pressure and P_w is the well bottom-hole pressure. Expressions for the well index for standard block-centered cartesian grids can be found in Aziz and Settari (1979). The heat source density due to wells can be written as

$$Q^{h,well} = -\sum_j \frac{h^j \xi^j k_r^j}{\mu^j} WI \left(P - P_w\right). \tag{6.49}$$

The outer boundaries of the reservoir are assumed closed, and mass is only transported in and out of the system through wells. However, in general heat losses will occur to the surrounding formation through heat conduction. Since in this paper we are primarily concerned with the simulation of laboratory scale combustion tubes, we will model heat losses using an external proportional heat controller

$$Q^{h,htr} = -u_a \left(T - T^{ext}\right), \tag{6.50}$$

where u_a is a heat transfer coefficient (or controller gain) and T^{ext} is the external heating/cooling temperature (controller set point).

Chapter 7

Conclusions

The primary focus of the work presented in this thesis has been the development of simulation models and algorithms for the study of reactive porous media processes with emphasis on in-situ combustion (ISC) enhanced oil recovery. The overall conclusions of the work are summarized in this chapter.

The motivation for addressing this topic has been the high potential of ISC as a primary recovery process for the world's vast heavy oil reserves as well as a tertiary process in waterflooded, light oil reservoirs. Predictive mathematical models and robust and efficient numerical simulators are essential for safe and cost effective design of ISC processes. A review of the relevant literature showed that there is a need for improvements to current mathematical models, especially in the modeling of simultaneous reactive and compositional effects. Moreover, current simulation algorithms for ISC do not take into account the multiscale nature of the process, and possible improvements exist in the design and development of tailored numerical methods.

The main modeling contributions of this work are the Virtual Combustion Tube (VCT) and the Virtual Kinetic Cell (VKC). The VCT is an Equation-of-State (EoS) compositional, one-dimensional ISC model for laboratory scale combustion simulation. It accounts for the simultaneous flow, transport of heat and mass, chemical reactions, and phase equilibrium. The VKC is a zero-dimensional version of the VCT. The VKC models a multiphase, chemical batch reactor where only chemical reactions and phase behavior are taken into account. In both the VCT and VKC a dual strategy is implemented for phase behavior and fluid property modeling, using both a cubic EoS and an ideal mixture approach, where, in the latter, phase behavior is modeled from pressure-temperature K-

value correlations. Together, the two models provide a flexible platform for the study and support of laboratory scale combustion experiments.

The VKC and VCT allow rigorous treatment of phase behavior based on an EoS. This feature, not shared by other ISC models, enables a study of the importance of accurate phase behavior representation for ISC. The efficiency of ISC processes depends critically on the formation and sustained propagation of a high-temperature combustion front. Thus, reaching proper ignition conditions is very important. We employed the VKC and VCT to study ignition/extinction phenomena in ISC as a function of key operating conditions such as air injection rate and external heat loss rate. We showed that in certain operating regimes a change of phase behavior model will shift the system from ignition to extinction or vice versa. For a particular 25 °API gravity oil there was a 17% difference in the air flow rate required to sustain combustion between the EoS based phase behavior approach and a K-value based approach. Although based on limited data, our observations showed that the sensitivity to phase behavior modeling is stronger for lighter oils.

The VCT can be used quantitatively to map ignition/extinction regimes as a function of key parameters, which we have illustrated in this work for air injection rate and heat loss rate. We showed that, qualitatively, the same conclusions regarding impact of different phase behavior models can be obtained from simulations using the VKC. Thus, the VKC should be used as a fast screening tool when assessing different kinetics and phase behavior models. All sensitivity studies were performed carefully to ensure that the results were converged, so that the differences observed reflected only differences in modeling approaches, and that they were not due to numerical approximation errors.

With respect to simulation algorithms, the main focus in this work has been on the design of a time integration methodology for ISC, which addresses the underlying multiscale character of the process. In particular, we have focused on efficient integration methods for chemical kinetics and phase behavior. We proposed a simple and intuitive integration scheme for ISC based on operator splitting techniques, where the chemical reaction terms in the equations are essentially decoupled from the flow and transport terms during integration. This approach is attractive for problems with disparate time scales, such as ISC, and it facilitates the construction of efficient, tailored integration methods for each subprocess in the problem. We focused on the reaction subprocess and designed a family of integration methods of varying order based on the ESDIRK subclass of the Runge-Kutta methods. The ESDIRK methods are well-suited for short-interval integration of mixed differential-algebraic equations as required in an operator splitting approach for ISC. Careful benchmark studies against popular off-the-shelf stiff ODE solvers showed that the ESDIRK methods were 2–5 times faster in the accuracy range of 2–4 correct digits in the solution, which we expect to be of practical interest in ISC simulations.

Fluid phase changes cause non-smooth behavior in the equations, which often results in convergence problems and repeated step failures. Based on the

concept of discrete event systems we proposed an algorithm for detecting and consistently locating phase changes. Most often phase changes occur between mesh points. The algorithm detects phase changes as sign changes in special event functions and subsequently locates the exact time of occurrence. The ESDIRK integration methods were extended with the phase change detection algorithm. Isolated VKC simulations showed that the proposed algorithm improves the integration robustness near phase boundaries by lowering the number convergence and error test failures compared to direct integration without the algorithm.

In conclusion, the key contributions of this work are: (i) the two models, the VKC and the VCT, which facilitate fundamental studies of laboratory scale combustion experiments, (ii) efficient, tailored integration methods for ISC with emphasis on algorithms for kinetics and phase behavior, and (iii) improved understanding of compositional effects and their impact on ignition/extinction dynamics in ISC processes.

7.1 Suggestions for future work

During the course of the work presented in this thesis a number of related problems were encountered, the treatment of which has been outside the scope of the work. We summarize here the most important problems in the form of possible topics for future work.

A natural and important next step in model development is validation of the models with experimental data. Unfortunately, experimental data in the form of temperature profile measurements and production data from laboratory combustion tube tests, have not been available to us. With such data available, possible model deficiencies can be located and improved, and uncertain parameters can be estimated. The sensitivity study conducted in this thesis for phase behavior modeling showed that the system dynamics will change dramatically in certain regions of the parameter space, if the phase behavior model is changed. Without experimental data it is, however, not possible to give strict guidelines as to which phase behavior modeling approach should be used. The appropriate choice will be case dependent, but it should be based on sensitivity studies using the VKC and VCT.

A possible application of the models is in the design of experiments. For example, parametric sensitivity studies can be used to determine regions of the parameter space where additional laboratory experiments should be carried out. The models can also be applied to help determine optimal experimental conditions in the design phase, so that when carried out, the data obtained from the experiments will have optimal information content. This process, which ties together model building and experimental design, is inherently iterative. The model is formulated, and parameters are estimated from experimental data. Experiments are then designed based on the model, and the data obtained is

used to improve the model and reestimate the parameters.

An important modeling aspects with close links to the experimental side of ISC, but outside the scope of this thesis, is oil pseudoization procedures for ISC. Most pseudoization techniques are designed to match PVT properties of the oil. The development of systematic pseudoization techniques for reactive-compositional processes, which take into account both reactivity and phase behavior, is an important area for future research and one of the current bottlenecks in the development of reliable models for ISC. Moreover, based on a particular oil component representation, a reaction model must be established and kinetic parameters determined, which is also an area requiring the development of more systematic procedures.

The ignition/extinction behavior in ISC was studied in this thesis for two parameters. Following the non-dimensional analysis of the ISC equations in Younis and Gerritsen (2006) this study of regimes of dominating behavior can be generalized. To be more specific, the ISC equations can be parameterized in terms of a limited number of dimensionless groups, which govern the relative importance of different physics, e.g. the importance of reaction over convection as measured by the Damköhler number. The regimes of dominating behavior, such as the high-temperature oxidation regime, can then be mapped in the parameter space defined by the dimensionless groups. In principle, this mapping of the physics in terms of dimensionless groups will make available important information regarding the behavior of an ISC process and the type of operation, which can be expected, given a specific oil and reservoir. In practice a complete analysis is difficult, since ISC processes are characterized by up to seven dimensionless groups (Younis and Gerritsen, 2006).

With respect to numerical methods for ISC simulation, several topics deserve more attention. In continuation of the work presented in this thesis the most important such topic is further research into tailored integration methods. Integration methods based on operator splitting techniques are attractive for ISC due to the multiscale nature of the process, but more work is needed to validate and further develop the proposed splitting scheme and compare the accuracy and performance of the scheme to the fully coupled approach. Compared to other reactive porous media processes, such as contaminant migration problems in groundwater hydrology, where splitting methods are well established, the distinguishing feature of ISC is the strong coupling between flow and reactions. The heat released in reactions, which causes the oil mobility to decrease, is the primary driving mechanism in heavy oil ISC. For light oil processes the combustion gases evolved in reactions provide the main mobilizing energy, but in both cases there is a strong feedback on flow from reactions. The decoupling of flow/transport and reactions in the splitting scheme therefore, naturally, introduces a splitting error. In this work we have not attempted to analyze the order and consistency of the splitting scheme, but future work should include such an analysis in order to understand how the splitting error is affected by, for example, the sequence of substeps, the stiffness of the operators, and the

treatment of boundary conditions.

Operator splitting methods provide a flexible framework for the design of an optimal integration scheme. Specialized numerical methods can be applied to subprocesses, and fractional steps can be introduced both at the scheme design level as well as in each substep. Optimal design requires knowledge of the dominating physical processes. This observation suggests a splitting scheme design, where the number and sequence of fractional steps and the implicitness and accuracy in each substep, is guided by governing dimensionless parameters. Since the dominating processes change during the course of an ISC process, the splitting scheme should change adaptively during a simulation. For example, a simulation may start out in a fully coupled, implicit mode when flow rates and reaction rates are small and heat conduction dominates during the onset of combustion. Later, when a combustion front is established, the simulation may switch to a splitting mode with explicit treatment of transport and implicit treatment with fractional steps for chemical reactions. However, much research still remains before a fully adaptive and physically guided splitting scheme can be realized.

Achieving a fully adaptive framework requires, in addition, that spatial multiscale behavior is addressed as well, a topic not touched upon in this thesis. The use of adaptive mesh refinement techniques, such as those developed in Nilsson et al. (2005), is an obvious topic for future work. The ability to refine the mesh in high-activity areas will be very important when extending to multi-dimensional problems.

Finally, we mention that, on the shorter term, a number of desirable extensions exist to the simulators developed as part of this work. These include merging of the phase change detection algorithm in the VCT simulator and derivation of an analytical Jacobian for the fully coupled, implicit scheme.

Appendix A

Derivation of ESDIRK methods

In this appendix we introduce and derive a family of Explicit Singly Diagonally Implicit Runge-Kutta (ESDIRK) methods. We outline the principles of construction of ESDIRK methods with embedded methods of different order for error estimation and continuous extensions for discrete event location. We refer to Paper I in Chapter 5 for a motivation of ESDIRK methods for integration of kinetics in ISC simulations. For a more thorough discussion of the properties of ESDIRK methods we refer to Jørgensen et al. (2008).

A.1 Runge-Kutta integration methods

Consider the differential-algebraic equation (DAE) system

$$\mathbf{M}\frac{d\mathbf{u}}{dt} = \mathbf{f}(t, \mathbf{u}), \qquad \mathbf{u}(t_0) = \mathbf{u}_0, \tag{A.1}$$

where $\mathbf{u} \in \mathbb{R}^n$ is a vector of state variables depending on t, and $\mathbf{f}$ is a vector function mapping $\mathbb{R} \times \mathbb{R}^n$ into $\mathbb{R}^n$. We assume a constant, but possibly singular, mass matrix $\mathbf{M} \in \mathbb{R}^n \times \mathbb{R}^n$. A general s-stage Runge-Kutta scheme for solving

the DAE system (A.1) can be expressed as

$$\mathbf{M}\mathbf{U}_i = \mathbf{M}\mathbf{u}_n + h\sum_{j=1}^{s} a_{ij}\mathbf{f}(t_n + c_j h, \mathbf{U}_j) \tag{A.2a}$$

$$\mathbf{M}\mathbf{u}_{n+1} = \mathbf{M}\mathbf{u}_n + h\sum_{i=1}^{s} b_i\mathbf{f}(t_n + c_i h, \mathbf{U}_i) \tag{A.2b}$$

$$\mathbf{e}_{n+1} = h\sum_{i=1}^{s} d_i\mathbf{f}(t_n + c_i h, \mathbf{U}_i), \tag{A.2c}$$

where $\mathbf{U}_i$ denotes the solution at the ith, $(i = 1, \ldots, s)$, internal stage of integration step n and h denotes the time step length. The coefficients of Runge-Kutta schemes are often represented in a Butcher tableau

$$\begin{array}{c|cccc} c_1 & a_{11} & a_{12} & \ldots & a_{1s} \\ c_2 & a_{21} & a_{22} & \ldots & a_{2s} \\ \vdots & \vdots & \vdots & \ddots & \vdots \\ c_s & a_{s1} & a_{s2} & \ldots & a_{ss} \\ \hline \mathbf{u}_{n+1} & b_1 & b_2 & \ldots & b_s \\ \hline \mathbf{e}_{n+1} & d_1 & d_2 & \ldots & d_s \end{array} \quad = \quad \begin{array}{c|c} \mathbf{c} & \mathbf{A} \\ \hline & \mathbf{b}^T \\ \hline & \mathbf{d}^T \end{array}. \tag{A.3}$$

A.1.1 Order conditions

To assess the accuracy of the integration and to adjust the step length we use the method of embedded formulas, where an estimate of the local integration error is computed from the difference between two approximations, $\mathbf{u}_{n+1}$ and $\hat{\mathbf{u}}_{n+1}$, having different orders of accuracy

$$\mathbf{e}_{n+1} = \mathbf{u}_{n+1} - \hat{\mathbf{u}}_{n+1}. \tag{A.4}$$

$\hat{\mathbf{u}}_{n+1}$ is computed like $\mathbf{u}_{n+1}$, but with its own set of quadrature weights, $\hat{b}_i$. The error coefficients in the Butcher tableau are then simply given as $d_i = b_i - \hat{b}_i$.

Definition A.1 (Order of accuracy) A method has order p, if the difference between a Taylor series for the exact solution through the point $\mathbf{u}_n$ evaluated at $\mathbf{u}(t_n + h)$ and the numerical solution $\mathbf{u}_{n+1}$ is $\mathcal{O}\left(h^{p+1}\right)$, i.e. the two expansions coincide up to and including the term h^p.

The order conditions for Runge-Kutta methods can be derived by comparing Taylor expansions for the exact and numerical solutions to the DAE (A.1). General order conditions can be found in Hairer and Wanner (1996). If we let $\mathbf{C} = \mathrm{diag}\{c_1, c_2, \ldots, c_s\}$ denote a diagonal matrix with $\{c_i\}_{i=1}^{s}$ on the diagonal,

and if we use the notation for the Butcher tableau coefficients introduced in (A.3), then the conditions for order $p = \{1, 2, 3, 4\}$ can be expressed as

$$\text{Order 1}: \quad \mathbf{b}^T\mathbf{e} = 1 \tag{A.5a}$$

$$\text{Order 2}: \quad \mathbf{b}^T\mathbf{C}\mathbf{e} = \frac{1}{2} \tag{A.5b}$$

$$\text{Order 3}: \quad \mathbf{b}^T\mathbf{C}^2\mathbf{e} = \frac{1}{3} \tag{A.5c}$$

$$\mathbf{b}^T\mathbf{A}\mathbf{C}\mathbf{e} = \frac{1}{6} \tag{A.5d}$$

$$\text{Order 4}: \quad \mathbf{b}^T\mathbf{C}^3\mathbf{e} = \frac{1}{4} \tag{A.5e}$$

$$\mathbf{b}^T\mathbf{C}\mathbf{A}\mathbf{C}\mathbf{e} = \frac{1}{8} \tag{A.5f}$$

$$\mathbf{b}^T\mathbf{A}\mathbf{C}^2\mathbf{e} = \frac{1}{16} \tag{A.5g}$$

$$\mathbf{b}^T\mathbf{A}^2\mathbf{C}\mathbf{e} = \frac{1}{24}, \tag{A.5h}$$

where $\mathbf{e} = [1\ 1\ \cdots\ 1]^T$ is the s-dimensional unity vector. In addition to these classical order conditions we impose conditions on each internal stage of the integration scheme. Each stage (A.2a) is itself an approximation to the DAE. The approximation order, q, of the internal stages is referred to as the *stage order* of the method which is typically less than the classical order. It can be shown that the stage order influences the order of accuracy in the algebraic components of the DAE (Hairer and Wanner, 1996). Having high stage order is therefore important. Requiring stage order q leads to the following additional set of conditions

$$\sum_{j=1}^{s} a_{ij} c_j^{k-1} = \frac{1}{k} c_i^k, \qquad i = 1, \ldots, s; \quad k = 1, \ldots, q. \tag{A.6}$$

Definition A.2 (Stiff accuracy) Runge-Kutta methods satisfying the condition that the last row of the coefficient matrix $\mathbf{A}$ in (A.3) is equal to the quadrature weights, $a_{sj} = b_j,\ j = 1, \ldots, s$, are *stiffly accurate*.

Stiffly accurate methods satisfy the property that the last stage is equal to the final solution, $\mathbf{u}_{n+1} = \mathbf{U}_s$, and no extra computations are therefore needed to ensure consistency of the algebraic equations in (A.1). Stiffly accurate methods avoid the order reduction phenomenon (Prothero and Robinson, 1974) when applied to stiff problems. The explicit first stage of ESDIRK methods together with the stiffly accurate requirement ensure that the stage order of the first and last stages is equal to the basic integration order. Thus, it is only necessary to impose the stage order conditions (A.6) on stages $i = 2, \ldots, s-1$.

A.1.2 Stability conditions

Assessment of stability is associated with the scalar linear equation $\dot{u} = \lambda u$, $u(0) = u_0$, where $\lambda \in \mathbb{C}$. For all Runge-Kutta methods, advancing one step in the solution of this equation is equal to the multiplication with a rational function

$$u_{n+1} = R(h\lambda)u_n, \tag{A.7}$$

where the rational function is given by

$$R(z) = 1 + z\mathbf{b}^T \left(\mathbf{I} - z\mathbf{A}\right)^{-1} \mathbf{e} = \frac{\det\left(\mathbf{I} - z\mathbf{A} + z\mathbf{e}\mathbf{b}^T\right)}{\det\left(\mathbf{I} - z\mathbf{A}\right)} = \frac{P(z)}{Q(z)}, \qquad z \in (C), \tag{A.8}$$

where $\mathbf{I}$ is the s-dimensional identity matrix. The stability region is defined as the set of points in the complex plane for which $|R(z)| < 1$.

Definition A.3 (A-stability) A method for which the stability region includes all of the left half-plane, $|R(z)| < 1$ for $\mathrm{Re}(z) < 0$, is said to be *A-stable*.

Definition A.4 (L-stability) A method is *L-stable*, if it is A-stable and satisfies $\lim_{z\to-\infty}|R(z)| = 0$.

For ESDIRK methods, $\mathrm{rank}(\mathbf{A}) = s - 1$ and the degree of the numerator and denominator polynomials in (A.8) is $s - 1$. The L-stability condition therefore corresponds to a zero-coefficient for the leading term in the numerator polynomial.

A.1.3 Continuous extensions

The ability to efficiently compute an approximation to the DAE (A.1) between mesh points, $\mathbf{u}(t_n + \theta h)$ for $\theta \in [0,\ 1]$, is important for hybrid systems with discrete events as well as for generating dense output for plotting and visualization purposes. This can be accomplished by exploiting the *continuous extension* (Enright et al., 1986) of Runge-Kutta methods. The continuous extension, $\bar{\mathbf{u}}(t_n + \theta h)$, is computed as

$$\bar{\mathbf{u}}(t_n + \theta h) = \mathbf{u}_n + h\sum_{i=1}^{s} b_i^*(\theta)\mathbf{f}(t_n + c_i h, \mathbf{U}_i), \tag{A.9}$$

in which the quadrature weights, b_i^*, depend in θ according to

$$b_i^*(\theta) = b_{i,1}^*\theta + b_{i,2}^*\theta^2 + \ldots + b_{i,p}^*\theta^q. \tag{A.10}$$

We refer to Paper I in Chapter 5 for a discussion of the continuous extension in the discrete event algorithm and the application to phase change location. We

note that the continuous extension is also used as stage value predictor for the nonlinear iterations in the internal Runge-Kutta stages.

The coefficients for the continuous extension can be determined by requiring the same set of order conditions satisfied, which were used to determine the coefficients of the actual method. If we let $\mathbf{b}_i^* = [b_{1,i}^* \; b_{2,i}^* \; \cdots \; b_{s,i}^*]^T$ denote the vector of coefficients for the ith order term in (A.10), then the quadrature weights in (A.9) are given by

$$\mathbf{b}^*(\theta) = \mathbf{b}_1^*\theta + \mathbf{b}_2^*\theta^2 + \ldots + \mathbf{b}_q^*\theta^q. \tag{A.11}$$

For a fourth order continuous extension ($q = 4$) the coefficients in (A.11) can be obtained as the solution to the following linear system of equations

$$\begin{bmatrix} (\mathbf{e})^T \\ (\mathbf{Ce})^T \\ (\mathbf{C}^2\mathbf{e})^T \\ (\mathbf{ACe})^T \\ (\mathbf{C}^3\mathbf{e})^T \\ (\mathbf{CACe})^T \\ (\mathbf{AC}^2\mathbf{e})^T \\ (\mathbf{A}^2\mathbf{Ce})^T \end{bmatrix} \cdot \begin{bmatrix} \mathbf{b}_1^* & \mathbf{b}_2^* & \mathbf{b}_3^* & \mathbf{b}_4^* \end{bmatrix} = \begin{bmatrix} 1 & 0 & 0 & 0 \\ 0 & \frac{1}{2} & 0 & 0 \\ 0 & 0 & \frac{1}{3} & 0 \\ 0 & 0 & \frac{1}{6} & 0 \\ 0 & 0 & 0 & \frac{1}{4} \\ 0 & 0 & 0 & \frac{1}{8} \\ 0 & 0 & 0 & \frac{1}{16} \\ 0 & 0 & 0 & \frac{1}{24} \end{bmatrix} \tag{A.12}$$

The rows of the coefficient matrix in (A.12) are not linearly independent, and the coefficents for the continuous extension are, hence, not uniquely determined, depending on the number of stages of the integration scheme, s. Additional conditions can be imposed, requiring, for example, that the continuous extension matches the numerical solution at mesh points as well as at the internal nodes of the stages

$$\bar{\mathbf{u}}(t_n + c_i h) = \mathbf{U}_i, \qquad i = 1, \ldots, s. \tag{A.13}$$

A.2 A family of ESDIRK methods

A general Butcher tableau for an s-stage, stiffly accurate ESDIRK method is

$$\begin{array}{c|cccccc} 0 & 0 & 0 & & & & \\ c_2 & a_{21} & \gamma & 0 & & & \\ c_3 & a_{31} & a_{32} & \gamma & 0 & & \\ \vdots & \vdots & \vdots & \ddots & \ddots & \ddots & \\ c_{s-1} & a_{s-1,1} & a_{s-1,2} & a_{s-1,3} & \cdots & \gamma & 0 \\ 1 & b_1 & b_2 & b_3 & \cdots & b_{s-1} & \gamma \\ \hline \mathbf{u}_{n+1} & b_1 & b_2 & b_3 & \cdots & b_{s-1} & \gamma \\ \hline \mathbf{e}_{n+1} & d_1 & d_2 & d_3 & \cdots & d_{s-1} & d_s \end{array} . \tag{A.14}$$

		Advancing method				Embedded method			
Method	s	p	A-S.	L-S.	Stiff. acc.	$\hat{p}$	A-S.	L-S.	Stiff. acc.
ESDIRK21	2	2	Yes	No	Yes	1	No	No	No
ESDIRK23	3	2	Yes	Yes	Yes	3	No	No	No
ESDIRK34	4	3	Yes	Yes	Yes	4	No	No	No
ESDIRK45	7	4	Yes	Yes	Yes	5	Yes	No	Yes

Table A.1: Overview of properties of the derived ESDIRK methods. s denotes the number of stages and p and $\hat{p}$ denote the order of the advancing and embedded methods, respectively. All methods have stage order 2. A-S.: A-stable. L-S.: L-stable. Stiff. acc.: stiffly accurate.

The classical order conditions (A.5), stage order conditions (A.6), and the desired stability properties jointly define the conditions needed to determine the coefficients of the Butcher tableau for the individual ESDIRK methods. As a final design requirement we include the condition that all the quadrature nodes lie within the integration step, i.e.

$$t_n \leq t_n + c_i h \leq t_n + h, \qquad i = 1, \ldots, s. \tag{A.15}$$

This is a reasonable condition for one-step methods and particularly important for discrete event problems, where otherwise discrete changes may be triggered if the system is evaluated outside the current integration step.

Stiffly accurate, A- and L-stable ESDIRK methods of orders up to four have been derived. The order and stability conditions were solved using the mathematical software package Maple. We give in this section a complete list of coefficients for all methods including their error estimators and continuous extensions. In cases, where the order and stability conditions do not determine the coefficient uniquely, we comment on the choices made. We denote by ESDIRK$p, \hat{p}$ an ESDIRK method of order p with embedded method of order $\hat{p}$. The ESDIRK methods and their properties are summarized in Table A.1.

ESDIRK21

The lowest order ESDIRK method is the Implicit Euler scheme, which is both A- and L-stable and has one implicit stage. With one implicit stage we can also construct a second order method (the Trapezoidal method) and use the implicit Euler method as error estimator, which results in the following sheme

$$\begin{array}{c|cc} 0 & 0 & 0 \\ 1 & 1/2 & 1/2 \\ \hline \mathbf{u}_{n+1} & 1/2 & 1/2 \\ \hline \mathbf{e}_{n+1} & 1/2 & -1/2 \end{array}. \tag{A.16}$$

ESDIRK21 is the only method, where the advancing method is not L-stable and where the solution is advanced with the higher order approximation. The

c_2	0.58578643762690	b^*_{11}	1.00000000000000
a_{21}	0.29289321881345	b^*_{21}	0.00000000000000
γ	0.29289321881345	b^*_{31}	0.00000000000000
b_1	0.35355339059327	b^*_{12}	-1.35355339059328
b_2	0.35355339059327	b^*_{22}	0.56903559372885
d_1	-0.13807118745770	b^*_{32}	2.06066017177981
d_2	0.33333333333333	b^*_{13}	-1.37377344785321
d_3	-0.19526214587563	b^*_{23}	-0.70710678118653
	.	b^*_{33}	0.80473785412436

Table A.2: ESDIRK23 coefficients for advancing method, error estimator, and continuous extension.

coefficients for a second order continuous extension are

$$\begin{bmatrix}\mathbf{b}^*_1 & \mathbf{b}^*_2\end{bmatrix} = \begin{bmatrix}1 & -1/2 \\ 0 & 1/2\end{bmatrix}. \tag{A.17}$$

ESDIRK23

With three stages (two implicit) we can construct a second order A- and L-stable method with a third order embedded error estimator. The coefficients are uniquely determined by the order and stability conditions. They are given in Table A.2 along with coefficients for a third order continuous extension.

ESDIRK34

As for ESDIRK23, the order and stability conditions determine the coefficients uniquely for a four-stage, third order method with embedded fourth order error estimator. There are several degress of freedom in the construction of a third order continuous extension. In addition to order conditions, the coefficients given in Table A.3 satisfy $\bar{\mathbf{u}}(t_n + h) = \mathbf{U}_4 = \mathbf{u}_{n+1}$.

ESDIRK45

For this method only the continuous extension was derived as part of this work. The basic method and error estimator were originally published by Kværnø (2004). The advancing method and error estimator satisfy fourth and fifth order conditions, respectively. Coefficients are given in Tables A.4 and A.5.

c_2	0.87173304301692	b_{11}^*	0.92716600367945
c_3	0.46823874485184	b_{21}^*	-0.65894519150133
a_{21}	0.43586652150846	b_{31}^*	0.29591266631342
a_{31}	0.14073777472471	b_{41}^*	0.43586652150846
a_{32}	-0.10836555138132	b_{12}^*	-1.64140141649749
γ	0.43586652150846	b_{22}^*	-0.66560479362449
b_1	0.10239940061991	b_{32}^*	2.30700621012198
b_2	-0.37687845225556	b_{42}^*	0.00000000000000
b_3	0.83861253012719	b_{13}^*	0.81663481343795
d_1	0.05462549724041	b_{23}^*	0.94767153287026
d_2	0.49420889362599	b_{33}^*	-1.76430634630822
d_3	-0.22193449973506	b_{43}^*	0.00000000000000
d_4	-0.32689989113134		.

Table A.3: ESDIRK34 coefficients for advancing method, error estimator, and continuous extension.

c_2	0. 52000000000000	a_{51}	0. 16648564323248	b_2	0. 00000000000000
c_3	1. 23033320996791	a_{52}	0. 10450018841592	b_3	-0. 05496908796538
c_4	0. 89576598435008	a_{53}	0. 03631482272099	b_4	-0. 04118626728321
c_5	0. 43639360985865	a_{54}	-0. 13090704451074	b_5	0. 62993304899016
c_6	1. 00000000000000	a_{61}	0. 13855640231268	b_6	0. 06962479448203
a_{21}	0. 26000000000000	a_{62}	0. 00000000000000	d_1	-0. 00195889053628
a_{31}	0. 13000000000000	a_{63}	-0. 04245337201752	d_2	0. 00000000000000
a_{32}	0. 84033320996791	a_{64}	0. 02446657898003	d_3	-0. 01251571594786
a_{41}	0. 22371961478321	a_{65}	0. 61943039072481	d_4	-0. 06565284626324
a_{42}	0. 47675532319800	γ	0. 26000000000000	d_5	0. 01050265826536
a_{43}	-0. 06470895363113	b_1	0. 13659751177640	d_6	-0. 19037520551797
	.		.	d_7	0. 26000000000000

Table A.4: ESDIRK45 coefficients for advancing method and error estimator.

$\mathbf{b}_1^*$	$\mathbf{b}_2^*$	$\mathbf{b}_3^*$	$\mathbf{b}_4^*$
1. 00000000000000	-2. 11033010334339	0. 00000000000000	2. 14420720133310
0. 00000000000000	0. 00000000000000	0. 00000000000000	0. 00000000000000
0. 00000000000000	0. 59806632203087	0. 00000000000000	-1. 27316010934713
0. 00000000000000	-1. 94997165281239	0. 00000000000000	4. 23736963094436
0. 00000000000000	3. 46223543412491	0. 00000000000000	-5. 10841672293033
0. 00000000000000	0. 00000000000000	1. 00000000000000	-1. 50000000000000
0. 00000000000000	0. 00000000000000	0. 00000000000000	0. 00000000000000

Table A.5: ESDIRK45 coefficients for fourth order continuous extension.

Appendix B

Simulation input data

In this appendix we list simulation input data for the component and reaction models used in this thesis.

B.1 The minimal model

The components in the model are light oil (LO), heavy oil (HO), coke (C), oxygen (O_2), water (W) and inert gas (IG). The reactions are

$$\begin{aligned} \mathrm{LO} + \mathrm{O_2} &\rightarrow \mathrm{IG} + \mathrm{W} \\ \mathrm{HO} + \mathrm{O_2} &\rightarrow \mathrm{IG} + \mathrm{W} \\ \mathrm{HO} &\rightarrow \mathrm{LO} + \mathrm{C} + \mathrm{IG} \\ \mathrm{C} + \mathrm{O_2} &\rightarrow \mathrm{IG} + \mathrm{W}. \end{aligned} \tag{B.1}$$

Tube length	0.807 m	Rock thermal conduc.	1.731 $^{\mathrm{J}}/_{\mathrm{s\cdot K\cdot m}}$
Tube diameter	0.055 m	Solid thermal conduc.	1.731 $^{\mathrm{J}}/_{\mathrm{s\cdot K\cdot m}}$
Rock porosity	0.4142	Oil thermal conduc.	0.133 $^{\mathrm{J}}/_{\mathrm{s\cdot K\cdot m}}$
Rock permeability	12700 mDa	Water thermal conduc.	0.623 $^{\mathrm{J}}/_{\mathrm{s\cdot K\cdot m}}$
Rock C_v^1	2348.3 $^{\mathrm{kJ}}/_{\mathrm{m^3\cdot K}}$	Gas thermal conduc.	0.144 $^{\mathrm{J}}/_{\mathrm{s\cdot K\cdot m}}$
Rock C_v^2	0.0		

Table B.1: Rock (homogeneous) and phase properties for the minimal model. Rock heat capacity correlation: $C_v[^{\mathrm{kJ}}/_{\mathrm{m^3\cdot K}}] = C_v^1 + C_v^2 \cdot T$.

Comp.	Phase(s)	M_i [kg/mole]	$\xi_{i,ref}$ [mole/m^3]	c_i^p [atm^{-1}]	c_i^t [K^{-1}]
LO	o/g	0.157	5118	$7.35 \cdot 10^{-5}$	$5.11 \cdot 10^{-4}$
HO	o/g	0.675	1464	$7.35 \cdot 10^{-5}$	$2.68 \cdot 10^{-4}$
O2	o/g	0.032	95277	–	–
IG	o/g	0.041	95277	–	–
H2O	w/g	0.018	55520	$4.41 \cdot 10^{-5}$	$2.16 \cdot 10^{-4}$
Coke	s	0.013	70488	–	–

Table B.2: Component data for the minimal model. M_i: molar weight. $\xi_{i,ref}$: liquid density at reference conditions. c_i^p: liquid compressibility. c_i^t: thermal expansivity.

Comp.	T_i^{crit} [K]	P_i^{crit} [atm]	ω_i
LO	617.4	20.8	0.449
HO	887.6	8.2	1.589
O2	154.8	49.7	0.022
IG	126.5	34.0	0.040
H2O	647.4	214.7	0.344

Table B.3: Critical data for the minimal model. T_i^{crit}: critical temperature. P_i^{crit}: critical pressure. ω_i: accentric factor. Binary interaction coefficients are assumed to be zero.

Comp.	C_p^1	C_p^2	C_p^3	C_p^4
LO	-7.913	0.961	$-5.290 \cdot 10^{-4}$	$1.123 \cdot 10^{-7}$
HO	-34.081	4.137	$-2.279 \cdot 10^{-3}$	$4.835 \cdot 10^{-7}$
O2	28.106	$-3.680 \cdot 10^{-6}$	$1.746 \cdot 10^{-5}$	$-1.065 \cdot 10^{-8}$
IG	31.150	$-1.357 \cdot 10^{-2}$	$2.679 \cdot 10^{-5}$	$-1.167 \cdot 10^{-8}$
H2O	7.701	$4.595 \cdot 10^{-4}$	$2.521 \cdot 10^{-6}$	$-0.859 \cdot 10^{-9}$
Comp.	a_i^g	b_i^g	a_i^l	b_i^l
LO	$3.770 \cdot 10{-}6$	0.943	$4.02 \cdot 10{-}4$	3400.89
HO	$7.503 \cdot 10{-}6$	1.102	$4.02 \cdot 10{-}4$	3400.89
O2	$3.355 \cdot 10{-}4$	0.721	.	.
IG	$3.213 \cdot 10{-}4$	0.702	.	.
H2O	$1.700 \cdot 10{-}5$	1.116	$7.52 \cdot 10{-}5$	1384.86

Table B.4: Heat capacity and viscosity data for the minimal model. Heat capacity correlation: $C_p[\text{J/mole·K}] = C_p^1 + C_p^2 T + C_p^3 T^2 + C_p^4 T^3$ (T in [K]). Solid phase heat capacity: 16.0 J/mole·K (constant). Liquid viscosity correlation: $\mu_i^l[cP] = a_i^l \exp(b_i^l/T)$. Gas viscosity correlation: $\mu_i^g[cP] = a_i^g T^{b_i^g}$.

	LO oxidation	HO oxidation	HO cracking	Coke oxidation
LO	−1.	0.	2.154	0.
HO	0.	−1.	−1.	0.
O2	−14.06	−60.55	0.	−1.18
IG	11.96	51.53	0.	1.
H2O	6.58	28.34	0.	0.55
Coke	0.	0.	25.96	−1.

Table B.5: Stoichiometric coefficients for the minimal reaction model.

Reaction	m_γ	n_γ	E_a^γ [kJ/mole]	α_γ	ΔH_γ^r [kJ/mole]
LO oxidation	1	1	138.281	$4.4394 \cdot 10^{11}$	6762.5
HO oxidation	1	1	138.281	$4.4394 \cdot 10^{11}$	29133.2
HO cracking	1	–	62.802	$4.1670 \cdot 10^{5}$	93.0
Coke oxidation	1	1	58.615	$6.1238 \cdot 10^{3}$	523.4

Table B.6: Reaction kinetic data for the minimal reaction model. m_γ: reaction order in component concentration. n_γ: reaction order in oxygen partial pressure. E_a^γ: activation energy. α_γ: frequency factor. ΔH_γ^r: reaction enthalpy.

B.2 The SARA model

$$
\begin{array}{ll}
\text{cracking/} & \begin{cases} \text{Asph} \rightarrow \text{H}_2\text{O} + \text{Arom} + \text{Sat} + \text{Lites} + \text{PyrCoke} \\ \text{Resins} \rightarrow \text{H}_2\text{O} + \text{Asph} + \text{Arom} + \text{Sat} + \text{Lites} \\ \text{Arom} \rightarrow \text{Asph} + \text{Lites} \end{cases} \\
\text{pyrolysis} & \\
\text{LTO} & \begin{cases} \text{Asph} + \text{O}_2 \rightarrow \text{H}_2\text{O} + \text{CO}_2 + \text{OxdAsph} \\ \text{Resins} + \text{O}_2 \rightarrow \text{H}_2\text{O} + \text{CO}_2 + \text{OxdResAr} \\ \text{Arom} + \text{O}_2 \rightarrow \text{H}_2\text{O} + \text{CO}_2 + \text{OxdResAr} \\ \text{Sat} + \text{O}_2 \rightarrow \text{H}_2\text{O} + \text{CO}_2 + \text{OxdSat} \end{cases} \\
\text{HTO} & \begin{cases} \text{PyrCoke} + \text{O}_2 \rightarrow \text{H}_2\text{O} + \text{CO}_2 \\ \text{OxdAsph} + \text{O}_2 \rightarrow \text{H}_2\text{O} + \text{CO}_2 \\ \text{OxdResAr} + \text{O}_2 \rightarrow \text{H}_2\text{O} + \text{CO}_2 \\ \text{OxdSat} + \text{O}_2 \rightarrow \text{H}_2\text{O} + \text{CO}_2 \\ \text{Asph} + \text{O}_2 \rightarrow \text{H}_2\text{O} + \text{CO}_2 \\ \text{Resins} + \text{O}_2 \rightarrow \text{H}_2\text{O} + \text{CO}_2 \\ \text{Arom} + \text{O}_2 \rightarrow \text{H}_2\text{O} + \text{CO}_2. \end{cases}
\end{array}
\tag{B.2}
$$

Component Name	Abbreviation
Water	H_2O
Inert oil	InertOil
Oxidized resins/aromatics	OxdResAr
Oxidized saturates	OxdSat
Asphaltenes	Asph
Resins	Resins
Aromatics	Arom
Saturates	Sat
Light oil	Lites
Carbon dioxide	CO_2
Nitrogen	N_2
Oxygen	O_2
Oxidized asphaltenes	OxdAsph
Pyrolysis coke	PyrCoke

Table B.7: List of (pseudo) components for the SARA model.

Comp.	Phase(s)	M_i [kg/mole]	$\xi_{i,ref}$ [mole/m^3]	c_i^p [atm^{-1}]	c_i^t [K^{-1}]
InertOil	o/g	0.010	95277	$7.09 \cdot 10^{-5}$	$7.00 \cdot 10^{-4}$
OxdResAr	o/g	0.475	2422	$7.09 \cdot 10^{-5}$	$6.50 \cdot 10^{-4}$
OxdSat	o/g	0.166	6631	$7.09 \cdot 10^{-5}$	$6.50 \cdot 10^{-4}$
ASPH	o/g	1.443	811	$7.09 \cdot 10^{-5}$	$6.32 \cdot 10^{-4}$
RESINS	o/g	0.875	1205	$7.09 \cdot 10^{-5}$	$6.60 \cdot 10^{-4}$
AROM	o/g	0.444	2218	$7.09 \cdot 10^{-5}$	$6.53 \cdot 10^{-4}$
SAT	o/g	0.298	2915	$7.09 \cdot 10^{-5}$	$7.45 \cdot 10^{-4}$
Lites	o/g	0.172	4926	$7.09 \cdot 10^{-5}$	$9.10 \cdot 10^{-4}$
CO2	o/g	0.044	22159	$7.09 \cdot 10^{-5}$	$4.34 \cdot 10^{-4}$
N2	o/g	0.028	95277	–	–
O2	o/g	0.032	95277	–	–
H2O	w/g	0.018	55344	$4.41 \cdot 10^{-5}$	$2.16 \cdot 10^{-4}$
OxdAsph	s	0.047	23163	–	–
PyrCoke	s	0.013	70488	–	–

Table B.8: Component data for the SARA model. M_i: molar weight. $\xi_{i,ref}$: liquid density at reference conditions. c_i^p: liquid compressibility. c_i^t: thermal expansivity.

Tube length	1.623 m	Rock thermal conduc.	1.731 $^{J}/_{s\cdot K\cdot m}$
Tube diameter	0.054 m	Solid thermal conduc.	0.250 $^{J}/_{s\cdot K\cdot m}$
Rock porosity	0.4037	Oil thermal conduc.	0.133 $^{J}/_{s\cdot K\cdot m}$
Rock permeability	594 mDa	Water thermal conduc.	0.669 $^{J}/_{s\cdot K\cdot m}$
Rock C_v^1	1487 $^{kJ}/_{m^3\cdot K}$	Gas thermal conduc.	0.042 $^{J}/_{s\cdot K\cdot m}$
Rock C_v^2	2.15 $^{kJ}/_{m^3\cdot K^2}$		

Table B.9: Rock (homogeneous) and phase properties for the SARA model. Rock heat capacity correlation: $C_v[^{kJ}/_{m^3\cdot K}] = C_v^1 + C_v^2 \cdot T$.

Comp.	a_i^g	b_i^g	Comp.	a_i^g	b_i^g
InertOil	$1.00 \cdot 10^{-3}$	0.500	SAT	$2.46 \cdot 10^{-4}$	0.491
OxdResAr	$2.46 \cdot 10^{-4}$	0.466	Lites	$2.61 \cdot 10^{-5}$	0.896
OxdSat	$2.46 \cdot 10^{-4}$	0.466	CO2	$1.59 \cdot 10^{-4}$	0.798
ASPH	$2.46 \cdot 10^{-4}$	0.466	N2	$2.33 \cdot 10^{-3}$	0.347
RESINS	$2.46 \cdot 10^{-4}$	0.466	O2	$2.87 \cdot 10^{-3}$	0.338
AROM	$2.46 \cdot 10^{-4}$	0.466	H2O	$9.35 \cdot 10^{-6}$	1.209

Table B.10: Viscosity data for the SARA model. Standard literature values are used for the chemical component (CO2, N2, O2 and H20) heat capacities. Pseudo component heat capacities: $C_p = 2.1^{J}/_{mole\cdot K}$ (constant). Solid phase heat capacity: $16.0\,^{J}/_{mole\cdot K}$ (constant). Liquid viscosities are obtained from tables (not presented here). Gas viscosity correlation: $\mu_i^g[cP] = a_i^g T^{b_i^g}$.

Comp.	T_i^{crit} [K]	P_i^{crit} [atm]	ω_i
InertOil	499.2	83.7	0.184
OxdResAr	1000.2	21.6	0.778
OxdSat	856.6	29.6	0.487
ASPH	1155.2	14.3	1.099
RESINS	1067.2	11.7	1.143
AROM	930.5	14.8	0.929
SAT	809.8	13.5	0.792
Lites	699.4	22.8	0.465
CO2	304.2	72.9	0.224
N2	126.2	33.5	0.040
O2	154.8	49.7	0.022
H2O	647.4	214.7	0.344

Table B.11: Critical data for the SARA model. T_i^{crit}: critical temperature. P_i^{crit}: critical pressure. ω_i: accentric factor.

0.0000	0.0321	0.0172	0.0512	0.0533	0.0422	0.0412	0.0209	0	0	0
	0.0000	0.0029	0.0034	0.0042	0.0010	0.0008	0.0015	0	0	0
		0.0000	0.0122	0.0135	0.0072	0.0067	0.0002	0	0	0
			0.0000	0.0000	0.0007	0.0009	0.0094	0	0	0
				0.0000	0.0011	0.0013	0.0105	0	0	0
					0.0000	0.0000	0.0050	0	0	0
						0.0000	0.0046	0	0	0
							0.0000	0	0	0
								0	0	0
									0	0
										0

Table B.12: Binary interaction coefficients for the SARA model. The coefficients are estimated from Twu's correlations (Twu, 1984).

Reaction	m_γ	n_γ	E_a^γ [kJ/mole]	α_γ	ΔH_γ^r [kJ/mole]
ASPH crac.	1	–	222.000	$2.0100{\cdot}10^{17}$	0.0
RESINS crac.	1	–	184.450	$6.2000{\cdot}10^{13}$	0.0
AROM crac.	1	–	184.450	$3.1000{\cdot}10^{13}$	0.0
ASPH LTO	1	1	75.160	$6.2689{\cdot}10^{3}$	43932.7
RESINS LTO	1	0.7	78.600	$6.2393{\cdot}10^{4}$	21681.2
AROM LTO	1	0.7	105.170	$1.0106{\cdot}10^{8}$	9371.9
SAT LTO	1	0.7	78.604	$6.0005{\cdot}10^{7}$	10729.2
Coke HTO	1	1	68.405	$9.2968{\cdot}10^{3}$	28067.1
OxdAsph HTO	1	1	68.405	$9.2968{\cdot}10^{3}$	7881.1
OxdResAr HTO	1	1	68.405	$9.2968{\cdot}10^{3}$	9622.8
OxdSat HTO	1	1	68.405	$9.2968{\cdot}10^{2}$	3555.6
ASPH HTO	1	1	68.405	$9.2968{\cdot}10^{1}$	51813.8
RESINS HTO	1	1	68.405	$9.2968{\cdot}10^{1}$	34896.0
AROM HTO	1	1	68.405	$9.2968{\cdot}10^{1}$	18994.6

Table B.13: Reaction kinetic data for the SARA reaction model. m_γ: reaction order in component concentration. n_γ: reaction order in oxygen partial pressure. E_a^γ: activation energy. α_γ: frequency factor. ΔH_γ^r: reaction enthalpy.

	ASPH crac.	RESINS crac.	AROM crac.	ASPH LTO	RESINS LTO	AROM LTO	SAT LTO
InertOil	0.	0.	0.	0.	0.	0.	0.
OxdResAr	0.	0.	0.	0.	1.37	1.	0.
OxdSat	0.	0.	0.	0.	0.	0.	1.
ASPH	−1.	0.17	0.06	−1.	0.	0.	0.
RESINS	0.	−1.	0.	0.	−1.	0.	0.
AROM	0.18	0.59	−1.	0.	0.	−1.	0.
SAT	0.54	0.63	0.	0.	0.	0.	−1.
Lites	0.19	0.79	1.81	0.	0.	0.	0.
CO2	0.	0.	0.	63.50	25.80	7.02	10.65
N2	0.	0.	0.	0.	0.	0.	0.
O2	0.	0.	0.	−91.66	−48.62	−18.25	−18.71
H2O	0.55	0.48	0.	43.87	29.97	12.75	14.54
OxdAsph	0.	0.	0.	1.	0.	0.	0.
PyrCoke	1.43	0.	0.	0.	0.	0.	0.
	Coke HTO	OxdAsph HTO	OxdResAr HTO	OxdSat HTO	ASPH HTO	RESINS HTO	AROM HTO
InertOil	0.	0.	0.	0.	0.	0.	0.
OxdResAr	0.	0.	−1.	0.	0.	0.	0.
OxdSat	0.	0.	0.	−1.	0.	0.	0.
ASPH	0.	0.	0.	0.	−1.	0.	0.
RESINS	0.	0.	0.	0.	0.	−1.	0.
AROM	0.	0.	0.	0.	0.	0.	−1.
SAT	0.	0.	0.	0.	0.	0.	0.
Lites	0.	0.	0.	0.	0.	0.	0.
CO2	54.89	36.50	24.90	10.65	100.	60.	31.93
N2	0.	0.	0.	0.	0.	0.	0.
O2	−68.30	−41.92	−26.01	−12.96	−133.58	−84.34	−44.27
H2O	21.54	15.70	10.72	6.22	59.56	44.68	23.47
OxdAsph	0.	−1.	0.	0.	0.	0.	0.
PyrCoke	−1.	0.	0.	0.	0.	0.	0.

Table B.14: Stoichiometric coefficients for the SARA reaction model.

Nomenclature

Physical quantities

Symbol	Description	SI Units
C_i	Overall molar concentration of component i	$^{\text{mole}}/_{\text{m}^3}$
c_i^j	Molar concentration of component i in phase j	$^{\text{mole}}/_{\text{m}^3}$
c_i^p	Liquid compressibility of component i	Pa^{-1}
c_i^t	Thermal expansivity of component i	K^{-1}
D	Reservoir depth	m
E_a^γ	Activation energy for reaction γ	$^{\text{J}}/_{\text{mole}}$
f_i^j	Fugacity of component i in phase j	Pa
g	Gravitational acceleration	$^{\text{m}}/_{\text{s}^2}$
h	Formation thickness	m
h^j	Molar enthalpy of phase j	$^{\text{J}}/_{\text{mole}}$
$\mathbf{k}$	Absolute permeability (tensor)	m^2
$\mathbf{k}_c$	Effective thermal conductivity (tensor)	$^{\text{J}}/_{\text{m}\cdot\text{s}\cdot\text{K}}$
k_c^j	Thermal conductivity of phase j	$^{\text{J}}/_{\text{m}\cdot\text{s}\cdot\text{K}}$
$\mathbf{k}_c^r$	Thermal conductivity of rock (tensor)	$^{\text{J}}/_{\text{m}\cdot\text{s}\cdot\text{K}}$
k_r^j	Relative permeability of phase j	–
k_v	Valve coefficient in kinetic cell model	$^{\text{m}^3}/_{\text{Pa}\cdot\text{s}}$
K_i	Equilibrium K-value for component i	–
K_γ	Rate constant for reaction γ	–
L	Length of 1D domain	m
M_i	Molecular weight of component i	$^{\text{kg}}/_{\text{mole}}$
P	Pressure	Pa
P_i^{crit}	Component critical pressure	Pa
$\mathbf{q}_i^m$	Molar flux of component i	$^{\text{mole}}/_{\text{m}^2\cdot\text{s}}$
$\mathbf{q}^{h,adv}$	Heat flux due to advection	$^{\text{J}}/_{\text{m}^2\cdot\text{s}}$

Symbol	Description	SI Units
$\mathbf{q}^{h,cond}$	Heat flux due to conduction	$^{J}/_{m^2 \cdot s}$
$Q_i^{m,reac/well}$	Molar source density due to chemical reactions/wells	$^{mole}/_{m^3 \cdot s}$
$Q^{h,reac/well}$	Heat source density due to chemical reactions/wells	$^{J}/_{m^3 \cdot s}$
r_0	Pressure equivalent radius	m
r_w	Well radius	m
R_γ	Reaction rate for reaction γ	$^{mole}/_{m^3 \cdot s}$
R_g	Universal gas constant	$^{J}/_{mole \cdot K}$
s	Skin factor in well equation	–
S^j	Volumetric saturation of phase j	–
t	Time	s
T	Temperature	K
T_i^{crit}	Component critical temperature	K
T^{ext}	Set point for temperature controller	K
u_a	Heat transfer coefficient (controller gain)	$^{J}/_{s \cdot K}$
$\mathbf{u}^j$	Flow velocity og phase j	$^{m}/_{s}$
U^j	Molar internal energy of phase j	$^{J}/_{mole}$
U^r	Volumetric internal energy of rock	$^{J}/_{m^3}$
V^j	Volume of phase j	m^3
V_p	Void pore volume	m^3
V_T	Total bulk volume	m^3
x_i^j	Mole fraction of component i in phase j	–
z_i	Overall mole fraction of component i	–
Z^j	Compressibility of phase j	–
α_γ	Frequency factor for reaction γ	–
β^j	Molar phase fraction of phase j	–
μ^j	Viscosity of phase j	$Pa \cdot s$
ξ^j	Molar density of phase j	$^{mole}/_{m^3}$
ρ^j	Mass density of phase j	$^{kg}/_{m^3}$
ϕ_f	Fluid porosity	–
ϕ_v	Void porosity	–
φ_i^j	Fugacity coefficient for component i in phase j	–
ω_i	Accentric factor for component i	–

Indexing labels

Index	Set	Description	Size
i	$\mathcal{I}$	Chemical pseudocomponents	n_c
i	$\mathcal{I}^{ol}$	Oleic pseudocomponents	n_{ol}
i	$\mathcal{I}^{w}$	Water component	1
i	$\mathcal{I}^{s}$	Solid pseudocomponents	n_s
γ	$\mathcal{I}^{rx}$	Chemical reactions	n_r
w	$\mathcal{I}_w$	Wells	n_w
w	$\mathcal{I}_w^{inj}$	Injections wells	n_w^{inj}
w	$\mathcal{I}_w^{prod}$	Production wells	n_w^{prod}

Commonly used abbreviations

ADS	Additive Splitting
AIM	Adaptive Implicit Method
AMR	Adaptive Mesh Refinement
CFL	Courant-Friedrichs-Lewy
DAE	Differential Algebraic Equation
DIRK	Diagonally Implicit Runge-Kutta
EOR	Enhanced Oil Recovery
EoS	Equation-of-State
ESDIRK	Explicit Singly Diagonally Implicit Runge-Kutta
FIM	Fully Implicit Method
FIRK	Fully Implicit Runge-Kutta
HPAI	High Pressure Air Injection
IMEX	Implicit-Explicit
IMPEC	Implicit Pressure Explicit Composition
IMPES	Implicit Pressure Explicit Saturation
ISC	In-Situ Combustion
ODE	Ordinary Differential Equation
PDE	Partial Differential Equation
RK	Runge-Kutta
SAGD	Steam Assisted Gravity Drainage
SDIRK	Singly Diagonally Implicit Runge-Kutta
THAI	Toe-to-Heel Air Injection
VCT	Virtual Combustion Tube
VKC	Virtual Kinetic Cell

Bibliography

Adegbesan, K. O., Donnelly, J. K., Moore, R. G. and Bennion, D. W. (1987), Low-temperature-oxidation kinetic parameters for in-situ combustion: Numerical simulation, Society of Petroleum Engineers. SPE 12004: Presented at the 58th Annual Technical Conference and Exhibition, San Francisco, CA, October 5-8.

Akkutlu, I. Y. and Yortsos, Y. C. (2002), The effect of heterogeneity on in-situ combustion: The propagation of combustion fronts in layered porous media, Society of Petroleum Engineers. SPE 75128: Presented at the SPE/DOE Thirteenth Improved Oil Recovery Symposium,Tulsa, OK, 13-17 April.

Akkutlu, I. Y. and Yortsos, Y. C. (2003), 'The dynamics of in-situ combustion fronts in porous media', *Combustion and Flame* **134**, 229–247.

Akkutlu, I. Y. and Yortsos, Y. C. (2004), Steady-state propagation of in-situ combustion fronts with sequential reactions, Society of Petroleum Engineers. SPE 91957: Presented at the 2004 SPE International Petroleum Conference, Puebla, Mexico, 8-9 November.

Aldushin, A. P., Matkowsky, B. J. and Schult, D. A. (1997), 'Buoyancy driven filtration combustion', *Combustion Science and Technology* **125**, 283–349.

Alexander, R. (2003), 'Design and implementation of DIRK integrators for stiff systems', *Applied Numerical Mathematics* **46**, 1–17.

Arbogast, T., Bryant, S., Dawson, C., Saaf, F., Wang, C. and Wheeler, M. (1996), 'Computational methods for multiphase flow and transport problems arising in subsurface contaminant remediation', *Journal of Computational and Applied Mathematics* **74**, 19–32.

Aris, R. (1989), *Elementary Chemical Reactor Analysis*, Dover Publication, Inc., Mineola, New York.

Aziz, K. and Settari, A. (1979), *Petroleum Reservoir Simulation*, Elsevier Applied Science Publishers, London.

Bauer, I., Bock, H. G., Körkel, S. and Schlöder, J. P. (2000), 'Numerical methods

for optimum experimental design in DAE systems', *Journal of Computational and Applied Mathematics* **120**, 1–25.

Bijl, H., Carpenter, M. H., Vatsa, V. N. and Kennedy, C. A. (2002), 'Implicit time integration schemes for the unsteady compressible navier-stokes equations: Laminar flow', *Journal of Computational Physics* **179**, 313–329.

Butcher, J. C. and Chen, D. J. L. (2000), 'A new type of singly-implicit runge-kutta methods', *Applied Numerical Mathematics* **34**, 179–188.

Butler, R. M., McNab, G. S. and Lo, H. Y. (1981), 'Theoretical studies on the gravity grainage of heavy oil during in-situ steam heating', *Canadian Journal of Chemical Engineering* **59**(4), 455–460.

Cao, H. (2002), Development of techniques for general purpose simulators, PhD thesis, Stanford University, USA.

Castanier, L. M. and Brigham, W. E. (2004), In-situ combustion. Society of Petroleum Engineers Handbook.

Christensen, J. R., Darche, G., Déchelette, B., Ma, H. and Sammon, P. H. (2004), Applications of dynamic gridding to thermal simulations, Society of Petroleum Engineers. SPE 86969: Presented at the SPE International Thermal Operations and Heavy Oil Symposium, Bakersfield, CA., March 16-18.

Christofari, J., Castanier, L. M. and Kovscek, A. R. (2006), Laboratory investigation of the effect of solvent injection on in-situ combustion, Society of Petroleum Engineers. SPE 99752: Presented at 2006 SPE Symposium on Improved Oil Recovery, Tulsa, OK, April 22 - 26.

Clara, C., Durandeau, M., Quenault, G. and Nguyen, T.-H. (2000), 'Laboratory studies for light-oil air injection projects: Potential application in handil field', *SPE Reservoir Evaluation and Engineering* **3**(3), 239–248.

CMG (2004), *STARS, Advanced Process and Thermal Reservoir Simulator*, 2004 edn.

Coats, K. H. (1980), 'In-situ combustion model', *Society of Petroleum Engineers Journal* **269**, 533–554.

Crookston, R. B., Culham, W. E. and Chen, W. H. (1979), 'A numerical simulation model for thermal recovery processes', *Society of Petroleum Engineers Journal* pp. 37–58.

Dabbous, M. K. and Fulton, P. F. (1974), 'Low-temperature-oxidation reaction kinetics and effects on the in-situ combustion process', *Society of Petroleum Engineers Journal* **255**, 253–262. SPE 4143.

Duff, I. S. and Reid, J. K. (1996), 'The design of MA48: A code for the direct solution of sparse unsymmetric linear systems of equations', *ACM Transactions on Mathematical Software* **22**(2), 187–226.

EIA-DOE (2007), International energy outlook 2007, Technical report, Energy Information Administration, U.S. Department of Energy.

Enright, W. H., Jackson, K. R., Nørsett, S. P. and Thomsen, P. G. (1986), 'Interpolants for runge-kutta formulas', *ACM Transactions on Mathematical Software* **12**(3), 193–218.

Farouq Ali, S. M. (1977), Multiphase, multidimensional simulation of in-situ

combustion, Society of Petroleum Engineers. SPE 6896: Presented at the 52nd SPE Annual Fall Technical Conference and Exhibition, Denver, Colorado, Oct. 9-12.

Fassihi, M. R., Brigham, W. E. and Ramey Jr., H. J. (1984*a*), 'Reaction kinetics of in-situ combustion: Part 1 - observations', *Society of Petroleum Engineers Journal* pp. 399–407.

Fassihi, M. R., Brigham, W. E. and Ramey Jr., H. J. (1984*b*), 'Reaction kinetics of in-situ combustion: Part 2 - modelling', *Society of Petroleum Engineers Journal* pp. 408–416.

Freitag, N. P. and Exelby, D. R. (2006), 'A SARA-based model for simulating the pyrolysis reactions that occur in high-temperature EOR processes', *Journal of Canadian Petroleum Technology* **45**(3), 38–44.

Freitag, N. P. and Verkoczy, B. (2005), 'Low-temperature oxidation of oils in terms of SARA fractions: Why simple reaction models don't work', *Journal of Canadian Petroleum Technology* **44**(2), 54–61.

Friedly, J. C. (1991), 'Extent of reaction in open systems with multiple heterogeneous reactions', *AIChE Journal* **37**(5), 687–693.

Friedly, J. C. and Rubin, J. (1992), 'Solute transport with multiple equilibrium-controlled or kinetically controlled chemical reactions', *Water Resources Research* **28**(6), 1935–1953.

Gillham, T. H., Cerveny, B. W., Turek, E. A. and Yannimaras, D. V. (1997), Keys to increasing production via air injection in gulf coast light-oil reservoirs, Society of Petroleum Engineers. SPE 38848: Presented at the SPE Annual Technical Conference and Exhibition, San Antonio, TX, October 5-8.

Grabowski, J. W., Vinsome, P. K., Lin, R. C., Behie, A. and Rubin, B. (1979), A fully implicit general purpose finite-difference thermal model for in-situ combustion and steam, Society of Petroleum Engineers. SPE 8396: Presented at the 54th Annual Fall Technical Conference and Exhibition of the SPE, Las Vegas, NV, September 23-26.

Greaves, M., Xia, T. X. and Ayasse, C. (2005), Underground upgrading of heavy oil using thai: "toe-to-heel air injection", Society of Petroleum Engineers. SPE 97728: Presented at 2005 SPE Thermal Operations and Heavy Oil Symposium, Calgary, Canada, November 1 - 3.

Gustafsson, K. (1992), Control of Error and Convergence in ODE Solvers, PhD thesis, Department of Automatic Control, Lund Institute of Technology.

Hairer, E., Nørsett, S. and Wanner, G. (1996), *Solving Ordinary Differential Equations I*, second revised edn, Springer.

Hairer, E. and Wanner, G. (1996), *Solving Ordinary Differential Equations II*, second revised edn, Springer.

Hascoët, L. and Pascual, V. (2004), *Tapenade 2.1 User's Guide*, INRIA, France.

Haukås, J. (2006), Compositional reservoir simulation with emphasis on the IMPSAT formulation, PhD thesis, University of Bergen, Norway.

Hindmarsh, A. C. (1983), ODEPACK, a generalized collection of ODE solvers, *in* R. S. Stepleman, ed., 'Scientific Computing (IMACS Transactions on Sci-

entific Computing, Vol. 1)', North-Holland, Amsterdam, pp. 55–64.

Hundsdorfer, W. and Verwer, J. G. (2003), *Numerical Solution of Time-Dependent Advection-Diffusion-Reaction Equations*, Springer Series in Computational Mathematics, Springer.

Islam, M. R., Chakma, A. and Farouq Ali, S. M. (1989), State-of-the-art of in-situ combustion modelling and operations, Society of Petroleum Engineers. SPE 18755: Presented at the SPE California Regional Meeting, Bakersfield, CA., April 5-7.

Jørgensen, J. B., Kristensen, M. R. and Thomsen, P. G. (2008), 'A familiy of esdirk integration methods', *Submitted to SIAM Journal on Scientific Computing* .

Kennedy, C. A. and Carpenter, M. H. (2003), 'Additive runge-kutta schemes for convection-diffusion-reaction equations', *Applied Numerical Mathematics* **44**, 139–181.

Kräutle, S. and Knabner, P. (2005), 'A new numerical reduction scheme for fully coupled multicomponent transport-reaction problems in porous media', *Water Resources Research* **41**.

Kristensen, M. R. (2008), Development of Models and Algorithms for the Study of Reactive Porous Media Processes, PhD thesis, Technical University of Denmark.

Kristensen, M. R., Gerritsen, M., Thomsen, P. G., Michelsen, M. L. and Stenby, E. H. (2007*a*), Coupling chemical kinetics and flashes in reactive, thermal and compositional reservoir simulation, Society of Petroleum Engineers. SPE 106218: Presented at 2007 SPE Reservoir Simulation Symposium, Houston, TX, February 26 - 28.

Kristensen, M. R., Gerritsen, M., Thomsen, P. G., Michelsen, M. L. and Stenby, E. H. (2007*b*), 'Efficient integration of stiff kinetics with phase change detection for reactive reservoir processes', *Transport in Porous Media* **69**(3), 383–409.

Kumar, V. K., Gutierrez, D., Moore, R. G. and Mehta, S. A. (2007), Case history and appraisal of the west buffalo red river unit high-pressure air injection project, Society of Petroleum Engineers. SPE 107715: Presented at the SPE Hydrocarbons Economics and Evaluation Symposium, Dallas, TX, April 1-3.

Kutta, W. (1901), 'Beitrag zur näherungsweisen integration totaler differentialgleichungen', *Zeitschrift für Mathematik und Physik* **46**, 435–453.

Kværnø, A. (2004), 'Singly diagonally implicit runge-kutta methods with an explicit first stage', *BIT Numerical Mathematics* **44**, 489–502.

Lee, B. I. and Kesler, M. G. (1975), 'A generalized thermodynamic correlation based on three corresponding states', *AIChE Journal* **21**, 510–527.

Michelsen, M. L. (1982), 'The isothermal flash problem. part 1: Stability', *Fluid Phase Equilibria* **9**, 1–19.

Michelsen, M. L. and Mollerup, J. M. (2004), *Thermodynamic Models: Fundamentals and Computational Aspects*, Tie-Line Publications, Holte, Denmark.

Moore, G., Mehta, R. and Ursenbach, M. (2002*a*), 'Air injection for oil recovery',

Journal of Canadian Petroleum Technology **41**(8), 16–19.

Moore, R. G., Laureshen, C. J., Belgrave, J. D. M., Ursenbach, M. G. and Mehta, S. A. (1995), 'In-situ combustion in canadian heavy oil reservoirs', *Fuel* **74**(8), 1169–1175.

Moore, R. G., Laureshen, C. J., Ursenbach, M. G., Mehta, S. A. and Belgrave, J. D. M. (1999), 'Combustion/oxidation behavior of athabasca oil sands bitumen', *SPE Reservoir Evaluation and Engineering* **2**(6), 565 – 572.

Moore, R. G., Mehta, S. A. and Ursenbach, M. G. (2002*b*), A guide to high pressure air injection (HPAI) based oil recovery, Society of Petroleum Engineers. SPE 75207: Presented at the SPE/DOE Improved Oil Recovery Symposium, Tulsa, OK, April 13-17.

Nilsson, J., Gerritsen, M. and Younis, R. (2005), A novel adaptive anisotropic grid framework for efficient reservoir simulation, Society of Petroleum Engineers. SPE 93243: Presented at 2005 SPE Reservoir Simulation Symposium, Houston, TX, January 31 - February 2.

Orr Jr., F. M. (2007), *Theory of Gas Injection Processes*, Tie-Line Publications.

Park, T. and Barton, P. I. (1996), 'State event location in differential-algebraic models', *ACM Transactions on Modeling and Computer Simulation* **6**(2), 137–165.

Pascual, M., Lacentre, P. and Coombe, D. (2005), Air injection into a mature waterflooded light oil reservoir. laboratory and simulation results for barrancas field, argentina, Society of Petroleum Engineers. SPE 94092: Presented at the SPE Europec/EAGE Annual Conference, Madrid, Spain, June 13-16.

Peng, D. Y. and Robinson, D. B. (1976), 'A new two constant equation of state', *Industrial Engineering Chemistry Fundamentals* **15**, 59–64.

Petzold, L. R. (1982), 'DASSL: A differential/algebraic system solver'. 10th IMACS World Congress on System Simulation and Scientific Computation.

Prats, M. (1986), *Thermal Recovery*, Vol. 7 of *SPE Monograph Series*, Society of Petroleum Engineers.

Prothero, A. and Robinson, A. (1974), 'On the stability and accuracy of one-step methods for sloving stiff systems of ordinary differential equations', *Mathematics of Computation* **28**(125), 145–162.

Rasmussen, C. P., Krejbjerg, K., Michelsen, M. L. and Bjurstrøm, K. E. (2006), 'Increasing the computational speed of flash calculations with applications for compositional, transient simulations', *SPE Reservoir Evaluation & Engineering* pp. 32–38.

Ren, Y., Freitag, N. P. and Mahinpey, N. (2005), A simple kinetic model for coke combustion during an in situ combustion (ISC) process. Presented at the 6th Canadian International Petroleum Conference, Calgary, Alberta, June 7-9.

Rosenbrock, H. H. (1963), 'Some general implicit processes for numerical solution of differential equations', *Computer Journal* **6**(4), 329–330.

Runge, C. (1895), 'über die numerische auflösung von differentialgleichungen', *Mathematische Annalen* **46**, 167–178.

Saad, Y. (1994), *SPARSKIT: A Basic Tool Kit for Sparse Matrix Computations*,

University of Minnesota, MN.

Sandu, A., Verwer, J. G., Bloom, J. G., Spee, E. J., Carmichael, G. R. and Potra, F. A. (1997), 'Benchmarking stiff ODE solvers for atmospheric chemistry problems: II. rosenbrock solvers', *Atmospheric Environment* **31**(20), 3459–3472.

Sandu, A., Verwer, J. G., Loon, M. V., Carmichael, G. R., Potra, F. A., Dabdub, D. and Seinfeld, J. H. (1997), 'Benchmarking stiff ODE solvers for atmospheric chemistry problems: I. implicit vs. explicit', *Atmospheric Environment* **31**(19), 3151–3166.

Sarathi, P. S. (1999), In-situ combustion handbook – principles and practices, Technical report, U.S. Department of Energy. DOE/PC/91008-0374.

Schult, D. A., Matkowsky, B. J., Volpert, V. A. and Fernandez-Pello, A. C. (1996), 'Forced forward smolder combustion', *Combustion and Flame* **104**, 1–26.

Stokka, S., Oesthus, A. and Frangeul, J. (2005), Evaluation of air injection as an ior method for the giant ekofisk chalk field, Society of Petroleum Engineers. SPE 97481: Presented at the SPE International Improved Oil Recovery Conference, Kuala Lumpur, Malaysia, December 5-6.

Stone, H. L. (1973), 'Estimation of three-phase relative permeability and residual oil data', *Journal of Canadian Petroleum Technology* **12**(4), 53–61.

Strang, G. (1968), 'On the construction and comparison of difference schemes', *SIAM Journal of Numerical Analysis* **5**(3), 506–517.

Thomsen, P. G. (2006), Discontinuities in ODEs - systems with change of state, Technical Report IMM-2006-07, Informatics and Mathematical Modelling, Technical University of Denmark.

Tingas, J., Greaves, M. and Young, T. J. (1996), Field scale simulation study of in-situ combustion in high pressure light oil reservoirs, Society of Petroleum Engineers. SPE 35395: Presented at the SPE/DOE Improved Oil Recovery Symposium, Tulsa, OK, April 21-24.

Twu, C. H. (1984), 'An internally consistent correlation for predicting the critical properties and molecular weights of petroleum and coal tar liquids', *Hydrocarbon Processing* **16**, 137–150.

Walter, A. L., Frind, E. O., Blowes, D. W., Ptacek, C. J. and Molson, J. W. (1991), 'Modeling of multicomponent reactive transport in groundwater. 1. model development and evaluation', *Water Resources Research* **30**(11), 3137–3148.

Westbrook, C. K., Mizobuchi, Y., Poinsot, T. J., Smith, P. J. and Warnatz, J. (2005), 'Computational combustion', *Proceedings of the Combustion Institute* **30**, 125–157.

Whitson, C. and Brule, M. (2000), *Phase Behavior*, Society of Petroleum Engineers. SPE Monograph, volume 20.

Whitson, C. H. and Michelsen, M. L. (1989), 'The negative flash', *Fluid Phase Equilibria* **53**, 51–71.

Williams, R., Burrage, K., Cameron, I. and Kerr, M. (2002), 'A four-stage

index 2 diagonal implicit runge-kutta method', *Applied Numerical Analysis* **40**, 415–432.

Xu, T., Sonnenthal, E., Spycher, N. and Pruess, K. (2004), *THOUGHREACT User's Guide: A Simulation Program for Non-Isothermal Multiphase Reactive Geochemical Transport in Variably Saturated Geologic Media*, Lawrence Berkeley National Laboratory, Berkeley, CA.

Yeh, G.-T. and Tripathi, V. S. (1991), 'A model for simulating transport of reactive multispecies components: model development and demonstration', *Water Resources Research* **27**(12), 3075–3093.

Younis, R. and Gerritsen, M. (2006), Multiscale process coupling by adaptive fractional stepping: An in-situ combustion model, Society of Petroleum Engineers. SPE 93458: Presented at the 2006 SPE/DOE Symposium on Improved Oil Recovery, Tulsa, OK, April 22-26.

Zlatev, Z. (1995), *Computer Treatment of Large Air Pollution Models*, Kluwer Academic Publishers.

Morten Rode Kristensen

Development of Models and Algorithms for the Study of Reactive Porous Media Processes

ISBN: 978-87-91435-74-9